

NUMERICAL INVESTIGATION OF THE FRACTURE PROPERTIES OF MANATEE RIB  
BONE USING EXPERIMENTALLY DETERMINED ANISOTROPIC ELASTIC  
CONSTANTS

By

JEFFREY MICHAEL LEISMER

A DISSERTATION PRESENTED TO THE GRADUATE SCHOOL  
OF THE UNIVERSITY OF FLORIDA IN PARTIAL FULFILLMENT  
OF THE REQUIREMENTS FOR THE DEGREE OF  
DOCTOR OF PHILOSOPHY

UNIVERSITY OF FLORIDA

2007

© 2007 Jeffrey Michael Leisner

To my sons, Finn and Jake, who make me laugh and always keep life exciting. To my amazingly beautiful wife, Renee, I am indebted to you for your patience and for doing such a wonderful job with our boys during this multifaceted portion of our lives. To my very supportive family and friends, who have believed in me every step of the way.

## ACKNOWLEDGEMENTS

I thank my supervisory committee for their mentoring and/or for providing me access to their labs, computers, equipment, supplies, and graduate students. I also thank Dr. Anusavice (Chair of the Dental Biomaterials Department) and Dr. Daegling (Associate Professor in the Department of Anthropology) for extending the same courtesy with their labs and students. I thank my (current and former) lab mates in the Computational Solid Mechanics lab (Erik Knudsen, George Levesque, Linus Norlander, Matt Williams, Mika Lautaoja, Nathan Branch, Niraj Bidkar, Sangeet Srivastava, Shadab Siddiqui, Srikant Ranjan, Yogen Utturkar, and Tae Joong (TJ) Yu) for their friendship and participation in many great discussions and outings as well as for assisting with various aspects of my research. I thank Kari Clifton and Jiahau (Bratt) Yan for inspiring me to work on this project and for helping to pave the path for my work. Maggie Stoll helped me set-up equipment for harvesting the rib bones used in my study and was very generous with her time. Mike Braddock helped out tremendously by allowing for me to use his machine shop to prepare my bone specimens and fixtures. Brian Robinson machined a fixture for use in my experiments. Allyson Barrett provided assistance locating persons and equipment to help with specimen preparation. Ben Lee assisted with shear specimen preparation. Bret Stanford demonstrated how to use the VIC equipment and answered many questions I had on the subject. Nancy Strickland spent many days writing custom Labview code for my experiments and showed me how to operate the universal testing machine used in my studies. Robert Smith spent many hours powder coating my fracture specimens in preparation for the SEM analysis. The Major Analytical Instrumentation Center (MAIC) at the University of Florida performed SEM analyses for my quantitative fractography study. I thank those who discussed my research with me in Dr. Ifju's, Dr. Mecholsky's, and Dr. Reep's labs. Drs. Kathy Howe and Laurie Gower

facilitated motivating discussions by founding/organizing the Bone Research Group, an interdisciplinary group of researchers performing research on bone and collagen at the University of Florida. Thanks to Dr. Walsh for being a great conversationalist and for co-presenting on the topic of “Bone (Bio) Mechanics” with me at a UF Bone Research Group meeting. Mark Tillman and John Chow provided much guidance while I was searching for a suitable dissertation topic. I could not have gotten where I am without the aid of my parents; I thank them for always being there and for providing me with life-shaping advice, knowledge, and skills. My nieces, Auriana and Kaiya, taught me much about nature, space, science, and technology, which helped me to gain a better perspective on my research. My brother, Matt, enriched my learning experience by adding positive energy to my life. My sister-in-laws, Charlene and Melissa, my brother-in-law, Andrew, my in-laws, my extended family, and friends were always there to recharge me during my trips to Michigan. My wife, Renee, provided much support during my career as a graduate student, helped motivate the move to Florida, shared many great times with me, and has been a wonderful mother to our two boys. Thank you, Finn and Jake, for keeping my spirit light and for showing me how fun it is to learn new things; you guys are so cool. Lastly, I would like to thank all of those who believed in my work and who contributed to my success at the University of Florida.

## TABLE OF CONTENTS

	<u>page</u>
ACKNOWLEDGEMENTS .....	4
LIST OF TABLES .....	9
LIST OF FIGURES .....	10
ABSTRACT .....	13
CHAPTER	
1 INTRODUCTION .....	15
Motivation and Introduction .....	15
Florida Manatee ( <i>Trichechus manatus latirostris</i> ) .....	16
Hierarchy of Bone .....	19
Level 1: Major Components .....	19
Level 2: The Mineralized Collagen Fibril Building Block .....	20
Level 3: Fibril Arrays .....	21
Level 4: Diversity in Fibril Array Organizational Patterns .....	21
Level 5: Cylindrical Motifs – Osteons .....	23
Level 6: Solid versus Spongy Bone .....	24
Level 7: Whole Bones .....	25
Manatee Bone Tissue .....	25
2 EXPERIMENTAL METHODS IN BONE MECHANICS .....	28
Specimen Preparation .....	28
Cutting and Machining of Bone .....	28
Preservation .....	29
Potting .....	29
Standardized Tests .....	29
Tensile Testing .....	30
Shear Testing .....	31
Ultrasonic Testing .....	32
Visual Image Correlation (Speckle Image Photogrammetry) .....	33
Deformation accuracy .....	34
Mirrored image correlation .....	35
Rotated specimen method .....	35
Fracture Tests .....	36
Single Edge V-Notched Beam (SEVNB) Tests .....	36
Chevron-Notched Beam Tests .....	37
Three Point Bend Tests .....	37

	Quantitative Fractography .....	37
3	BONE FRACTURE MECHANICS .....	43
	Fracture in Engineering Materials .....	43
	Fracture Testing of Bone .....	48
	Validity of using LEFM to Model Bone Fracture .....	48
	Rising R-curve Approach to LEFM .....	49
	Elastic-Plastic Fracture Mechanics (EPFM) .....	49
	Testing Procedures .....	50
	Anisotropic Fracture Analysis of Bone .....	50
4	OVERVIEW AND ORGANIZATION OF THE EXPERIMENTS .....	54
	Overview of the Experiments .....	54
	Pilot Tensile Tests .....	54
	Tensile Tests .....	55
	Shear Tests .....	56
	Off-Axis Tensile Tests .....	57
	Variable Strain Rate Tensile Tests .....	57
	Notched Tensile Tests .....	58
	Numerical Fracture Tests .....	59
5	TENSILE PROPERTIES OF CORTICAL BONE USING MIRRORED IMAGE CORRELATION (MIC) .....	61
	Short Summary .....	61
	Introduction .....	62
	Materials and Methods .....	65
	Results .....	69
	Discussion .....	71
	Conclusions .....	72
6	ANISOTROPIC ELASTIC TENSILE PROPERTIES .....	81
	Short Summary .....	81
	Introduction .....	82
	Methods .....	84
	Results .....	87
	Discussion .....	87
	Conclusions .....	90
7	ANISOTROPIC ELASTIC SHEAR PROPERTIES .....	94
	Short Summary .....	94
	Introduction .....	95
	Methods .....	97
	Results .....	100

Discussion.....	101
Conclusions.....	103
<b>8 MATERIAL SYMMETRY ANALYSIS .....</b>	<b>113</b>
Short Summary .....	113
Introduction.....	114
Material Symmetry .....	116
Hooke’s Law.....	117
Isotropic Materials.....	117
Transverse Isotropy .....	118
Orthotropy .....	119
Anisotropy .....	120
Transformations in Anisotropic Materials.....	121
Thermodynamic Restrictions on Elastic Constants.....	121
Tensile Testing.....	122
Material Symmetry Analysis .....	123
Results.....	124
Discussion.....	125
Example 8-1.....	130
Example 8-2.....	133
Example 8-3.....	135
<b>9 ANISOTROPIC FRACTURE PROPERTIES OF MANATEE RIB (CORTICAL) BONE: A NUMERICAL AND EXPERIMENTAL INVESTIGATION .....</b>	<b>137</b>
Short Summary .....	137
Introduction.....	138
Materials and Methods .....	139
Results.....	143
Discussion.....	144
Conclusions.....	147
<b>10 CONCLUDING REMARKS.....</b>	<b>154</b>
<b>APPENDIX</b>	
<b>A TENSILE TESTING AT VARIOUS CROSSHEAD SPEEDS .....</b>	<b>157</b>
<b>B MATERIAL PROPERTY CALCULATIONS.....</b>	<b>159</b>
<b>C VISUAL IMAGE CORRELATION (VIC) EQUIPMENT TUTORIAL.....</b>	<b>168</b>
<b>LIST OF REFERENCES.....</b>	<b>179</b>
<b>BIOGRAPHICAL SKETCH .....</b>	<b>186</b>

## LIST OF TABLES

<u>Table</u>	<u>page</u>
4-1 Tensile tests.....	60
4-2 Shear tests. ....	60
4-3 Numerical tests.....	60
5-1 Elastic moduli from MIC analysis. Mean values are presented $\pm$ standard deviations along with the number of specimens used to compute the mean values ( $n$ ).....	74
5-2 Poisson’s ratios from MIC analysis. Index 1 denotes the [100] direction, index 2 denotes the [010] direction, and index 3 denotes the [001] direction.....	74
5-3 Summary of known manatee rib material properties.....	74
6-1 Tensile properties of the Florida manatee rib bone. Mean values are presented as a function of specimen orientation .....	90
6-2 Summary of known manatee rib material properties.....	91
7-1 Shear modulus and coefficient of variation ( $CV$ ) from cyclic tests. Mean values are presented $\pm$ standard deviations.....	104
7-2 Shear modulus of three orthogonal orientations of manatee rib bone. Mean values are presented $\pm$ standard deviations along with the number of specimens used ( $n$ ).....	104
8-1 Mean tensile and shear properties of manatee rib bone obtained from parts I and II of this paper, respectively.....	127
8-2 Average load, number of specimens tested, average strains calculated by VIC (experimental).....	127
9-1 Orientation dependent fracture toughness and fracture parameters of manatee rib (cortical) bone .....	148
9-2 Selected studies measuring fracture toughness of compact bone (modified from Yan (2005)).....	149
A-1 Viscoelastic properties of manatee rib bone. Three cross-head speeds were tested for their effect on elastic modulus for .....	157

## LIST OF FIGURES

<u>Figure</u>	<u>page</u>
1-1 Florida manatees. ....	26
1-2 Hierarchical levels of bone architecture. ....	27
1-3 Three-dimensional, sliced view of an osteon.....	27
1-4 Cortical and trabecular bone within a section of long bone.....	27
2-1 ASTM tensile specimen recommendations. ....	38
2-2 Tensile specimen with some bending present.....	39
2-3 Iosipescu shear specimen. This specimen is loaded uniaxially in order to generate nearly pure shear in the gage section. ....	39
2-4 Iosipescu shear specimens fitted in grips on a uniaxial testing machine .....	40
2-5 Ultrasonic test specimen geometries (A) cube used to obtain 18 velocities; B) shape used to obtain 9 velocities). ....	40
2-7 A) Close-up of the notch in an SEVNB specimen. B) Close-up of the v-notch in an SEVNB specimen .....	42
2-8 Chevron-notched (CN) specimen. ....	42
2-9 Three-point bend specimen and loading constraints.....	42
3-1 Compact tension (CT) specimen dimensions. ....	52
3-2 Single edge notched bend (SENB) specimen dimensions.....	52
3-3 Definition of the coordinate system associated with a crack tip.....	53
3-4 Three modes of failure .....	53
5-1 Three-dimensional surface as seen by two imaging sensors (courtesy of Correlated Solutions, Inc, West Columbia, SC). ....	75
5-2 Movement of a sample square subset used for cross-correlation function estimation .....	75
5-3 Manatee skeleton .....	76
5-4 Stereographic set-up used in the MIC analysis.....	76

5-5	Example image and target region used by VIC3D to generate a dataset and the associated surface plot created by VIC3D .....	77
5-6	Typical $dV/dY$ curve showing all data points on the gage section of a manatee rib bone specimen.....	77
5-7	Nomenclature used for the Poisson's ratio analysis. Shaded faces represent the faces on which each respective Poisson's ratio was evaluated.....	78
5-8	Stress-strain curve for a [010] specimen.....	78
5-9	Schematic of Proximodistal [100] specimens prepared from the middle 1/3 <sup>rd</sup> of an adult manatee rib bone.....	79
5-10	Proximodistal [100] stress-strain curve for three dry manatee rib bone specimens (A, B, and C) loaded to failure.....	79
5-11	Superficial-Deep [010] stress-strain curve for three dry manatee rib bone specimens (A, B, and C) loaded to failure.....	80
5-12	Craniocaudal [001] stress-strain curve for three dry manatee rib bone specimens (A, B, and C) loaded to failure.....	80
6-1	Articulated manatee skeleton.....	91
6-2	Visual image correlation performed on the gage section of a manatee rib bone tensile specimen .....	92
6-3	Plot of the deformation versus position data ( $dv$ vs. $dy$ ) in the gage region of a tensile specimen .....	92
6-4	Stress-strain plot for a given load step during a VIC analysis.....	93
7-1	Three-dimensional surface as seen by two imaging sensors .....	104
7-2	Movement of a sample square subset used for cross-correlation function estimation in the VIC analysis.....	105
7-3	Manatee skeleton .....	105
7-4	The middle third of each rib was used for the analysis to reduce potential site-specific variability between specimens.....	106
7-5	Orientation and sectioning of the shear specimens used in this study.....	107
7-6	Iosipescu specimen dimensions. The length of the $G_{23}$ specimens was limited by the physical dimensions of the manatee rib cross section. ....	107
7-7	Iosipescu specimen prepared for simultaneous shear gage and VIC testing .....	108

7-8	Image showing the test section and loading of an Iosipescu specimen prepared for simultaneous VIC and shear gage testing .....	108
7-9	Plots showing the high correlation of the $dU/dY$ and $dV/dX$ data points across the entire test section of an Iosipescu VIC specimen .....	109
8-1	Specimen orientations used in the present analysis. ....	128
8-2	Typical vertical position versus vertical deformation ( $dV/dY$ ) curve .....	128
8-3	Surface plots showing the variation in material properties with material axes .....	130
8-5	Rotation of the material coordinates to specimen coordinates for a specimen lying in the [110] material direction.....	133
9-1	Manatee skeleton. Center ribs from adult manatees were used in this study .....	150
9-2	Mode I (opening mode) stress intensity factor (SIF) nomenclature. ....	151
9-3	Notch tip geometry showing an illustration of the finite elements and variables used in the fracture toughness models.....	151
9-4	Numerically-determined mode I SIF versus normalized crack front.....	152
9-5	Scanning electron micrographs of typical fracture surfaces from specimens loaded in each of the three principal orthogonal directions.....	152
9-6	Schematic (left) demonstrating the “peeling” of fibrous layers during the fracture experiments. ....	153
9-7	R-curve behavior of manatee rib bone demonstrating a trend of increasing fracture toughness with increasing critical crack length. ....	153
A-1	Viscoelastic properties of manatee rib bone. Results are shown for one proximodistal specimen loaded at three different strain rates.....	158

Abstract of Dissertation Presented to the Graduate School  
of the University of Florida in Partial Fulfillment of the  
Requirements for the Degree of Doctor of Philosophy

NUMERICAL INVESTIGATION OF THE FRACTURE PROPERTIES OF MANATEE RIB  
BONE USING EXPERIMENTALLY DETERMINED ANISOTROPIC ELASTIC  
CONSTANTS

By

Jeffrey Michael Leismer

August 2007

Chair: Nagaraj Arakere  
Cochair: John Mecholsky, Jr.  
Major: Mechanical Engineering

Manatees are docile marine mammals that are inhabitants of the Florida coastline as well as some of the natural springs. They are listed as an endangered species by the U.S. Department of the Interior. The coexistence of humans and manatees in Florida waterways has contributed to the depletion of the manatee population: collisions between watercrafts and manatees are responsible for 25% of all manatee deaths. Previous research at the University of Florida aimed to reduce watercraft-related deaths by relating the work-to-fracture of whole manatee ribs to the kinetic energy of a small boat traveling at various speeds. The intention was to provide scientific evidence for the reduction of speed limits in manatee populated waterways. Data collected by the researchers was limited by the scope of their research, and there still remains significant work to be done to understand the response of manatee rib bones to mechanical loading.

The purpose of the present study was to fully characterize the elastic anisotropy of the Florida manatee rib bone in terms of mechanical and fracture properties. Previous research conducted on anisotropic materials shows that neglecting anisotropy (directional dependence of material properties) by modeling a material as isotropic (non-directionally dependent) reduces the accuracy of the analysis. Therefore, it was necessary to first establish an appropriate material

model for manatee rib bone (specific aim 1) that could be used to accurately predict the response of the material to failure loading. Stereographic imaging techniques utilizing visual (digital) image correlation were developed to measure the elastic anisotropic constitutive constants of manatee rib bone (specific aim 2). These techniques were verified by comparison with traditional mechanical testing techniques. Once fully characterized, experimental fracture tests were performed on the material (specific aim 3). Numerical models of the fracture specimens were then developed that incorporated experimentally determined anisotropic elastic constants, failure loads, and critical crack lengths (specific aim 4) to elucidate the fracture properties of manatee rib bone.

It was found that manatee rib bone was more anisotropic and less tough than similar classifications of bone from other animals. Further contributing to the uniqueness of this material, the tissue was previously shown to have a greater mineral density than bone from most other animals, manatee ribs are mostly cortical bone, and the ribs do not possess a marrow cavity. Thus manatee ribs are brittle, solid structures that exhibit a high degree of anisotropy and they have potential to fracture with relative ease.

From an engineering perspective, my study introduces modeling and analysis tools never before used to study bone fracture. From a conservation standpoint, the information gathered from this study (with proper interpretation) can be used to help protect the already depleted manatee population by providing additional scientific evidence for restricting speed limits of watercraft in manatee populated waterways.

## CHAPTER 1 INTRODUCTION

### **Motivation and Introduction**

The issue of a 3D anisotropic stress intensity factor ( $K$ ) solution was previously addressed by other students in Dr. Nagaraj Arakere's research group for various materials (single crystal nickel base superalloys (Ranjan, 2005) and foam insulation for the space shuttle external fuel tank (Knudsen, 2006a)), but this is the first time the 3D anisotropic  $K$  solution has been studied for a material as complex as bone. Bone is a composite material with a hierarchical structure that exhibits a wide range of properties at each length scale (Weiner and Wagner, 1998; Rho et al., 1998). Very little is understood about how bone fails or the means by which hierarchical structures affect failure (Akkus, 2004). My analysis generates more information regarding the material and fracture properties of bone than what is currently available in the literature and therefore provides a significant contribution to the field of bone mechanics.

Though a significant body of literature exists on the material properties of human and animal bone, reports of all 9 orthotropic or 5 transversely isotropic elastic constants (depending on how the bone is classified) come few and far between. My study explores the variation in elastic constants as a function of material orientation so that the elastic anisotropy of manatee rib bone can be fully characterized.

The methods by which specimens are harvested, prepared, preserved, and tested greatly affect the results of mechanical tests (An and Draughn, 2000), while the influences of microstructure on fracture properties found from mechanical testing of bone have only recently been investigated (Malik et al., 2003; Nalla et al., 2003, 2005 a; Vashishth, 2004). Yan et al. (2006b) presented discussion on the differences in fracture toughness values found from different

species and attributed the differences to the microstructure of the bones. The microstructure of manatee rib bone is discussed along with the preparation, preservation, and testing procedures used in my study. The intent is to provide sufficient information for a full and accurate comparison of the results found here to other work reported in the literature.

This is a first study of its kind, in that no other researchers have employed the methods used here for the formulation of a 3D anisotropic stress intensity factor solution for bone. In fact, current techniques used to compute the fracture properties of bone almost always neglect the anisotropy of the material. Therefore, one purpose of this investigation was to determine whether or not the anisotropic assumption plays a significant role in the fracture properties of this material. Arakere et al. (2005) found that the anisotropic assumption plays a significant role in the stress state about a notch in single-crystal materials. It is therefore hypothesized that fracture properties will likely be affected by the anisotropic assumption as well.

An experimental component to this work is provided as a preface to the computational analysis. Experiments are used to determine the elastic constants of compact bone from the ribs of adult Florida manatees. The elastic constants are then used as input to finite element (FE) models of fracture specimens. The computational analysis provides a predictive framework for the determination of the fracture properties of compact bone based on input of the correct material properties to the numerical model. Thus the methods reported in this document have the potential to mitigate the need for experimental analyses to determine fracture properties and stress states in bone specimens and whole bone.

### **Florida Manatee (*Trichechus manatus latirostris*)**

The Florida manatee (*Trichechus manatus latirostris*) (Figure 1-1) is listed by the U.S. Department of the Interior as an endangered species. This is due in large part to human presence in the manatee's habitat. Each year, 25-30% of all manatee deaths are a direct result of collision

with watercraft. Of these collisions, 66% of the deaths are attributed to impact, while the remaining deaths are attributed to wounds caused by propellers (Clifton, 2005). A clear understanding of the mechanical and fracture properties of the manatee rib bone is necessary to determine proper ways of protecting this endangered species from impact-related injuries.

Researchers at the University of Florida (Clifton, Golden, Koob, Mecholsky, Reep, and Yan) have been performing experiments with bone from the Florida manatee since 1999. Their work has resulted in the publication of several peer-reviewed articles (Clifton et al., 2003; Yan et al., 2006a, b, 2007). Material and fracture property data collected by these researchers was limited by the scope of their research, so a full picture of the material and fracture properties of manatee bone had yet to be developed.

A significant percentage of manatees die as a result of collisions with watercraft. Therefore, one of the objectives of Dr. Kari Clifton's work was to propose a scientific basis for enforcing watercraft speed limits in manatee-populated waters. She was able to relate the energy of impact from a collision between a manatee and a small boat traveling at various speeds to the energy required to fracture a manatee rib. One of Dr. Clifton's co-workers, Dr. Jia-Hau Yan, developed a finite element model of manatee bone that could be used to predict stresses at critical locations for a variety of impact loading conditions (Yan, 2002).

The techniques used in my study for modeling manatee bone further elaborate on the work conducted by Yan (2002). The models include increased material property data compared to Yan's 2002 model by assuming that the material exhibits some degree of anisotropy, rather than being isotropic. In the fracture study, notched tensile specimens are loaded to failure and the failure load and critical flaw sizes in the failed specimens are documented. The critical flaw is modeled in a finite element model, and failure loads from the experimental fracture study are

used as input to these models. Input of experimentally determined material properties, failure load, and critical flaw sizes allow for the first time ever the determination of the fracture toughness of manatee rib bone from a numerical model. The predictive capacity of the model is analyzed by comparison of the numerical results with experimental results found here and by Clifton (2005) and Yan (2002, 2005).

This is the first study to analyze the anisotropic fracture properties of manatee rib bone. To date, manatee rib bone fracture properties have only been tested for cracks propagated in the transverse direction of the rib (Clifton, 2005; Yan, 2005). The transverse orientation represents the “most likely” orientation for cracks resulting from a side impact from a watercraft. However, impact can occur at any angle, and it is still not known if other crack orientations are as detrimental as the orientation already tested. The literature supports the idea that cracks propagated in the longitudinal direction of the bone result in a lower value of fracture toughness. Fracture toughness for cracks propagated in the transverse direction of long bones is ~50-100% greater than for longitudinally propagated cracks in cortical bone (Nalla et al., 2005b)). Thus the work by Yan et al. (2006 a, b, 2007a) may underestimate the severity of collisions between manatee and watercraft. The 3D anisotropic stress intensity factor formulations implemented by the finite element software is used to determine which of the tested orientations is the least fracture resistant.

In addition to further supporting the idea of enforcing speed limits in manatee zones (Clifton, 2005), the current study lends itself towards the development of more realistic computational models of bone with improved predictive capabilities over current models. In a broader scope, it is anticipated that the methods developed for this study can be extrapolated to analyses of fracture in the skeletal systems of other animal species including humans. The

present work aims at providing a universally accepted model of bone that uses known material properties to predict the fracture toughness of any cortical bone specimen for any material orientation.

This study aims to build on the work of other University of Florida researchers in several ways including: 1) fully characterizing manatee bone material properties, 2) evaluating the feasibility of using image-based techniques to measure the material properties of manatee bone, 3) examining the microstructure and critical crack lengths of failed tensile specimens, and 4) numerically predicting the fracture properties of manatee bone.

### **Hierarchy of Bone**

Bone is a highly complex material, characterized by its structural hierarchy. At the very basic level, bone is predominantly comprised of collagen fibrils, hydroxyapatite crystals, and water. The apatite represents the inorganic component of bone, while the collagen is the dominant organic component. The structural arrangement of these materials varies depending on the length scale being observed (Figure 1-2), hence the hierarchy of bone architecture. The following sections will outline the seven hierarchical levels of bone identified by Weiner and Wagner (1998).

#### **Level 1: Major Components**

Hydroxyapatite crystals are plate-shaped and are on the order of 50 x 25 x 2.5 nm (length by width by thickness). The crystals exhibit hexagonal symmetry, and thus exhibit transversely isotropic material properties. No studies have yet looked at the mechanical properties of these crystals when extracted from bone. However, the elastic modulus of large single crystals of hydroxyapatite is in the vicinity of 114 GPa. Mineral content of bone and elastic modulus are positively correlated to one another, although the energy to fracture decreases with increasing

mineral content (Currey, 1990). The dry weight percentage of hydroxyapatite in bone is typically 66%, while the crystal accounts for roughly  $\frac{1}{2}$  of the volume (An and Draughn, 2000).

Type I collagen fibrils comprise the largest portion of organic components in bone, although there exist over 200 other types of proteins within bone. Each fibril is between 80 and 100 nm in diameter. The collagen fibrils are comprised of three polypeptide chains that are wound into a triple helix. The helix is cylindrical in shape with a diameter of 1.5 nm and length of 300 nm. The fibril structure is orthotropic. Mechanical properties of individual fibers are difficult to obtain, since the fibrils exist in groups (called fibers) in biological materials. The properties of fibers vary depending on the organization of fibrils within the fiber, which is different from one tissue to the next. Collagen accounts for  $\sim\frac{1}{2}$  of the volume of dry bone, weighing in at  $\sim\frac{1}{3}$ <sup>rd</sup> the dry weight of the tissue (An and Draughn, 2000).

Water exists within and between fibrils as well as between fibers. Studies have shown dramatic differences in the properties of hydrated versus dehydrated bone (Currey, 1990; Yan, 2005). Generally, the percentage of water in bone for various species is inversely proportional to the mineral content, while the collagen content is fairly constant for most species. Evans (1973) references reports of water content ranging from a low of 9.49% in the tibia of cattle to a high of 73 volume % in the tibia of young dogs. Neuman and Neuman (1957) found that newly forming bone has a water content of 60%, while senile bone has a water content of only 10%.

## **Level 2: The Mineralized Collagen Fibril Building Block**

At the mineralized collagen fibril building block length scale, the structure is a platelet-reinforced fibril. Here, hydroxyapatite crystals are arranged in layers inside of collagen fibrils. The layers align with the long axis of the elliptical cross-section of the crystals. The arrangement of crystals within the fibrils makes the fibrils orthotropic. As the crystals grow, they compress the triple-helical polypeptide chains, which provide an organic matrix in which the crystals are

embedded. Hydroxyapatite also exists outside of the fibrils. The mineral crystals that exist outside the fibrils exhibit little order in their structural arrangement.

### **Level 3: Fibril Arrays**

Mineralized collagen fibrils usually exist in bundles. The nature of how individual fibrils are arranged relative to one another in a bundle is poorly understood. One method of determining the structural arrangements of these bundles would be to assess their material properties. Orthotropic properties would coincide with an ordered arrangement of fibrils within the bundle, while transversely isotropic properties would imply a random alignment of fibrils within the bundles.

Fibril bundles can be measured at the millimeter length scale, although level 3 generally pertains to bone structures at or below the micron length scale. Tendons are examples of fibril bundles. Mineralized tendons have modulus values ranging from 162 to 825 MPa, while demineralized tendons have a much lower modulus (67 to 103 MPa). Tendons generally are less than 50 wt% mineral.

Parallel-fibered bone is another structure comprised of mineralized collagen fibrils. Their mineral weight percent is on the order of 65. Hardness tests indicate that this bone is orthotropic in nature. Parallel-fibered bone has an elastic modulus of ~26 GPa along its long axis, while the transverse orientations have a modulus of only ~11 GPa.

### **Level 4: Diversity in Fibril Array Organizational Patterns**

Several patterns exist for fibril arrays at level 4 of bone structural hierarchy. Pattern 1 is categorized as an array of parallel fibrils. These parallel fibers exist in tendons, and they are especially prevalent in mineralized form at tendon attachment points to bone. Parallel-fibered bone grows rapidly, leaving spaces between each layer of newly formed bone, where lamellar

bone will be subsequently laid. The combination of parallel-fibered and lamellar bone is called fibrolamellar (plexiform) bone.

Poorly arranged, loosely packed fibril bundles comprise the woven fiber structure of pattern 2. Both the matrix and the mineral are disorganized in woven bone. The disorganization of woven bone yields anisotropic material properties rather than isotropic properties. Woven bone is rapid in growth, and is suitably found at fracture sites where rapid bone growth is necessary.

Fibril bundles and fiber bundles can exist in plywood-like layers, hence the name for pattern 3: plywood-like structures. The simplest structure has alternating orthogonal parallel fibril arrays. However, the thickness of each layer is not always uniform, although layers usually repeat in a pattern of thick then thin, creating a basic repeating unit. A more complex plywood-like structure has five layers of parallel fibrils oriented at ~30 degrees from one another. This structural unit is not symmetrical since there are five, rather than six, layers. Within each layer exists an internal crystalline structure. Most of the layers have a crystal layer that is parallel to the boundary of the fibril array, while a couple of the layers have a rotated axis relative the boundary. The rotations of these layers is in one direction, thus the lamellar unit is asymmetrical. Lamellar bone also exists in the form of cylinders, called osteons. Lamellar bone is less anisotropic than plexiform bone (anisotropic ratio of 1.13-1.21 for lamellar bone versus 1.18-1.47 for plexiform bone).

Pattern 4 represents radial fibril arrays. These arrays are generally formed in dentin, the material at the inner layer of the teeth. Here, the fibrils lie in the plane parallel to the pulp cavity surface where dentin formation takes place. There is a poor organization of fibrils within this plane. Dentin is highly anisotropic in structure due to the organization of collagen fibrils,

although material properties reveal that dentin is nearly isotropic. This reveals that the material properties are more dependent on the poor organization of crystals than on the structural organization of the collagen fibrils.

### **Level 5: Cylindrical Motifs – Osteons**

The long cylindrical lamellar bone structures that are preferentially aligned along the axes of bones are called osteons (Figure 1-3). At the center of osteons are hollow tunnels that function as blood vessels. Capillary-like tunnels called canaliculi stem from the hollow center of the osteons. The canaliculi house bone cells called osteocytes. Osteocytes can remain as osteocytes for the duration of their life, or they can turn into osteoclasts or osteoblasts to meet the remodeling needs of the surrounding tissue. During the process of remodeling, bone eating cells called osteoclasts eat old or damaged bone, creating a tunnel for the bone forming cells (osteoblasts) to lay new bone. The new bone is laid in layers, creating the lamellar structure of osteons. As the newly formed osteonal bone ages, its mineral content increases. Osteons involved in the process of remodeling are called secondary osteons to differentiate them from the similarly-shaped structures found in the spaces between the parallel-fibered bone in primary plexiform bone.

Discussion on the stasis of bone becomes important at this level. Homeostasis occurs when the rate of bone formation equals that of bone absorption. If the rate of absorption exceeds that of formation, bone becomes structurally deteriorated. Osteoporosis, a disease characterized by low bone mass and structural deterioration of bone tissue, is the result of inadequate bone formation in response to bone absorption. Various drugs are available to prevent or slow the rate of bone absorption, resulting in a net gain of bone tissue. However, there is still some debate over whether bone's structural integrity is compromised when newly formed tissue is laid in voids without the repair of old, damaged tissue.

Mechanical influences on the skeleton are also observed at this level of bone hierarchy. Mechanical loading governs where bone remodels, while hormones determine when it remodels. Osteons tend to align themselves with the principal stress direction, which has implications pertaining to the strength and damage resistance of osteonal bone. Transversely oriented cracks in bone tend to kink at the cement line interface between an osteon and surrounding bone tissue, while longitudinal cracks are able to propagate more freely. The cement line interface also acts as a barrier to crack propagation by blunting the tip of an approaching crack. The reduced mineral content of newly laid osteonal bone relative the surrounding mineralized matrix makes it difficult for cracks to initiate on the osteon. Thus, osteonal bone is both resistant to fracture and fatigue damage.

#### **Level 6: Solid versus Spongy Bone**

Cortical bone comprises the outer surface of bones, while trabecular bone tends to be found internal the cortical outer layer of whole bones (Figure 1-4). Trabecular bone, also known as spongy or cancellous bone, is named for its porous appearance. Trabecular bone porosity is generally in the 75 to 95% range (Yan, 2005). Trabeculae are rod or plate shaped structures that form the structure of cancellous bone. The strength of trabecular bone is attributed to both the mineral content (~60%) and the architecture of the tissue (~40%) (Kleerekoper, 2006). Solid bone is referred to as compact, or cortical, bone. Cortical bone exhibits very few pores. From its appearance one would not anticipate a great deal of anisotropy in cortical bone. However, the orientation of cortical bone constituents results in macroscopic anisotropy of its material properties. The elastic modulus of trabecular bone is on the order of 1 GPa, while that of cortical bone is ~20 GPa in the longitudinal direction (Cowin, 2002).

## **Level 7: Whole Bones**

At the largest length scale, whole bone is characterized in terms of its shape and function. Long bones, such as the femur and humerus, are used primarily for mobility and for support. Their internal structure is geared for a high strength-to-weight ratio. Flat bones are used primarily for protection of organs. The skull is an example of a flat bone. Irregular bones such as the scapula (shoulder bone), vertebra, and rib can be used for support and/or protection (e.g., the vertebrae protect the spinal cord from injury while at the same time providing support for our upper body).

### **Manatee Bone Tissue**

Manatee rib bones are mostly primary plexiform bone (Clifton, 2005), which is the predominant type of bone found in large land mammals. The Florida manatee is unique in the marine mammal kingdom in that it exhibits pachyostosis, characterized by thickening of bone tissue, replacement of cancellous bone with compact bone, and lack of a marrow cavity, while other marine mammals tend towards lower bone mass and density (Yan et al., 2006a). In addition to a more solid, dense bone structure, the mineral content of manatee rib bone is quite high (69% +/- 2%) (Clifton, 2005) compared to other mammals. The high density may help the manatee overcome buoyancy (Ray and Chinsamy, 2004) and it is responsible for the material response to loading being highly linear up to failure. The highly linear response to loading provides a reasonable argument for the use of linear elastic fracture mechanics (LEFM) to model fracture in manatee rib bone. The large size of manatee bone make it ideal for testing the fracture behavior of the material, since specimen sizes can be large enough to satisfy standard fracture testing protocols that require plane strain conditions to be met (e.g., ASTM E399). Also, the large size and the lack of a marrow cavity allow for the preparation of large specimens oriented about all material axes required to capture orthotropic material response to loading. The large size of the

bone also allows for more specimens to be cut from a single bone, thus reducing the natural variability between animals and between anatomical sites when aiming for statistically significant values of bone properties.

De Buffrenil and Schoevaert (1989) found that the dugong, a close relative of the manatee in the marine mammal world, has a higher bone mineral density and mineral content at the anterior (cranial) ribs than at the caudal ribs. It is expected that this trait is also present in the Florida manatee. The variation in mineral density by location means that specific subsets of ribs must be selected in order to reduce variability in mechanical test results. This will be discussed in more detail in later chapters.

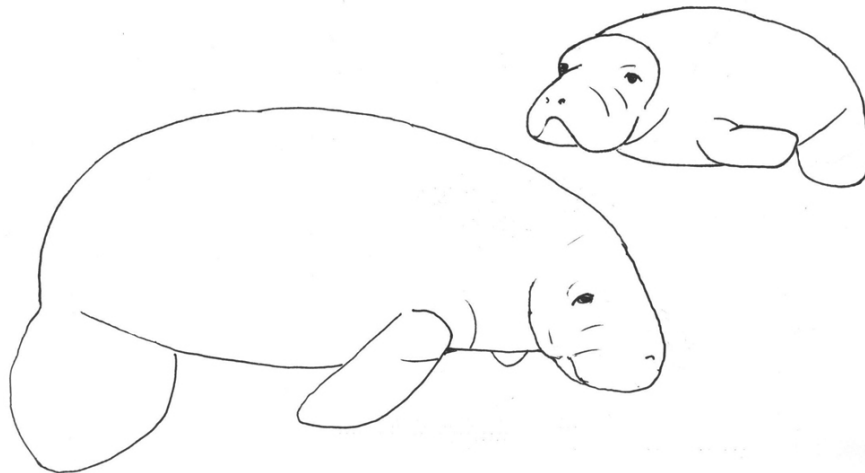


Figure 1-1. Florida manatees.

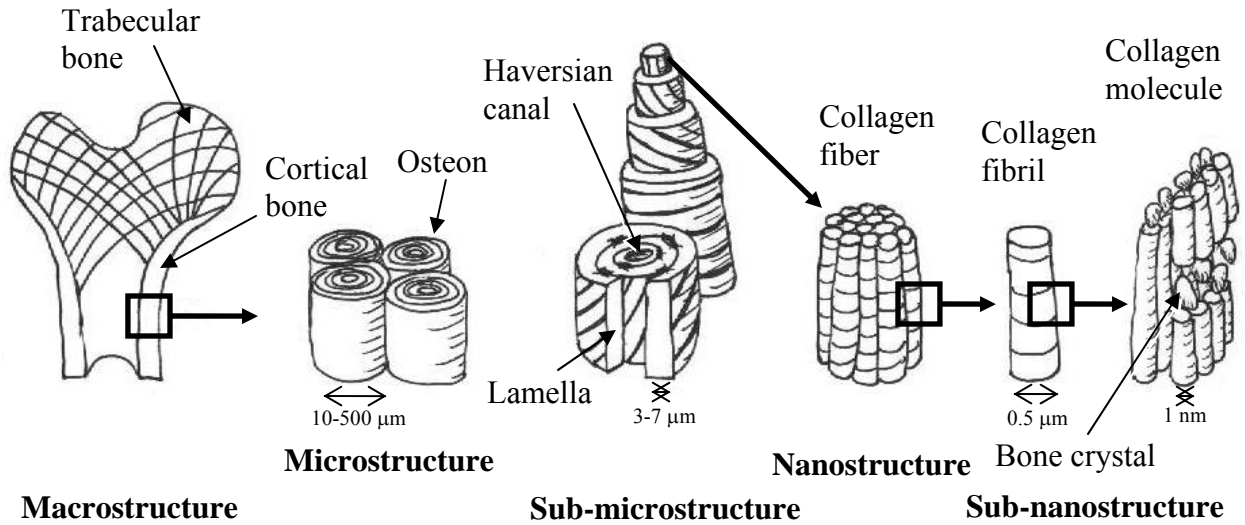


Figure 1-2. Hierarchical levels of bone architecture.

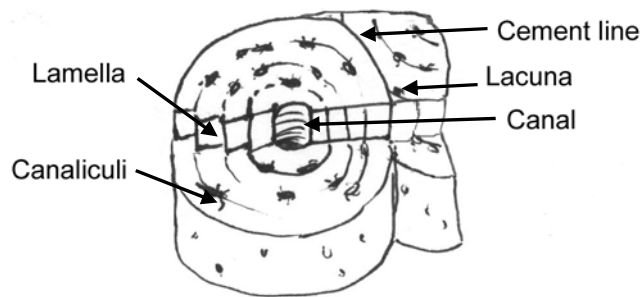


Figure 1-3. Three-dimensional, sliced view of an osteon.

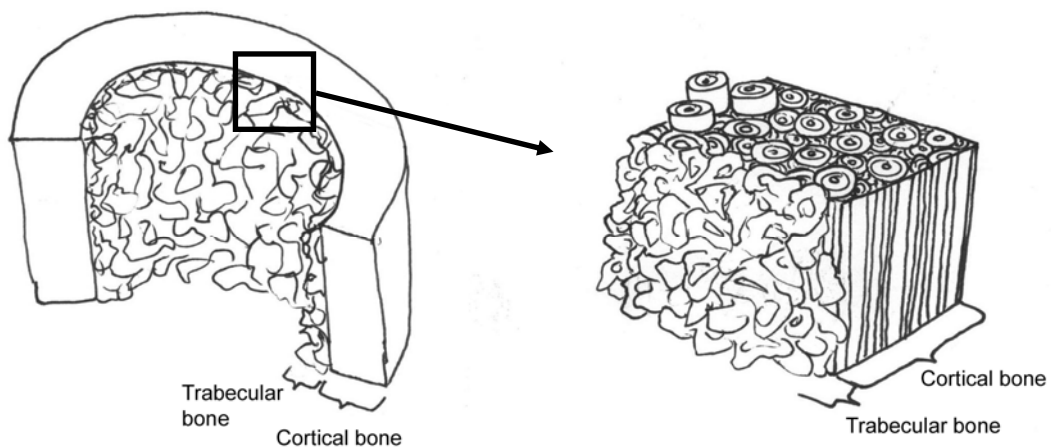


Figure 1-4. Cortical and trabecular bone within a section of long bone.

## CHAPTER 2 EXPERIMENTAL METHODS IN BONE MECHANICS

### **Specimen Preparation**

An and Draughn (2000) provide a detailed description of specimen preparation techniques and considerations. Their work can be referenced for additional details not reported here. The discussion in this chapter is limited to specimen preparation procedures relevant to the current study. The techniques provided below refer to macroscopic bone specimens in level 6 of the hierarchy of bone discussed in Chapter 1.

#### **Cutting and Machining of Bone**

Once bone is excised from an animal, it can be further cut into manageable sections. Rough cuts can be made using a band saw, hacksaw, or jigsaw. Efforts should be made to hydrate and cool the specimen while making any cut, since each of these factors can greatly affect material properties of the specimen. Water or saline can be used to cool and hydrate the bone. If the tools used to cut or machine the specimen are not resistant to water damage or corrosion from saline, then 1 to 2 mm of bone tissue should be removed from the cutting/working surface using wet sand paper (An and Draughn, 2000). Diamond-impregnated wire saws or low speed diamond-impregnated wafering saws reduce specimen damage compared to other types of cutting tools, and they can be used for finer cuts that do not need to be sanded or polished. A diamond coring tool can be used for cylindrical specimens. Vertical milling machines and lathes can be used to mill and turn or face specimens, respectively. The specimen should be irrigated with water or saline when using a mill or a lathe.

## **Preservation**

Drying, heating, freezing, embalming, or storing bone in saline or alcohol solutions can alter the material properties of bone. It is best to use freshly harvested bone when possible. If it is not possible to harvest fresh bone, it is recommended that the bone be wrapped in plastic wrap and stored in airtight bags in a freezer at -20° Celsius (An and Draughn, 2000). Properties will be best maintained with the muscles and soft tissues attached, although hydrating with saline solution after wrapping the bone in gauze is a reasonable alternative if storing the bone for shorter periods of time.

## **Potting**

Bone specimens can be potted in polymethylmethacrylate (PMMA) or epoxy to provide a better gripping surface for the specimen grips. The gripping surface should first be made free of fat and bone marrow using a water jet and soaking in trichloroethylene or a solution containing 10% bleach and 90% water. The surface should be allowed to dry before potting. Cyanoacrylate cement should be applied in several layers to improve the bond between the bone and the PMMA when specimens are subjected to large loads. Alternatives are available that make use of specimen geometry to remove the need for potting materials (e.g., tapered ends, milled grooves/slots, etc.).

## **Standardized Tests**

Mechanical test results can be greatly influenced by the specimen preparation techniques and testing methods. Therefore, standardized protocols should be closely adhered to in order to improve the accuracy of results. Some limitations exist for bone specimens prepared according to standardized tests for engineering materials, since size, gripping methods, and relatively low failure load levels often prevent standardized procedures from being adhered to (An and Draughn, 2000). The American Society for Testing and Materials (ASTM) has prescribed

standardized tensile testing procedures (ASTM C565, D1623, D3039, D3044, E8, and E132), a shear testing procedure (ASTM D143), and fracture testing procedures (ASTM E399, E561, E1820, and C1421, etc.), amongst other tests. These procedures are always being updated and new standards are being put in place in order to meet the demands of materials testing research. For example, although ASTM E399 is the standard for fracture testing of engineering materials, recent evidence suggests that ASTM E399 may not be appropriate to fully characterize the fracture properties of some materials with natural toughening mechanisms (Wallin, 2005).

### **Tensile Testing**

Tensile tests are used to find the elastic modulus and Poisson's ratio of a material. Dog-bone shaped specimens are recommended by ASTM for tensile tests. These testing procedures mandate the following dimensional relations: 1)  $d/D$  (gage width to grip width) ratio of 0.5, 2) gage length  $A \sim 3d$ , 4) grip length  $M = L/4$ , and 5) large fillet radius,  $R$  (Figure 2-1) (An and Draughn, 2000).

A reduced gage section is introduced to guarantee that the largest values of strain occur at the central portion of the specimen. Strain gages or extensometers are attached to the gage section to measure strain and deformation in the region, respectively. Strain gages are attached to a specimen using an adhesive and must be oriented appropriately to capture the desired strain reading. There are several types of strain gages, which can be classified by their foil pattern and other parameters. The most common foil pattern is found on the uniaxial strain gage, which provides an average value of strain in one direction over the foil region on a strain gage. The foil is oriented appropriately to capture strain in a particular direction. The elastic modulus of a specimen can be found when a foil gage is oriented along the loading axis and the load acting on the specimen is measured (e.g., with a load cell). When a uniaxial force is applied, the load can

be divided by the specimen cross-sectional area at the gage section and divided by the strain in the loading direction to obtain the elastic modulus (Equation 2-1).

$$\sigma = \frac{F}{A}, \quad E = \frac{\sigma}{\varepsilon} \quad (\text{Eq. 2-1})$$

where  $\sigma$  is the stress,  $F$  is the applied load,  $A$  is the cross-sectional area of the specimen gage section, and  $\varepsilon$  is the strain measured by the strain gage. A biaxial strain gage can be used to determine the Poisson's ratio of a material. Biaxial gages measure strain in two (perpendicular) directions, thus the ratio of the strains can be found (Equation 2-2).

$$\nu_{12} = -\frac{\varepsilon_2}{\varepsilon_1} \quad (\text{Eq. 2-2})$$

It is good practice to place a strain gage on both the front and the back of a specimen to account for any bending that may be present in the specimen during testing. The test fixture can often induce bending if precautions are not made to insure proper specimen alignment with the loading axis of the testing machine. Figure 2-2 shows a tensile specimen with some bending present due to specimen misalignment. Averaging the strains from gages mounted to two opposite faces of a bend specimen will remove the contribution of bending stresses to the average strain. Thus, the average measured strain is that due only to tensile loads and not to bending loads.

### **Shear Testing**

Shear specimens are generally rectangular in shape and contain a slot or groove on either side of the gage section (Figure 2-3). Nearly-pure shear can be obtained in anisotropic materials when loading Iosipescu specimens on a uniaxial machine. Graphical depictions of two Iosipescu test fixtures are provided in Figure 2-4. These fixtures remove the translational and twisting

motion of the upper and lower mounts caused by 3D stresses generated in anisotropic materials during testing, and thus Iosipescu shear testing fixtures like these are more useful for generating pure shear than when using other shear test specimens and fixtures. As with tensile tests, strain gages are used to measure the strain in a shear specimen. Specialized gages called shear gages were developed by Ifju (1992) to measure shear across the gage section of a shear specimen. The distribution of shear stress is non-uniform across the gage section. Therefore, the shear strain is obtained by integrating over the gage region.

Shear modulus can also be obtained using cylindrical (torsion) specimens although shear specimens will be used in this analysis. Equation 2-3 can be used to find the shear modulus when using a torsion test.

$$\theta = \frac{TL}{JG} \text{ (radians)}, G = \frac{TL}{J\theta} \text{ (N/m}^2\text{)} \quad \text{(Eq. 2-3)}$$

where  $\theta$  is the angle of twist,  $T$  is the applied torque,  $L$  is the length,  $J$  is the polar moment of inertia, and  $G$  is the shear modulus.

### **Ultrasonic Testing**

Ultrasonic testing of material properties is a non-destructive technique that is capable of providing elastic properties. A single specimen can be used to determine several anisotropic properties, and therefore the technique may be advantageous over mechanical testing techniques. Elastic properties are found by measuring wave velocity and inputting known specimen densities into simple formulas. These formulas relate the speed of the wave and the apparent density of the material to the elastic constants of Hooke's law. Various specimen geometries can be used to determine material properties. Cube specimens with chamfered edges (Figure 2-5) are capable of providing measurement of 18 velocities (three in each of six directions) when ultrasonic waves

are passed through the specimen at various angles. These velocities provide sufficient information to determine all 9 independent elastic constants of an orthotropic material. However, thin, square-shaped specimens with a chamfer on two opposite corners (Figure 2-5) can provide only 9 velocities, and 2 of the 9 independent elastic constants cannot be measured with this geometry (Rho, 1996). Yan (2002) used thin, square specimens to determine a single elastic modulus, Poisson's ratio, and shear modulus for manatee bone.

### **Visual Image Correlation (Speckle Image Photogrammetry)**

Traditional measures of material properties involve the use of extensometers or strain gages to measure the response of a specimen to loading. These measures provide a *representative* value of deformation or strain over the gage section of a specimen, thus much of the data across the gage section is lost. For some heterogeneous materials, there may be considerable variation in deformation within the gage section. A full-field deformation analysis is necessary to describe the constitutive relations for these non-homogeneous materials. In addition, understanding how every point in the gage section is behaving during a full-field deformation analysis increases the amount of data available for material property calculations over traditional measurement techniques.

One method to obtain full-field data over a specimen gage section is to use photogrammetry, which provides 3-dimensional coordinates of points on an object from 2 images. Photogrammetry uses a technique called spectroscopy, whereby two cameras are placed at some distance from one another and focused on the same object. Images from these cameras are taken simultaneously in order to create a stereoscopic view of the object. Points on the object are then correlated between the images to provide object feature representation in 3D space.

A specialized form of photogrammetry is speckle image photogrammetry (SIP), also known as visual (or digital) image correlation (VIC). Visual image correlation requires that an

array of speckles be applied to an object such that the speckles contrast the color(s) of the object. In general, gray-scale images are used for the correlation analysis. Cross-correlation (CC) and normalized cross-correlation (NCC) are commonly used methods to determine object features (e.g., points, edges, etc.).

Once the images have been correlated for a reference image of an unloaded specimen, the specimen is loaded and more stereoscopic images are taken. The position of the points in the deformed specimen images are compared to those from the reference image, and the full-field deformation of the specimen gage section can be found. In addition, commercial software packages are available that apply algorithms to further reduce the data to strains, deformation rates, strain rates, etc.

### **Deformation accuracy**

The accuracy of the full-field deformation analysis is in excess of  $1/100^{\text{th}}$  of a pixel when using VIC3D v3.1 (Correlated Solutions, Inc.). For out-of-plane deformation, accuracies vary as a function of the angle between the specimen and the cameras. Out-of-plane accuracy decreases with reduced camera spacing, while accuracy (in general) decreases as the camera/specimen positions deviate from equilateral. It is estimated that the out-of-plane accuracy is about  $\frac{1}{2}$  the in-plane accuracy for angles approaching equilateral (Simonsen, 2006). Strains are considered accurate from  $500 \mu\epsilon$  to 500% when using VIC3D software.

Visual image correlation is a relatively new technique that can be used to determine deformation and strain rate of any point on a specimen. It is generally accepted that cross-head displacement be used for the calculation of deformation in a specimen as well as to calculate the strain rate of a test. However, specimen slip and compliance of the test rig reduce the accuracy of these measures, making VIC a more attractive approach to this measure.

### **Mirrored image correlation**

Mirrored image correlation (MIC) is a technique that was developed for this study to provide full-field information on multiple specimen faces simultaneously, thus reducing the number of tests required to capture the full constitutive response of an anisotropic body.

Mirrored image correlation involves the placement of mirrors in strategic locations to simultaneously view the desired specimen surfaces with both cameras. The simplest case of MIC involves the placement of a single mirror behind a specimen. The mirror is placed close enough to the specimen that the speckle patterns on both the reflected and non-reflected specimen images remain in focus. At the same time, the mirror must be located far enough from the specimen in order to view the reflected specimen image with both cameras. A camera lens with a long focal length is recommended when performing MIC.

More specimen surfaces must be in view of the cameras than when using SIP alone, causing a need to move the cameras further from the specimen. Also, mirror placement may require special fixtures and careful positioning. Thus, the drawbacks of using MIC during SIP include increased set-up time and reduced image resolution.

### **Rotated specimen method**

Another method that can be used to increase the amount of data available for calculation of material properties is the rotated specimen method (RSM), whereby a specimen with a polygonal cross-section is oriented relative to the cameras to maximize the viewing area of each specimen face. For an orthotropic material, a square cross-section provides the simplest case whereby material properties can be calculated. Therefore, discussion in this document is limited to a specimen with a square cross-section oriented at a  $45^\circ$  angle relative to the midline between the cameras.

Similar to MIC, a drawback of RSM is a reduction in image resolution compared to non-RSM MIC or VIC, since fewer pixels are associated with each face. Thus the combination of RSM and MIC significantly reduces the resolution of a full-field deformation analysis. However, the benefits of viewing all specimen surfaces during the analysis may outweigh the decrease in resolution for certain tests, depending on the resolution needs of the particular analysis. Should reduced resolution be an issue, higher resolution cameras can be incorporated in the analysis fairly inexpensively to make up for the loss of resolution associated with the combination of RSM and MIC.

### **Fracture Tests**

The failure of a material is governed by the type of material being analyzed (e.g., brittle vs. ductile), the microstructure of the material, and environmental factors such as the temperature and humidity levels at which the fracture test is performed. Several tests have been standardized for the determination of the fracture properties of a material (e.g., ASTM E399, E561, E1820, and C1421). Several of these tests and others are described below since results from these tests have been conducted on manatee rib bone and their results will be used for comparison to fracture toughness values found during the current study.

### **Single Edge V-Notched Beam (SEVNB) Tests**

Yan et al. (2006b) used single edge V-notched beams (SEVNB) to analyze fracture in manatee rib bone. Although this method is not currently standardized, other authors have successfully applied the method to alumina, silicon nitride, and dental ceramics (Kubler, 1997 and 2002; Fischer and Marx, 2002). Figure 2-6 shows the dimensions and orientation of SEVNB specimens used in Yan et al.'s study. Figure 2-7 shows a close-up of the V-notch introduced to a notched bend specimen.

### **Chevron-Notched Beam Tests**

Chevron-notched (CN) specimens have several advantages over other methods (Yan, 2006c). Plane strain conditions at the crack tip are reached more easily than with other fracture specimens. This allows for smaller specimens to be prepared, thus more specimens can be obtained from a single bone. Also, cortical bone is generally not very thick and testing of three orthogonal orientations of bone is not always possible. Therefore, thicker specimens may not be practical for fracture testing of cortical bone. Pre-cracking a specimen is not necessary with CN specimens, since the shape of the notch allows for the specimen to pre-crack easily during loading. The notches also help guide the crack to prevent crack turning from occurring, which often happens in transverse specimens. Also, a sharp crack is formed early during loading, and therefore special techniques are not required to introduce a sharp crack. Failure in CN specimens is stable, whereas crack growth is unstable for most fracture specimen geometries. Figure 2-8 shows a CN specimen along with the notch and appropriate dimensions.

### **Three Point Bend Tests**

Yan et al. (2006a) studied fracture in manatee rib bone using three point bend tests with no pre-crack or notch introduced prior to loading (Figure 2-9). Fractography was used to identify the origin of the flaw which caused catastrophic failure as well as to determine the critical flaw size that led to failure. Correction factors were implemented to determine the critical stress at the flaw if failure initiated anywhere other than at the center of the specimen.

### **Quantitative Fractography**

Quantitative fractography is a method that locates the source of failure in a specimen and relates the fracture features to the failure stress (Yan et al., 2006a). Using this technique, fracture surfaces can be analyzed to determine artifacts such as failure mode, crack origin, and critical flaw size and to determine fracture toughness without the need to introduce pre-cracks into a

specimen. Scanning electron microscopy (SEM), a tool used in quantitative fractography, uses a focused electron beam to scan the surface of a specimen. There is backscatter of primary electrons and ejection of secondary electrons during SEM scanning. A positively charged collector attracts the ejected secondary electrons and the signal is amplified and displayed on a cathode ray tube. A conductive coating is generally applied to a specimen prior to SEM scanning to allow for sufficient electron ejection and backscatter. However, low-vacuum SEM and field emission (FE) SEM allow for the specimen to be observed without chemical fixation, dehydration, drying and coating (An and Draughn, 2000). These techniques use backscattered electron images that provide both composition contrast and contrast caused by specimen topography over a long focal length compared to microscopy techniques. Image analysis software can be used to determine microstructural artifacts present in the images produced by SEM, including porosity. Microstructural artifacts have been shown to have a strong influence on fracture parameters in bone (Akkus et al., 2005). Therefore it is good practice to compare the microstructure of specimens if fracture properties are going to be compared.

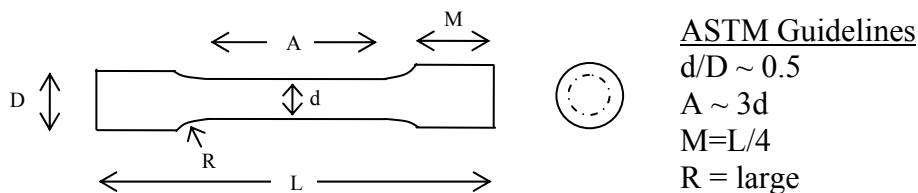


Figure 2-1. ASTM tensile specimen recommendations.

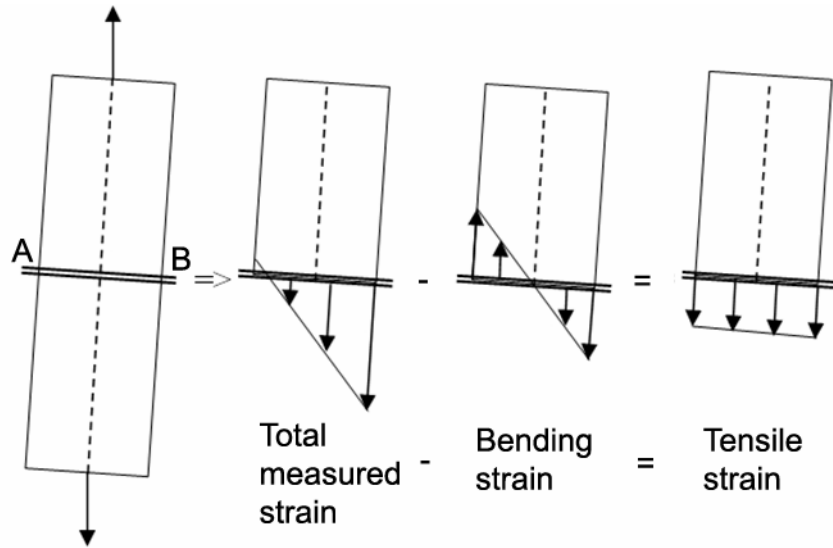


Figure 2-2. Tensile specimen with some bending present. Averaging the total measured strain at points A and B of the above specimen removes the bending component of strain and we are left with only the tensile strain.



Figure 2-3. Iosipescu shear specimen. This specimen is loaded uniaxially in order to generate nearly pure shear in the gage section.

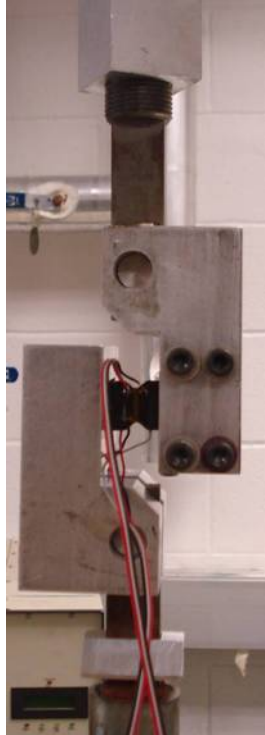


Figure 2-4. Iosipescu shear specimens fitted in grips on a uniaxial testing machine. Image courtesy of Nancy Strickland (University of Florida, Mechanical and Aerospace Engineering).

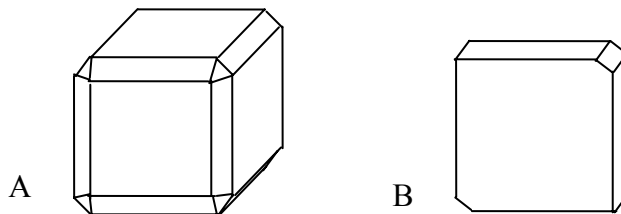


Figure 2-5. Ultrasonic test specimen geometries (A) cube used to obtain 18 velocities; B) shape used to obtain 9 velocities).

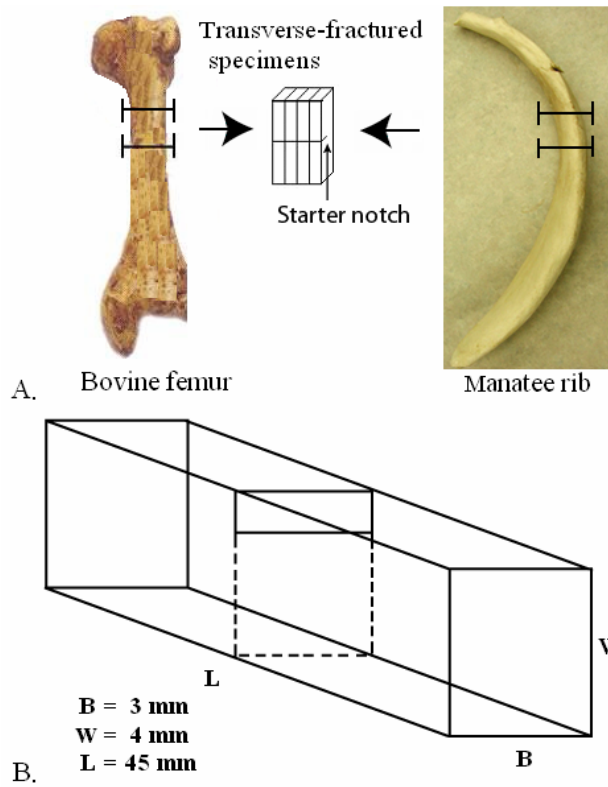
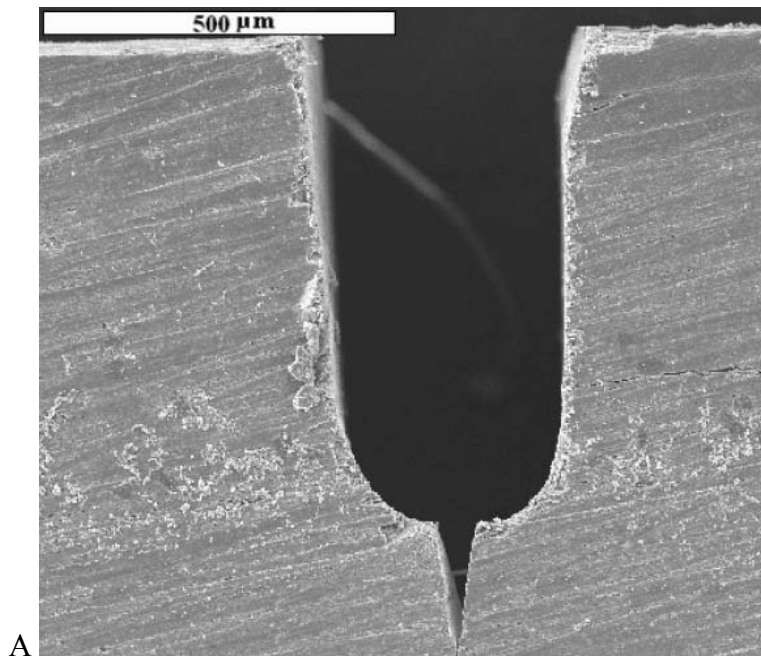
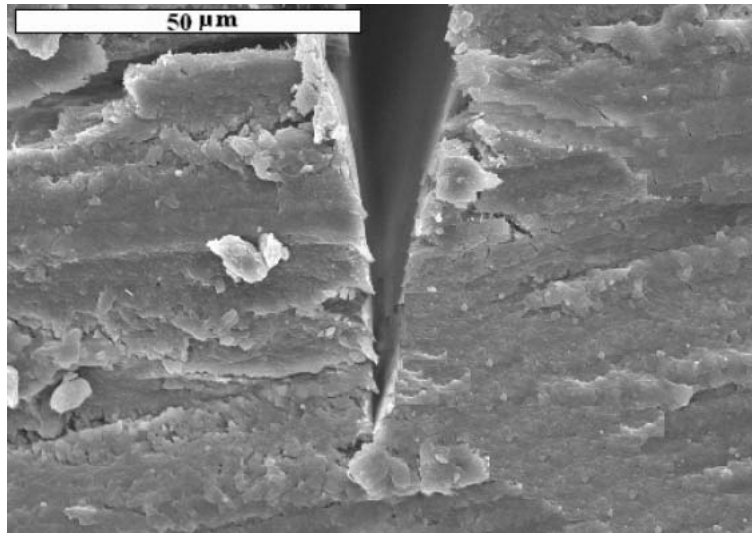


Figure 2-6. Single edge V-notched beam (SEVNB) specimen. Reproduced with permission from Yan, J., 2005. Elastic-plastic fracture mechanics of compact bone. Ph.D. thesis, University of Florida, Gainesville, Figure 3-2, p. 30.





B  
 Figure 2-7. A) Close-up of the notch in an SEVNB specimen. B) Close-up of the v-notch in an SEVNB specimen. Reproduced with permission from Yan, J., 2005. Elastic-plastic fracture mechanics of compact bone. Ph.D. thesis, University of Florida, Gainesville, Figure 3-1, p. 28.

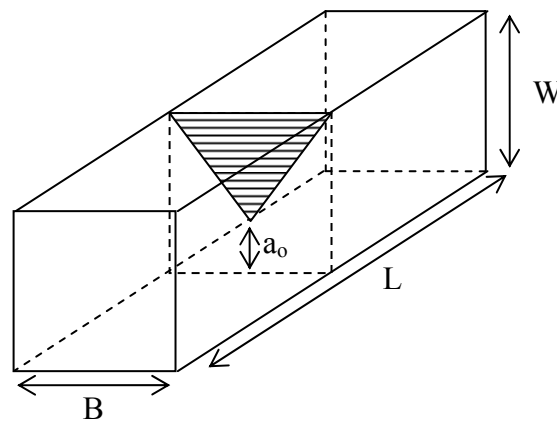


Figure 2-8. Chevron-notched (CN) specimen.

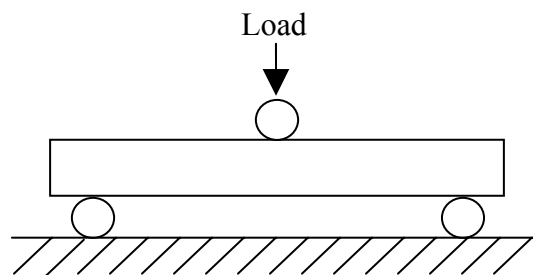


Figure 2-9. Three-point bend specimen and loading constraints.

CHAPTER 3  
BONE FRACTURE MECHANICS

**Fracture in Engineering Materials**

Stress fields have been analyzed in the vicinity of a crack-tip by many authors for the isotropic case (Westergaard, 1939; Irwin, 1939; Irwin 1949; Williams, 1957; Gross and Srawley, 1964; Sih, 1973). According to Griffith, the critical stress that causes the crack to propagate is

$$\sigma_C = [2E\lambda/(\pi a)]^{0.5} \quad (\text{Eq. 3-1})$$

where  $E$  is the elastic modulus and  $\lambda$  is the fracture surface energy.

Orowan (1950) extended Griffith's theory to include ductile materials by accounting for the energy dissipated by local plastic flow:

$$\sigma_C = [2E(\lambda + \lambda_p)/(\pi a)]^{0.5} \quad (\text{Eq. 3-2})$$

where  $\lambda_p$  is the energy due to plastic deformation.

Irwin built on Orowan's work by introducing the fracture parameter,  $G$ , the strain energy release rate, in 1956.

$$G = -dP/da = dW/da - dU/da \quad (\text{Eq. 3-3})$$

where  $P$  is the potential energy of the system,  $a$  is the crack half length,  $W$  is the work done by external forces per unit thickness, and  $U$  is the strain energy per unit thickness. Equation 3-3 says that the energy due to plastic deformation must be added to the energy associated with generation of new crack surfaces. The strain energy release rate is a measure of the change of elastic energy per change of crack length.

Alternatively,  $G$  can be expressed as

$$G = 2(\lambda + \lambda_p). \quad (\text{Eq. 3-4})$$

Irwin next introduced the stress intensity factor, a measure of the intensity of the stresses in the vicinity of a crack (Irwin, 1957). According to ASTM E-399,  $K$  can be determined from the following equation:

$$K = P*Y(a/W)/(B*W^{0.5}) \quad (\text{Eq. 3-5})$$

where  $P$  is the load,  $B$  is the specimen thickness,  $W$  is the width, and  $Y$  is the shape function, which is also known as the geometry factor. The shape function can take several forms depending on the specimen and loading scenario.

$Y_{CT} = (2+a/W)/(1-a/W)^{3/2} \{.866 + 4.64(a/W) - 13.36(a/W)^2 + 14.72(a/W)^3 - 5.6(a/W)^4\}$  for the compact tension (CT) specimen (Figure 3-1), and

$$Y_{SENB} = 3*S/W*(a/W)^{0.5}/[2*(1 + 2(a/W))*(1 - (a/W))^{3/2}] * \{1.99 - (a/W)*(1 - (a/W)) * [2.15 - 3.93(a/W) + 2.7(a/W)^2]\}$$

where  $S$  is the spacing between reaction loads in a single edge notched bend (SENB) specimen (Figure 3-2).

The elastic stresses near the tip of a crack can be found as a function of  $K$  using the following relation:

$$\sigma_{ij}(\omega) = K*f_{ij}(\omega)/(r)^{0.5} + \text{higher order terms} \quad (\text{Eq. 3-6})$$

where  $\sigma_{ij}$  are the component stresses,  $\omega$  and  $r$  are defined in Figure 3-3,  $f_{ij}$  is a dimensionless function of  $\omega$ , and the *higher order terms* reduce to zero or remain finite as  $r$  approaches zero, while the leading term approaches infinity (Anderson, 1991).

The critical stress intensity factor of a material is also known as the fracture toughness. The fracture toughness,  $K_{Ic}$ , of a material is defined as the critical SIF at or above which stable crack

propagation occurs. The fracture toughness of a material depends on load, crack geometry, and specimen thickness, but it is independent of material properties. Fracture toughness is calculated as

$$K_C = \sigma_Y C (\pi a_C)^{0.5}, \quad (\text{Eq. 3-7})$$

where  $\sigma_Y$  is the yield strength and  $C$  is a geometry factor and  $a_C$  is the critical crack length leading to failure.

Opening mode fracture toughness is denoted as  $K_{IC}$ . Here, the subscript  $I$  tells us that the crack is subjected to mode I loading. The three types of loading a crack can experience are summarized in Figure 3-4. Mode I loading signifies that loads are applied normal to the crack plane, thus causing a crack to open. Mode II loading is the shearing mode, whereby in-plane shear loading slides one crack face relative the opposite face. Mode III loading results in tearing due to out-of-plane shearing.

The stress intensity factor approach to fracture mechanics requires an analysis of the stresses about a crack-tip, which presents some difficulty for anisotropic materials. To date, there are very few analysis tools capable of computing stresses about a crack tip in an anisotropic material such as bone. Therefore, other approaches are generally used to analyze fracture in bone.

The strain energy release rate approach is equally valid for iso- and aniso-tropic materials. The strain energy release rate approach is based on the crack tip opening displacement method, whereby the crack tip displacements are related to the strain energy release rate (Gibson, R., 1994). The strain energy release rate of a material is not influenced directly by microstructural features of a material, and thus provides an adequate representation of the global behavior of a

material with complex microstructure such as bone (Norman, 1995). For an isotropic material, the strain energy release rate,  $G$ , as it relates to  $K$  is given as

$$G = K^2/E' \quad (\text{Eq. 3-8})$$

where  $E' = E/(1-\nu^2)$  for plane strain,  $E' = E$  for plane stress, and  $\nu$  is Poisson's ratio. Since  $G$  is a scalar, this relationship between  $G$  and  $K$  can be further delineated into individual loading modes with the following equation (Anderson, 1991):

$$G = K_I^2/E' + K_{II}^2/E' + K_{III}^2/(2\mu) \quad (\text{Eq. 3-9})$$

where  $\mu$  is the shear modulus. Note that later discussions refer to shear modulus as  $G$ , while it is reported as  $\mu$  in this chapter to differentiate it from strain energy release rate.

For an anisotropic material, the relationship between  $K$  and  $G$  is given by Liebowitz (1968) and Sih (1965) as

$$G = K^2(b_{11}b_{22}/2)^{0.5} [(b_{22}/b_{11})^{0.5} + (2b_{12} + b_{66})/(2b_{11})]^{0.5} \quad (\text{Eq. 3-10})$$

where

$$b_{11} = (a_{11}a_{33} - a_{13}^2)/a_{33}, \quad b_{12} = (a_{12}a_{33} - a_{13}a_{23})/a_{33}, \quad b_{22} = (a_{22}a_{33} - a_{23}^2)/a_{33}, \quad b_{66} = (a_{66}a_{33} - a_{36}^2)/a_{33}$$

for plane strain, and

$$b_{11} = a_{11}, \quad b_{12} = a_{12}, \quad b_{22} = a_{22}, \quad b_{66} = a_{66}$$

for plane stress.

$$a_{11} = 1/E_1, \quad a_{13} = -\nu_{13}/E_1, \quad = -\nu_{31}/E_3,$$

$$a_{22} = 1/E_2, \quad a_{23} = -\nu_{23}/E_1, \quad = -\nu_{32}/E_3,$$

$$a_{33} = 1/E_3, \quad a_{12} = -\nu_{12}/E_1 = -\nu_{21}/E_2,$$

$$a_{36} = 0 \text{ (due to elastic symmetry)}, \quad a_{66} = 1/G_{12}.$$

Another method used to evaluate fracture is the J-integral approach (Rice, 1968a, b), which uses a path-independent line integral that measures the strength of the singular stresses and strains near a crack tip. For the 2D case,  $J$  is defined as

$$J = \int_{\Gamma} W dy - \int_{\Gamma} (T_x \delta u / \delta x + T_y \delta v / \delta y) ds \quad (\text{Eq. 3-11})$$

where  $\Gamma$  is any path enclosing the crack tip (Figure 3-5),  $W$  is the strain energy density ( $W = \sigma_{ij} \epsilon_{ij} / 2$ ),  $T_x$  is the traction vector along the  $x$ -axis ( $T_x = \sigma_x n_x + \sigma_{xy} n_y$ ),  $T_y$  is the traction vector along the  $y$ -axis ( $T_y = \sigma_y n_y + \sigma_{xy} n_x$ ),  $\sigma$  is the component stress,  $n$  is the unit outer normal vector to path  $\Gamma$ ,  $u$  is the  $x$ -direction displacement vector,  $v$  is the  $y$ -direction displacement vector, and  $s$  is the distance along the path  $\Gamma$ .

The J-integral is related to  $G$ , where for small scale yielding,

$$J = K^2 / E' \quad (\text{Eq. 3-12})$$

where  $E'$  is the same as in Equation 3-8. Furthermore, by comparison with Equation 3-12, it can be noted that  $J = G$  for the linear range of a material, and that  $J_C = G_C$  for materials that exhibit linear elastic behavior up to failure.

A limitation with the J-integral approach is that the individual  $K$ s cannot be delineated for the mixed mode crack problem (Knudsen, 2006). Therefore, another approach is necessary to find individual  $K$ s. The present study will overcome the inherent hurdles associated with finding an anisotropic crack-tip stress solution by implementing a numerical technique developed specifically for this type of problem by the Cornell Fracture Group (FRANC3D, Cornell Fracture Group, Ithaca, N.Y.). The Cornell Fracture Group developed a software program called FRANC3D, which is an acronym for Fracture Analysis Code 3D, to simplify the analysis of fractures. The mathematical formulations used by FRANC3D are omitted from this document

due to their lengthy derivations. The reader is encouraged to review Knudsen (2006) for more information on this topic.

### **Fracture Testing of Bone**

There has been a significant amount of work done in the area of fracture testing of bone dating back to the early 1970s. Most often reported in the literature are values of fracture toughness ( $K_C$ ) and critical strain energy release rate ( $G_C$ ). However, there is much debate in recent times on the validity of using  $K_C$  to describe bone fracture, since recent work by Nalla et al. (2005) demonstrated the importance of reporting fracture resistance as a function of crack length (resistance-curves or R-curves for short) as opposed to reporting a single value of fracture toughness. In addition, many of the models used to describe bone fracture are limited by isotropic assumptions, which is a major source of error when it comes to modeling anisotropic materials such as bone. Another major problem in the literature is the lack of orientation dependent properties reported. Most authors report fracture toughness for a single orientation of cortical bone, because the animal model chosen does not support large specimen sizes to be harvested for all orientations.

Bone fracture literature can be segmented into several categories based on the animal species studied, the age of the animal from which the bone was harvested, the type of bone analyzed (cortical vs. trabecular), the level of bone hierarchy selected for analysis, and the location from which the bone was harvested. These categorizations are necessary due to the extreme variation in material and fracture properties between each category.

#### **Validity of using LEFM to Model Bone Fracture**

Fracture testing of bone is most often done according to ASTM E399 (Standard test method for plain strain fracture toughness testing of metallic materials) and ASTM E561 (Standard practice for R-curve determination), which were designed for linear elastic materials.

The linear elastic assumption is important, since  $K$  and  $G$  methods are based on LEFM. There is some debate over the validity of the linear elastic assumption for bone, since the viscous nature of the material results in some degree of non-linearity prior to fracture. However, LEFM remains the standard in the literature for the determination of bone fracture properties.

### **Rising R-curve Approach to LEFM**

The rising resistance curve (R-curve) approach to LEFM accounts for materials which display microstructural toughening mechanisms. The toughening mechanisms are responsible for increasing fracture resistance,  $K_R$ , with increasing crack length. Note that  $K_R$  is equal to  $K_C$ , but it is differentiated when referring to R-curve materials. Toughening mechanisms include, but are not limited to crack turning at the cement line interface between an osteon and the interstitial matrix which surrounds the osteon, crack tip blunting at the weaker cement line interface, microcracking, crack bridging by uncracked ligaments, crack bridging by collagen fibrils, osteon pull out, and osteon micro-rotation. Several models of these microstructural toughening mechanisms have been implemented in bone fracture mechanics studies to account for their relative contribution to the fracture toughness of human cortical bone (Nalla et al., 2005).

### **Elastic-Plastic Fracture Mechanics (EPFM)**

Elastic-plastic fracture mechanics (EPFM) are equally valid for both elastic and inelastic materials. The J-integral approach is widely used for the determination of elastic-plastic fracture properties, and it was recently implemented by Yan (2005) to model fracture in manatee and bovine cortical bone. Yan (2005) found that the energy spent propagating a crack in the plastic regime was greater than the energy expended in the linear elastic range of bovine bones. This calls to question the validity of the linear elastic assumption of LEFM models of bone.

## Testing Procedures

In brittle materials, such as bone, it is difficult to cause failure in Modes II and III, thus Mode I is the main mode of failure generally reported (e.g.,  $K_{IC}$ ). Testing procedures used to determine  $K_{IC}$  generally involve monotonic loading of a notched or pre-cracked specimen under constant load or displacement rate. The resulting load-displacement curve is used in fracture property calculations. The curve tends to be linear at start and deviates from linear prior to catastrophic crack propagation. The stress intensity factor or strain energy release rate can be calculated from the load-displacement curve and a geometry factor which is a function of crack length and specimen geometry (Equation 3-5).

Compact tension (CT) specimen geometries predominate the wealth of  $K$  and  $G$  experiments since the specimens are in accordance with standard test techniques and there exists much control over the loading rate (Akkus et al., 2004). However, other fracture tests are often employed as well. Several researchers have used three-point bend tests to determine the fracture toughness of cortical bone (Nalla et al., 2005b; Clifton, 2005; Yan, 2005). Yan (2005) used single-notched four-point bend tests, while Nalla et al., (2005b) used double-notched four-point bend tests to analyze fracture properties of cortical bone. Compact sandwich specimens (CSS) are sometimes used for smaller specimens that can not be analyzed using CT tests (Wang et al., 1996).

## Anisotropic Fracture Analysis of Bone

A substantial body of literature exists on the fracture mechanics of bone. The bulk of the literature is confined to reports of fracture properties for a single mode of fracture for one orientation of bone (Cooke et al., 1973; Pope and Murphy, 1974; Wright and Hayes, 1976; Wright and Hayes, 1977; Alto and Pope, 1979; Behiri and Bonfield, 1980; Behiri and Bonfield, 1984; Moyle and Gavens, 1986; Bonfield, 1987; Norman et al, 1991; Norman et al., 1995;

Zioupos and Currey, 1998; Yeni and Norman, 2000). Most of the existing literature neglects the anisotropic nature of bone, and hence, valuable information on orientation-dependent fracture properties is not always presented. There exists only a small body of literature that investigates anisotropic fracture properties of cortical bone (Bonfield, et al., 1985; Bonfield, 1987; Behiri and Bonfield, 1989; Hoffmeister et al., 2000; Lucksanambool et al., 2001; Nalla et al., 2005b). Nalla et al. (2005b) found  $K_C$  in human cortical bone to be between 51-140% greater for cracks propagating in the transverse direction relative long bones than for the cracks propagating in the longitudinal direction. The increase in transverse orientation toughness is the result of a  $\sim 90^\circ$  kink, or deflection, in the crack's path. Yeni and Norman (2000) found that cracks can deflect from a transverse direction of propagation to grow along the cement line interface between an osteon and the surrounding mineral matrix. The cement line acts as a path of least resistance, causing the crack to redirect away from the nominal path of maximum stress.

Akkus and Rimnac (2001) excluded from fracture toughness calculations fatigue cracks that delineated from initial crack growth direction by more than 20%, since the fracture toughness formulation they used (Zeng and Dai, 1994) assumes that cracks remain straight. Crack deflection can lead to erroneous calculations of fracture toughness if the crack deviates substantially from its initial growth direction (ASTM E-399), therefore other measures of fracture are generally obtained for the transverse orientation (Nalla et al., 2005b). Nalla et al. (2005b) used work-of-fracture,  $W_f$ , as an alternative measure of toughness. Work-of-fracture is obtained by dividing the area under the load-displacement curve by two times the nominal crack surface area. This fracture evaluation method has its limitations, since  $W_f$  is size and geometry-dependent.

Alternatively, several authors have placed grooves along the gage section of transverse fracture specimens to remove the crack kinking effect (Behiri and Bonfield, 1989; Norman et al., 1992; Malik, 2003). The components of the fracture toughness equation are modified according to Malik (2002) in order to account for the effects of the groove (Equation 3-13)

$$K_{R, grooved} = PY/[ (BB_n)^{0.5} W^{0.5} ] \quad (\text{Eq. 3-13})$$

where  $B_n$  is the thickness measured in the grooves and the other components correspond with those of Equation 3-5.

In summary, bone is a highly complex material that requires special treatment when analyzing its properties. Standard test procedures for engineering materials can be modified to accommodate the unusual characteristics of bone.

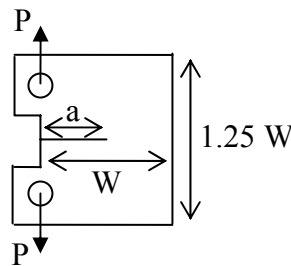


Figure 3-1. Compact tension (CT) specimen dimensions.

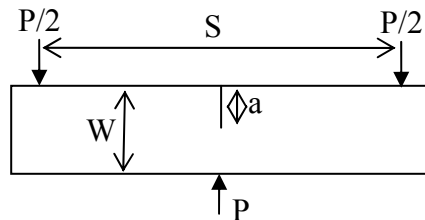


Figure 3-2. Single edge notched bend (SENB) specimen dimensions.

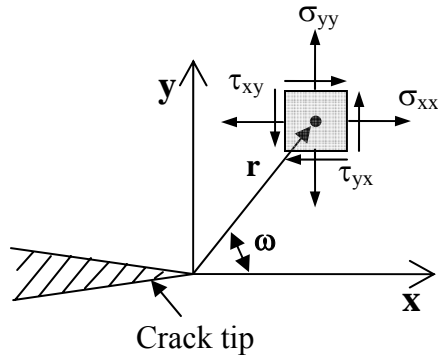


Figure 3-3. Definition of the coordinate system associated with a crack tip.

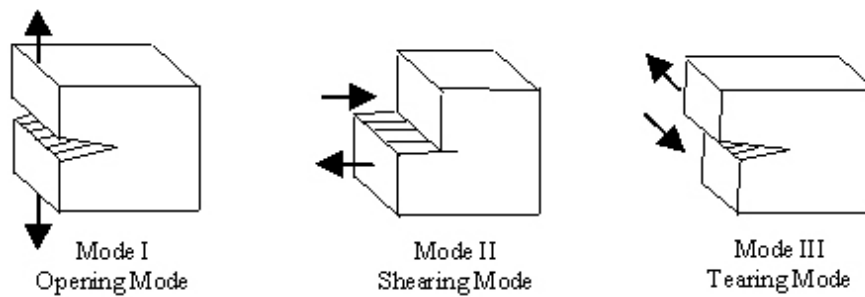


Figure 3-4. Three modes of failure: Mode I is the opening mode, whereby loading occurs normal to the crack plane; Mode II is the shearing mode, whereby in-plane shear loading slides one crack face with respect to the other; Mode III is the out-of-plane shearing mode, also known as the tearing mode.

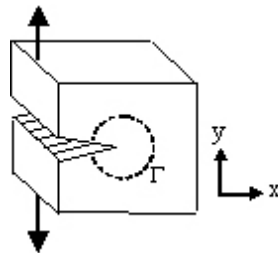


Figure 3-5. Path,  $\Gamma$ , enclosing the crack tip used for the J-integral formulation.

## CHAPTER 4 OVERVIEW AND ORGANIZATION OF THE EXPERIMENTS

This chapter concisely describes the experiments which are presented at greater length in the remaining chapters in order to put the experiments into perspective. Tables 4-1 through 4-3 provide information on each of the experiments performed in this study such as the number of specimens analyzed and the output variables from each experiment. The remaining chapters are organized as papers for publication in refereed journals with the exception of Chapter 10 which provides the concluding remarks of this dissertation. As such, some of the material from the introductory chapters (1 through 3) and the remaining chapters (4 through 9) will be repeated in the remaining chapters to allow for each chapter to serve as a stand-alone article. An appendix appears at the end of this document to present work not included in the remaining chapters, since the material falls outside the scope of the articles or exceeds page limitations of the journals to which the remaining chapters will be submitted.

### **Overview of the Experiments**

#### **Pilot Tensile Tests**

The initial experiment was a tensile test conducted on 9 specimens oriented about 3 orthogonal axes ( $n=3$  for each orientation). It was unknown how well the speckle pattern could be applied to wet bone specimens, so the pilot tensile test specimens were air-dried at room temperature in an air-conditioned room (for 2 weeks) prior to testing. The specimens were loaded to failure at a constant load rate (1 mm/min). Mirrored image correlation (MIC) was used to capture deformations on the front and back specimen gage sections while a load cell was used to capture load data during the experiment. Outputs from these tests included three elastic moduli (for the proximodistal, superficial-deep, and craniocaudal orientations, respectively) as well as six Poisson's ratios. This was possible because for a given orientation, two specimen faces ( $90^\circ$

from one another) were analyzed. Because of the limited number of specimens used in this experiment, only one or two specimens were used to determine each Poisson's ratio. This pilot study aimed to:

- Determine the elastic modulus for 3-orientations of manatee rib bone using MIC.
- Determine the Poisson's ratio for several orientations of manatee rib bone using MIC.
- Compare MIC results with those from three-point bend and ultrasound studies.
- Characterize the anisotropy of manatee rib bone elastic modulus.
- Evaluate the ability of the test fixtures to prevent specimen bending by determining if results significantly differ on the front and back of a specimen.
- Investigate the linearity of the material for each orientation.
- Provide a list of the benefits and draw backs of VIC relative to traditional deformation and strain measurement techniques.

### **Tensile Tests**

This experiment consisted of loading and unloading 39 wet bone specimens (13 from each orthogonal orientation) within their elastic range at a rate of 1 mm/min, then rotating the specimens 90 degrees and repeating the loading and unloading cycle. Mirrored image correlation (MIC) was used to determine elastic modulus and Poisson's ratios associated with each load cycle. These tests provided elastic modulus in 3 presumably primary orthogonal directions of manatee rib bone as well as Poisson's ratios on both pairs of faces for specimens oriented in each of 3 orthogonal directions. The tensile test study aims were to:

- Determine the elastic modulus for 3 orientations of manatee rib bone using MIC.
- Determine the Poisson's ratio for 3 orientations of manatee rib bone using MIC.
- Characterize the anisotropy of manatee rib bone tensile properties.

## Shear Tests

Shear testing was done in order to determine the shear modulus of three orientations of manatee rib bone. Iosipescu (shear) specimens were used in order to produce nearly pure-shear in the specimen gage sections. Iosipescu specimens have been evaluated many times over in the investigation of shear properties. Shear gages were thought to be the most accurate way to measure strain in the Iosipescu specimens, and were placed on the front and back of 9 wet bone specimens. Three specimens were oriented to obtain each of  $G_{12}$ ,  $G_{23}$ , and  $G_{32}$ , shear moduli for two orthogonal orientations of manatee rib bone (note that  $G_{23}=G_{32}$ ). Visual image correlation (VIC) was performed over the top of shear gages in order to evaluate the feasibility of using VIC in the determination of shear modulus. Shear strain from the strain gages was averaged over the front and back of the specimens, while strains were monitored by the VIC system on only one specimen face. Two additional wet bone specimens ( $G_{13}$ ) each had a shear gage applied to only the front face. VIC and shear gage acquisition were performed simultaneously on these specimens. The specimens were loaded in a cyclic manner to determine the repeatability of loading (i.e., was there property degradation with loading and how much variability exists in shear modulus when loading the same specimen several times?). Seven additional (wet)  $G_{13}$  specimens had VIC performed on them in the absence of shear gages. All loading was done at a rate of 1 mm/min. Output from these tests included shear modulus for three presumably primary orthogonal orientations of manatee rib bone. The shear study aimed to:

- Determine the shear modulus for 3-orientations of manatee rib bone using both VIC and shear gages.
- Determine the repeatability of each technique by performing cyclic tests and looking at the coefficient of variation ( $CV$ ) for all cycles.
- Determine if VIC is a viable alternative to shear gages in the calculation of shear modulus.

### **Off-Axis Tensile Tests**

Twenty-two wet bone specimens oriented along three “off-axis” directions, [110], [101], and [001], were loaded and unloaded within the elastic range of the material at a rate of 1 mm/min. Specimens were rotated 90° about their longitudinal axis and the load cycle was repeated in order to assess Poisson (lateral) strains on all specimen surfaces. A third loading was done to failure. Mirrored image correlation was used to sequester Poisson and normal strains on the specimen faces during testing. Several failed specimen fracture surfaces were scanned with a scanning electron microscope (SEM) to allow for critical crack lengths to be measured. Failed specimens were scanned on a high resolution scanner in order to measure the crack angle of each specimen. The aims of the off-axis study were to:

- Determine Poisson and normal strains in the gage section of off-axis specimens.
- Determine failure load of off-axis specimens of various orientations.
- Use fractography to determine critical crack lengths in failed specimens.
- Measure crack angles from scanned images of failed specimens.

### **Variable Strain Rate Tensile Tests**

Visual image correlation was performed on the crosshead of the universal testing machine operating in the absence of a load in order to determine velocity of the crosshead at three speed settings. The speed settings were adjusted by manipulating the position of a rheostat on the universal testing machine. The position of the rheostat was noted for three crosshead speeds, 1 mm/min, 2 mm/min, and 5 mm/min and the positions were marked on the universal testing machine in order to achieve the same crosshead speeds for each test. The same three rheostat settings were used while loading four medial-lateral and four anterior-posterior specimens fixed with strain gages. The specimens were loaded cyclically (3-5 times each at 1 mm/min) within the linear range of the material to check for hysteresis. Several specimens were also loaded

cyclically into the nonlinear range to assess the viscoelasticity of the material. The loading cycles were repeated at each of the remaining rheostat settings in order to determine the effect of increased strain rate (calculated from crosshead speed and the specimen gage length) on elastic modulus. It took several weeks to modify the Labview code used to read in strain values from the specimens (after the specimens were already fitted with strain gages) and modifying the code required that specimens be attached to the National Instruments equipment that received the strain readings, thus the specimens were air dried prior to testing.

Unfortunately, equipment malfunction at the time of this experiment prevented crosshead speeds from varying between rheostat settings except for during the testing of a single specimen (see data in Appendix A). This limited data provides a more thorough understanding of the viscoelastic behavior of manatee rib bone when put together with the results of the cyclic tests.

The aims of this study were to:

- Determine whether or not manatee rib bone is viscoelastic based on the presence or absence of hysteresis
- Determine the dependence of elastic modulus on strain rate (another indicator of viscoelasticity).

### **Notched Tensile Tests**

The same wet bone specimens used in the tensile test experiment along with 8 additional wet bone specimens were prepared for fracture testing. Specimens were wrapped in gauze, soaked in saline solution, and refrigerated until bringing them back to room temperature before testing. Notches were inserted ~1-1.5 mm deep on 2 opposite specimen faces using a diamond-tipped wafering saw followed by inserting v-notches at the end of the larger notches by pressing a razor blade into the notch tips. The v-notches were inserted in lieu of fatigue pre-cracks. Six to twelve specimens were prepared for each orientation in order to later obtain each of 6 fracture toughness values ( $K_{I2}$ ,  $K_{I3}$ ,  $K_{23}$ ,  $K_{21}$ ,  $K_{31}$ , and  $K_{32}$ ). Specimens were loaded to failure at a rate of 1

mm/min. Failure load was recorded for each specimen. MIC was performed on each specimen in order to have images available for the measurement of notch (crack) lengths. This study aimed to:

- Determine the failure load for each specimen and crack orientation.
- Determine crack lengths for each specimen.

### **Numerical Fracture Tests**

A 3-dimensional, orthotropic finite element model of the notched tensile specimen was prepared in order to assess the fracture toughness of manatee rib bone. Material properties found from the previous studies were inserted into the model. Finite elements were oriented to match the three primary orthogonal orientations of manatee rib bone in order to properly align material properties. One analysis was performed for each orientation. Specimens were fitted with cracks equal in length to those measured by Yan (2005) when using the same razor blade crack insertion technique, and elements were oriented to match those of the off-axis specimens. Boundary conditions were applied to closely approximate loading in the test fixture used in the experimental studies. Loads were applied according to the failure loads found during the experimental component of this analysis. Fracture analysis software was used to determine stress intensity factors (SIF or  $K$ ) I, II, and III relative the crack growth direction. Hence  $K_I$  is the opening mode,  $K_{II}$  is the shear mode, and  $K_{III}$  is the tearing mode SIF. Because failure load and critical crack lengths were inserted into the model along with appropriate material properties for the orientations being analyzed,  $K_I$  values reported by the software are actually the mode I fracture toughness values ( $K_{IC}$ ) for manatee rib bone specimens of these particular geometries and orientations. The aim of this study was to determine the fracture toughness of various orientations of manatee rib bone for two different geometries.

Table 4-1. Tensile tests.

Analysis technique	# of specimens per orientation	# of orientations	Total # of specimens used	Output from tests	
MIC (pilot study)	3	3	9	Elastic moduli	Poisson's ratio
MIC + strain gage	3-4	2	7	Elastic moduli at 3 strain rates	Poisson's ratio at 3 strain rates
MIC	13	3	39	Elastic moduli	Poisson's ratio
Off-axis MIC	1-11	3	24	Strains	Critical crack length
V-notch MIC	6-12	6	47	Failure loads	Critical crack length

Table 4-2. Shear tests.

Analysis technique	Number of specimens per orientation	Number of orientations	Total number of specimens used	Output from tests
VIC + shear gage	3	2	6	Shear modulus
VIC	9	1	9	Shear modulus

Table 4-3. Numerical tests.

Specimen model	# of orientations	Output from tests
V-notch	6	Fracture toughness

CHAPTER 5  
TENSILE PROPERTIES OF CORTICAL BONE USING MIRRORED IMAGE  
CORRELATION (MIC)

**Short Summary**

Manatee rib bone was the subject of a relatively new full-field deformation technique called visual image correlation (VIC) which was used to determine the tensile properties of the material. Manatee rib is predominantly primary plexiform bone and consists of very few osteons, no medullary cavity, and is almost completely cortical bone. Tension tests were performed on specimens oriented about three orthogonal directions assumed to be the principal material property directions for manatee rib bone under orthotropic assumptions. Nine bone specimens were analyzed in total (n=3 for each orientation). The specimens were loaded to failure at a rate of 1 mm/min under uniaxial tension. Mirrored image correlation (MIC), derived for this study from VIC, was used to determine full-field deformations simultaneously on the front and back of loaded specimens. Strains were calculated from the slope of the position versus deformation curves on the specimen gage sections, where  $\epsilon_x = dU/dX$  and  $\epsilon_y = dV/dY$ . Elastic moduli and Poisson's ratios were found from the initial slope of the stress-strain curves and the ratios of lateral (Poisson) to longitudinal (normal) strain ( $\nu_{yx} = -\epsilon_x/\epsilon_y$ ), respectively. Poisson's ratios ranged from 0.10 for  $\nu_{21}$  to 0.28 for  $\nu_{12}$  and elastic moduli found for the three orientations were  $E_1 = 14.2 \pm 1.6$  GPa,  $E_2 = 6.8 \pm 3.4$  GPa, and  $E_3 = 7.4 \pm 0.4$  GPa, where subscript 1 denotes the proximodistal orientation, subscript 2 denotes the superficial-deep orientation, and subscript 3 denotes the craniocaudal orientation of the specimens relative to the anatomical directions of the animal.

## Introduction

Cortical bone mechanical testing presents many difficulties due to the nonlinearity, heterogeneity, and anisotropy of the material. Quantifying material response to loading for the purpose of characterizing material properties becomes a challenging task. Nondestructive testing techniques such as ultrasound do not capture the nonlinearity of the material and require prior knowledge of the material density. Traditional mechanical testing procedures make use of strain gages and extensometers to measure material response to loading. These measurement tools average strains or deformations across a specimen gage section, thus they can miss critical factors that influence material response such as stress risers and heterogeneity within a specimen. An alternative, non-contact method of measuring deformations and calculating material properties is presented that overcomes difficulties presented with current techniques.

Visual (or digital) image correlation (VIC) is a non-contact full-field measurement technology, originally developed by researchers at the University of South Carolina (Sutton et al., 1986, 1991; Lichtenberger and Schreier, 2002). It is used to measure geometry, displacements, and plane strains. The underlying principle of the technology is to calculate the displacement field of a test specimen by tracking the deformation of a random speckling pattern applied to the specimen surface. The random pattern is digitally acquired by the cameras before and during loading.

The VIC system then tries to find the region (in the image of the deformed specimen) that maximizes a normalized cross-correlation function corresponding to a small subset of the reference image (taken when no load is applied to the structure) (Sutton et al., 1986). The image space is iteratively swept by the parameters of the cross-correlation function, to transform the coordinates from the original reference frame to coordinates within the deformed image. An originally square subset in the un-deformed image can then be mapped to a subset in the

deformed image, as can be seen in Figure 5-1. As it is unlikely that the deformed coordinates will directly fall onto the sampling grid of the image, accurate grey-value interpolation schemes (Schreier et al., 2000) are implemented to achieve optimal sub-pixel accuracy without bias. This procedure is repeated for a large number of subsets to obtain full-field data.

For two-dimensional plane stress problems, a single camera is sufficient to measure the in-plane displacements, directed orthogonally to the flat speckled surface. For the more general case of three-dimensional problems (where both in-plane and out-of-plane displacements are required over an arbitrarily non-flat surface), two cameras are needed. The acquisition of images is based on a stereo-triangulation technique, as well as the computing of the intersection of two optical rays. Referencing Figure 5-2, the stereo-correlation matches the two 2-D frames taken simultaneously by the two cameras to reconstruct the 3-D geometry, and then uses a tracking technique called temporal matching to follow the speckle deformations (Sutton et al., 1991). The calibration of the two cameras (to account for lens distortion and determine pixel spacing in the model coordinates) is the initial fundamental step, which permits the determination of the corresponding image locations from views in the different cameras. Calibration is done by taking images (with both cameras) of a known fixed grid of black and white dots.

The twin cameras are connected with a PC via an IEEE 1394 (Firewire) cable, and a specialized unit is used to synchronize the camera triggers for instantaneous shots. A standard acquisition board installed in the computer carries out the digitalization of the images, and the image processing is carried out by specialized software (VIC3D v.3.1, Correlated Solutions, Inc., West Columbia, SC). Typical data results that can be obtained from the VIC system consist of the geometry of the surface in discrete  $X$ ,  $Y$ , and  $Z$  coordinates (where the origin is located at the

centroid of the speckled area of interest, and the outward normal points towards the cameras, by default), and the corresponding displacements on the surface ( $U$ ,  $V$ , and  $W$ ).

A new technique was developed for this study that builds on the foundation of VIC in order to accurately capture the response of a specimen to loading. Mirrored image correlation (MIC) is a technique that was developed by the authors in order to provide an accurate account of deformations occurring simultaneously on the front and back of a specimen loaded in tension. The intent of this methodology was to mitigate the effects of bending if the specimens are misaligned in the custom tensile grips. Bending strains are removed by averaging strains found on the front and back of the specimen, leaving only tensile strains for the calculation of material properties. Visual image correlation alone cannot account for strain gradients throughout the thickness of a specimen, thus MIC is superior to VIC when there is a chance of specimen misalignment. Furthermore, MIC reduces error compared to VIC because more data is available and averaged for the analysis. Visual image correlation also has advantages over traditional measurement techniques. For instance, the systemic error of testing systems when using compliance measurement techniques (An and Friedman, 1999) is removed by using VIC, since VIC is a non-contact method of measuring deformations on a specimen surface rather than measuring the relative movement of testing equipment cross-heads, which introduces errors in measurement due to the natural compliance of testing equipment. The analysis technique presented here offers significant improvements towards the assessment of material properties.

Our study aims to describe the role of MIC for measuring full-field deformations during mechanical testing and use of these deformations in the determination of material properties. Manatee rib is ideally suited for mechanical testing due to its large size, its lack of a medullary (hollow) cavity, and its large proportion of cortical bone to trabecular bone. All of these

attributes make it possible to harvest large cortical bone specimens oriented in any direction relative to the rib bone.

The Florida manatee is an endangered species that far too often is killed as a result of collisions with watercraft. Computer simulations that utilize the anisotropic properties of manatee bone tissue can aid in the understanding of how manatee rib bone responds to impact from a watercraft. To this point, material properties are known for only the longitudinal orientation of manatee rib bone and computer simulations cannot accurately depict the true response of manatee rib to loading with this limited input. This study will improve on the ability of computers to predict impact response of watercraft and manatees by identifying material properties for three orthogonal orientations of rib bone under the presumption that manatee rib bone is orthotropic. The present study builds on work completed by other researchers at the University of Florida that aims to reduce watercraft-related injury to this docile marine mammal (Clifton et al., 2003; Clifton, 2005; Yan, 2002, 2005; Yan, 2006a, b, 2007).

The aims of this study are to: 1) determine the elastic modulus for 3-orientations of manatee rib bone using MIC, 2) determine the Poisson's ratio for several orientations of manatee rib bone using MIC, 3) compare MIC results with those from three-point bend and ultrasound studies, 4) characterize the anisotropy of manatee rib bone elastic modulus, 5) evaluate the ability of the custom test fixtures to prevent specimen bending by determining if results significantly differ on the front and back of a specimen, and 6) investigate the linearity of the material for each orientation.

### **Materials and Methods**

Manatee rib bones were obtained under US Fish and Wildlife permit #MA067116-0 issued to the Florida Fish and Wildlife Conservation Commission's (FWC) Marine Mammal Pathology Lab (MMPL). Use of the tissue was governed by University of Florida Institutional Animal Care

and Use Committee (IACUC) protocol #E407. One center rib (#9 of 17-19 ribs) was selected for this study from a single adult male manatee (Figure 5-3). The manatee rib was stored with flesh intact to preserve material properties (An and Draughn, 2000) at -20° Celsius. The middle third of the selected rib was used for testing, since Yan (2002) found that the fracture properties of manatee rib bone vary from the middle of each rib to the ends of the bone and it is assumed that material properties (in addition to fracture properties) vary as a function of position in the rib.

The specimens were rough-cut with a wet band saw: Close attention was paid to the orientation in which the specimens were harvested. Specimens were milled to their final dimensions (total length = 38 mm, width at grip = 12.7 mm, gage length = 19 mm, gage width = 6.4 mm, radius at gage section = 3.2 mm, and a square cross-section) under constant irrigation with water to prevent over-heating. The specimens were allowed to air dry at room temperature for 2 weeks prior to testing to provide a dry surface for application of the speckle pattern used during the VIC analysis. Specimens were spray painted white and dusted with black spray paint to generate the random speckle pattern used by the VIC stereo system during image correlation. During testing, specimens were fixed in a uniaxial loading machine (MTI 30K, Measurement Technology, Inc., Roswell, GA) in custom holders that were designed and fabricated for this study in order to reduce shadows cast on the specimen by halogen lights used to improve image quality during testing. A flat mirror was placed as close to the specimens as possible while still allowing for both the front and back of the specimens to be in view of the VIC cameras, since the focal length of the camera lenses (Schneider-Kreuznach Cinegon CM120, Bad Kreuznach, Germany) was limited. Optimal performance of the VIC stereo system was obtained when the cameras were placed ~13 mm behind the specimens with the cameras (Retiga 1300, Quantitative Imaging Corporation, Burnaby, British Columbia, Canada) arranged to form a near equilateral

triangle with the specimens (Figure 5-4). The cameras were calibrated with a dot matrix calibration grid generated using custom software provided by Correlated Solutions, Inc. and image correlation software (VIC3D v3.1, Correlated Solutions, Inc., West Columbia, SC). Specimens were loaded to failure at a rate of 1 mm/min. Load data was monitored using a 1000-lb load cell (Interface SM-1000-38, Scottsdale, AZ) accurate to 20 grams, received and amplified by a terminal block and signal amplifier (SCXI-1321 and SCXI-1121, National Instruments Corporation, Austin, TX), and logged using a custom Labview program (Labview v.7.0, National Instruments Corporation, Austin, TX). Correlation analyses were performed on the gage sections of loaded specimen images (Figure 5-5) using VIC3D v3.1. Output from the VIC analyses included position, deformation, and velocity for each data point on the specimen gage sections. Output files were exported from VIC3D and Labview and input into a custom Mathcad program (Mathcad v.12.1, Mathsoft Engineering and Education, Inc., Needham, MA) for further data reduction and analysis. Strains were calculated for each load step from the slope of the position versus deformation curves across the specimen gage sections, where  $\epsilon_x = dU/dX$  (Poisson strain) and  $\epsilon_y = dV/dY$  (normal strain) (Figure 5-6). Strains calculated for each load step were averaged over the linear range of the stress-strain curves for each specimen tested. The strains on the front and back of the specimen were averaged to remove bending effects on tensile property calculations. Poisson's ratio was taken as the negative ratio of Poisson strain to normal strain ( $\epsilon_{xy} = -\epsilon_y/\epsilon_x$ ) (Figure 5-7), while elastic modulus was calculated as the initial slope of the stress-strain curve (Figure 5-8). The linearity of the stress-strain curves was assessed by visual inspection.

The analysis required several operations to be performed on the data before Poisson's ratios and elastic moduli could be reported: 1) Poorly-correlated data points (as determined by

VIC3D software) ( $correlation \leq 0$ ) were removed from the dataset; 2) Data associated with negative or invalid Poisson's ratios ( $0 > \nu_{xy} > 0.5$ ) were removed from the analysis; 3) Data associated with deformation rates sufficiently different than the prescribed rate ( $0.5 \text{ mm/min} < \text{velocity} < 1.5 \text{ mm/min}$ ) were removed, since these points may be indicative of faulty data; 4) Several data points in the lower loading range were filtered out of the analysis because these data points did not meet minimum strain level requirements (strains less than  $500 \mu\epsilon$  are considered to be too small for the VIC system to accurately detect); and 5) Data points in the non-linear range of the stress-strain curve were removed from the elastic tensile property calculations.

The anisotropic elastic constants of manatee bone were analyzed using VIC along three directions assumed to be principal material axes of manatee rib (Figure 5-9). Three specimens were prepared in each of the three orientations selected for this analysis (labeled A, B, and C, respectively based on the order they were tested). Miller indices (Murray, 1993) were used in addition to anatomical labeling of material orientations to accommodate those readers whom are more familiar with labeling of crystalline structures and to keep specimen labels concise. The Miller indices represent the loading axis of the specimen. Specimens labeled as [100] were oriented (loaded) in the proximodistal direction. Superficial-deep specimens are labeled as [010]. The craniocaudal specimens are labeled as [001].

### **Statistics**

One-way ANOVA was performed on the means of all specimen orientations to determine if any modulus means were significantly different between the tested orientations. Independent group t-tests were performed on modulus means for each possible pair of specimen orientations to determine which means significantly differed. Not enough specimens were assessed to perform ANOVA or group t-tests on Poisson's ratio. Matched pairs t-tests were performed on

results from the front and back of specimens for a given orientation to determine if the effect of bending was significant on tensile properties for any orientation. Paired t-tests were also performed on elastic modulus and Poisson's ratio where all values were used regardless of orientation to see if bending had any effect on elastic modulus or Poisson's ratio as a whole. The null hypothesis for all tests was that no statistical difference existed between the variables. Significance was assumed if  $p < 0.05$ . Statistical analyses were performed using Statistics Calculator v.3.0 (StatPac, Inc., Bloomington, MN).

## Results

Results from each of the 9 specimens are provided in Tables 5-1 and 5-2 and Figures 5-10 to 5-12. Mean values and standard deviations (*SD*) are presented for elastic moduli along with the number of specimens used to calculate these values (*n*). Experimental values of several material properties of manatee rib bone are provided in Table 5-3 for comparison to values obtained during this study.

The proximodistal [100] orientation represents the longitudinal axis of the manatee rib bone. The strength for this orientation is much greater than for the other two orientations (Figure 5-10). The mean elastic modulus and standard deviation for the 3 proximodistal specimens was  $14.2 \pm 1.6$  GPa.

The superficial-deep [010] orientation represents the transverse plane minor-axis. Failure strength was the most uniform between specimens for this orientation. The strength was slightly greater than that for the craniocaudal orientation, but much less than for the proximodistal orientation. Failure strain was quite variable for this orientation. The stress-strain curve was more nonlinear for this orientation than for the other two orientations (Figure 5-11). The mean elastic modulus and standard deviation for the 3 superficial-deep specimens was  $6.8 \pm 3.4$  GPa.

The craniocaudal [001] orientation represents the major-axis in the transverse plane of the manatee rib bone. The mean failure strain for this orientation is lower than for the other orientations. The strength is nearly identical to that of the superficial-deep specimen orientation, but lesser than the proximodistal orientation. The slope of the craniocaudal stress-strain curve is (on average) more linear than the slope for the other two orientations (Figure 5-12). The mean elastic modulus and standard deviation for the 3 craniocaudal specimens was  $7.4 \pm 0.4$  GPa.

### **Statistical Results**

A one-way ANOVA test was performed on the tensile property means of three specimen orientations to determine if the difference between any of the orientations was significant. The  $p$ -value ( $<0.001$  for both modulus and Poisson's ratio) was significant ( $p < 0.05$ ). Therefore, the null hypothesis is rejected and it is concluded that at least one mean was significantly different from the others for both modulus and Poisson's ratio results.

For the paired t-tests performed on elastic moduli for three orientations, the t-statistic was significant at the 0.05 critical alpha level ( $t(4)=3.442$  with  $p=0.0262$ ) for  $E_1$  and  $E_2$ . Therefore, the null hypothesis is rejected and it is concluded that there is a significant difference between elastic moduli  $E_1$  and  $E_2$ . The t-statistic was not significant ( $t(4)=0.226$  with  $p=0.8322$ ) for  $E_2$  and  $E_3$ . Therefore, the null hypothesis is accepted and it is concluded that there is no significant difference between elastic moduli  $E_2$  and  $E_3$ . The t-statistic was significant ( $t(4)=3.097$  with  $p=0.0363$ ) for  $E_1$  and  $E_3$ . Therefore, the null hypothesis is rejected and it is concluded that there is a significant difference between elastic moduli  $E_1$  and  $E_3$ .

In comparing tensile properties on the front and back of the specimens using matched pairs t-tests, the null hypothesis was accepted for all tests ( $p > 0.05$ ) and it is concluded that no significant difference exists between values found on the front and back of the specimens used in this study.

## Discussion

Results from this study agree well with those from Clifton (2005) for a 3-point bend specimen taken from a center rib of the same manatee used in this study ( $14.3 \pm 2.0$  GPa for the [100] direction here compared to 15.7 GPa in the Clifton study). Poisson's ratios from various directions in this study ranged from  $\nu=0.10$  to 0.28, and are on the same order as those from Yan's ultrasound study (2002) ( $\nu=0.25$ ), although the results are not directly comparable since Poisson's ratio from Yan's study was calculated using isotropic assumptions ( $\nu = \frac{E}{2G} - 1$ ).

Results from this study provide an idea of the anisotropic nature of manatee rib bone elastic modulus, although more specimens should be assessed prior to drawing any final conclusions due to the relatively large coefficient of variation ( $CV=SD/\mu$ ) for elastic modulus. In this study, elastic modulus from one of the three orientations differed significantly from the others while the other two did not significantly differ from one another, implying that manatee rib bone elastic modulus is transversely isotropic (i.e., there is one plane of material symmetry). Although the anisotropic nature of manatee rib bone has been found for a limited number of specimens, a complete characterization of manatee rib bone material properties would require the knowledge of the material's shear properties in addition to knowing the elastic moduli and Poisson's ratios. It is recommended that additional tensile tests as well as shear tests be conducted in order to fully characterize the anisotropy of manatee rib bone material properties.

Manatee rib bone is significantly more compliant in the transverse plane than in the longitudinal plane ( $E_1 \approx 2 \times E_2$  and  $E_3$ ). It is hypothesized that measures of fracture toughness will follow suit with one orientation being significantly tougher than the other two orientations. Thus previous analyses assessing manatee rib bone fracture toughness in the low-compliance direction (Clifton et al., 2003, Clifton, 2005; Yan et al., 2006a, b, 2007) may over-estimate the minimum

toughness of manatee bone. The results presented here may therefore imply that manatee rib bone is far more fragile than originally thought. It has already been shown that manatee rib bone is less tough than other animal bones consisting of primary plexiform bone (Yan et al., 2006b).

The lack of significant difference between tensile properties calculated on the front and back of a specimen show that MIC is not required to obtain material properties (i.e., VIC may be good enough given that there is no bending in the experimental setup). It is cautioned that any experimental set-up used for assessing tensile properties other than the one used here should also be analyzed for bending effects if reporting VIC results for only one specimen face. Mirrored image correlation reduces error compared to VIC by removing the unwanted effects of bending induced by a tensile test fixture or misaligned specimen and by allowing for more data points to be averaged over the specimen gage sections.

An and Draughn (2000) assume that although bone is a viscoelastic material, it only exhibits a slight degree of viscoelasticity and can therefore be treated as a linear-elastic material. This assumption was assessed by visual inspection of the experimentally determined stress versus strain curves found from the tensile tests. It was found that significant nonlinearity existed for all orientations tested here (Figures 5-10 to 5-12). The cause for this nonlinear behavior remains unknown, since this study did not investigate whether the nonlinearity was due to microcracking, other forms of plasticity, or viscoelasticity. Testing of the cyclic behavior and strain-rate dependent behavior of manatee rib bone can shed more light on this subject. Also, X-ray diffraction, fractography, or other imaging techniques can be used to assess the existence of microcracks in the specimens pre- and post-testing.

### **Conclusions**

Elastic moduli and Poisson's ratios were found for three orientations of manatee rib bone. Elastic modulus was found to be transversely isotropic. To the authors' knowledge, this is the

first study to use MIC in the determination of material properties. The technique is superior to VIC if unwanted specimen bending is present. Mirrored image correlation is a viable alternative to 3-point bending for the determination of cortical bone modulus.

Several benefits exist from the use of VIC over other measures of deformation and strain (e.g., compliance-based techniques, strain gages, and extensometers), including: 1) Deformations are measured on the specimen surface(s) and thus do not reflect machine compliance in the test rig; 2) Material heterogeneity can be accounted for by looking for changes in slope of the position versus deformation curves (indicating differences in strain magnitude across the gage section), while most other techniques average strains over the entire specimen gage section; 3) Visual image correlation measurements are valid to 500% strain, while strain gages usually have a much lower top-out limit, thus VIC may be a better tool for capturing failure strain of a material than strain gages; 4) Localized strain (around notches or material imperfections) can be assessed using VIC, while they cannot with strain gages or extensometers.

The drawbacks of VIC include: 1) The minimum strain magnitude captured by the VIC system is limited by image correlation algorithms (currently, strains are not considered accurate below 500  $\mu\epsilon$ ); 2) Set-up time can be significant when considering the time to position and focus the cameras and calibrate the stereo system; although once the set-up is in place, testing can take place very rapidly.

Table 5-1. Elastic moduli from MIC analysis. Mean values are presented  $\pm$  standard deviations along with the number of specimens used to compute the mean values ( $n$ ).

Elastic modulus (GPa)			
	Proximodistal [100] ( $E_1$ )	Superficial-Deep [010] ( $E_2$ )	Craniocaudal [001] ( $E_3$ )
Specimen A	16.0	9.8	7.8
Specimen B	13.9	7.6	7.3
Specimen C	12.8	3.1	7.0
Mean	14.2 $\pm$ 1.6 ( $n=3$ )	6.8 $\pm$ 3.4 ( $n=3$ )	7.4 $\pm$ 0.4 ( $n=3$ )

Table 5-2. Poisson's ratios from MIC analysis. Index 1 denotes the [100] direction, index 2 denotes the [010] direction, and index 3 denotes the [001] direction.

Poisson's ratio			
	Proximodistal [100] ( $\nu_{1x}$ )	Superficial-Deep [010] ( $\nu_{2x}$ )	Craniocaudal [001] ( $\nu_{3x}$ )
Specimen A	$\nu_{13}=0.28$	$\nu_{21}=0.21$	$\nu_{31}=0.14$
Specimen B	$\nu_{12}=0.25$	$\nu_{21}=0.29$	$\nu_{32}=0.24$
Specimen C	$\nu_{13}=0.29$	$\nu_{23}=0.10$	$\nu_{32}=0.23$

Table 5-3. Summary of known manatee rib material properties.

Investigators	Testing method	Bone source	Load or wave direction	Elastic modulus (GPa)	Poisson's ratio	Shear modulus (GPa)
Yan (2002)	Ultrasonic	Manatee rib	Transverse	18.13 $\pm$ 1.77	0.253 $\pm$ 0.021	7.24 $\pm$ 0.711
Clifton (2005)	3-point bend	Manatee rib	Transverse	$E_1=4$ to 18	-	-
Clifton (2005)	3-point bend	MSW0253*	Transverse	$E_1=15.7$	-	-

\*MSW0253 is the ID for the same manatee as was used in the present study

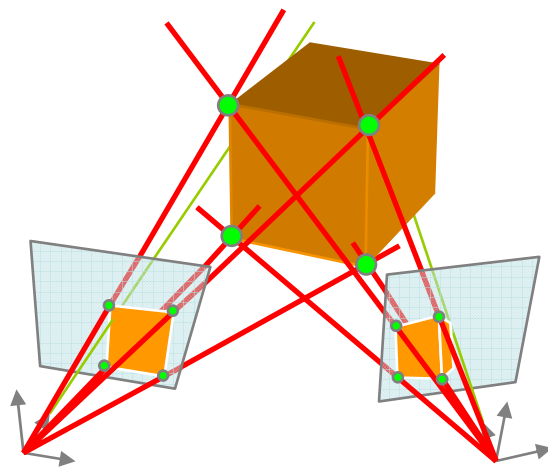


Figure 5-1. Three-dimensional surface as seen by two imaging sensors (courtesy of Correlated Solutions, Inc, West Columbia, SC).

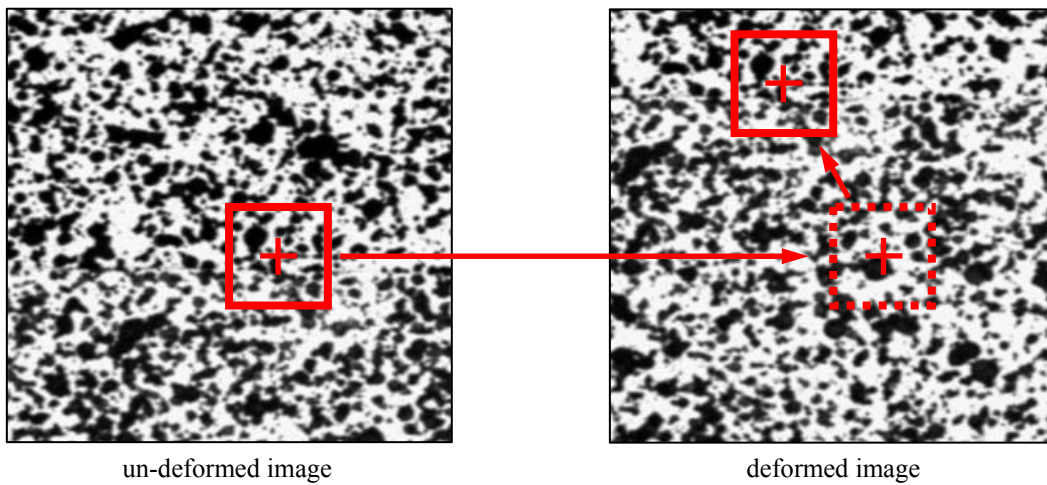


Figure 5-2. Movement of a sample square subset used for cross-correlation function estimation (courtesy of Correlated Solutions, Inc., West Columbia, SC).

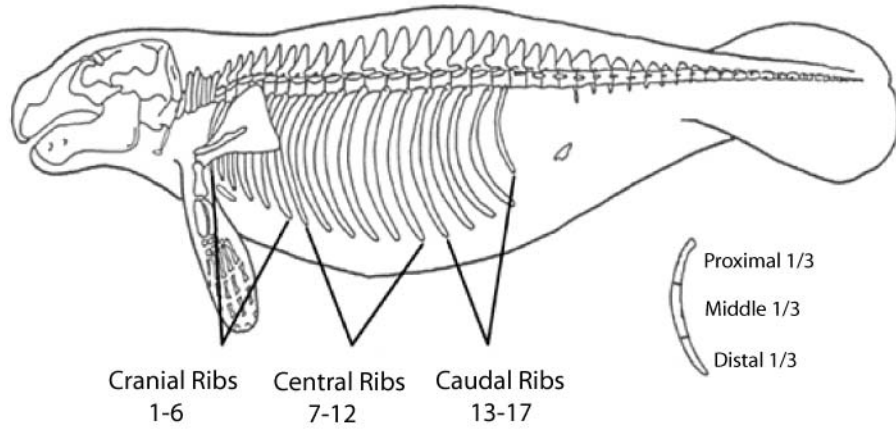


Figure 5-3. Manatee skeleton. Modified with permission from Yan, J., 2002. Biomechanical properties of manatee rib bone and analytical study using finite element analysis. M.S. Thesis, University of Florida, Gainesville, Figure 3-2, p. 19.

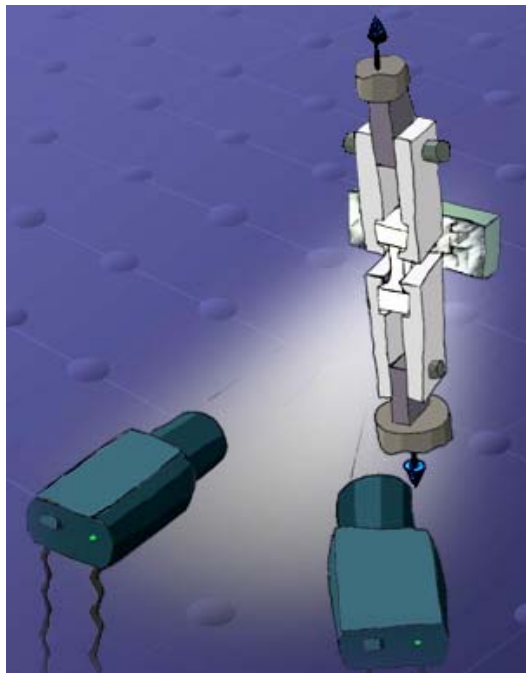


Figure 5-4. Stereographic set-up used in the MIC analysis.

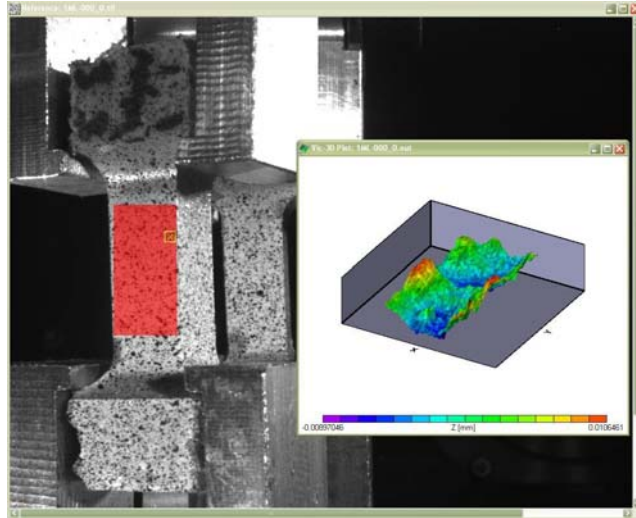


Figure 5-5. Example image and target region used by VIC3D to generate a dataset and the associated image surface plot created by VIC3D showing the exaggerated XYZ position data.

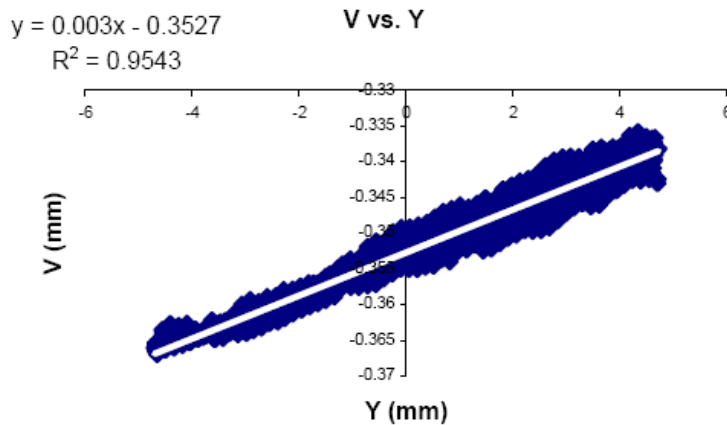


Figure 5-6. Typical  $dV/dY$  curve showing all data points on the gage section of a manatee rib bone specimen. The normal strain (slope of the  $V$  vs.  $Y$  curve) is  $3000 \mu\epsilon$  for this particular load step. The white line is the linear trend line used to fit the thousands of data points depicted in the plot.

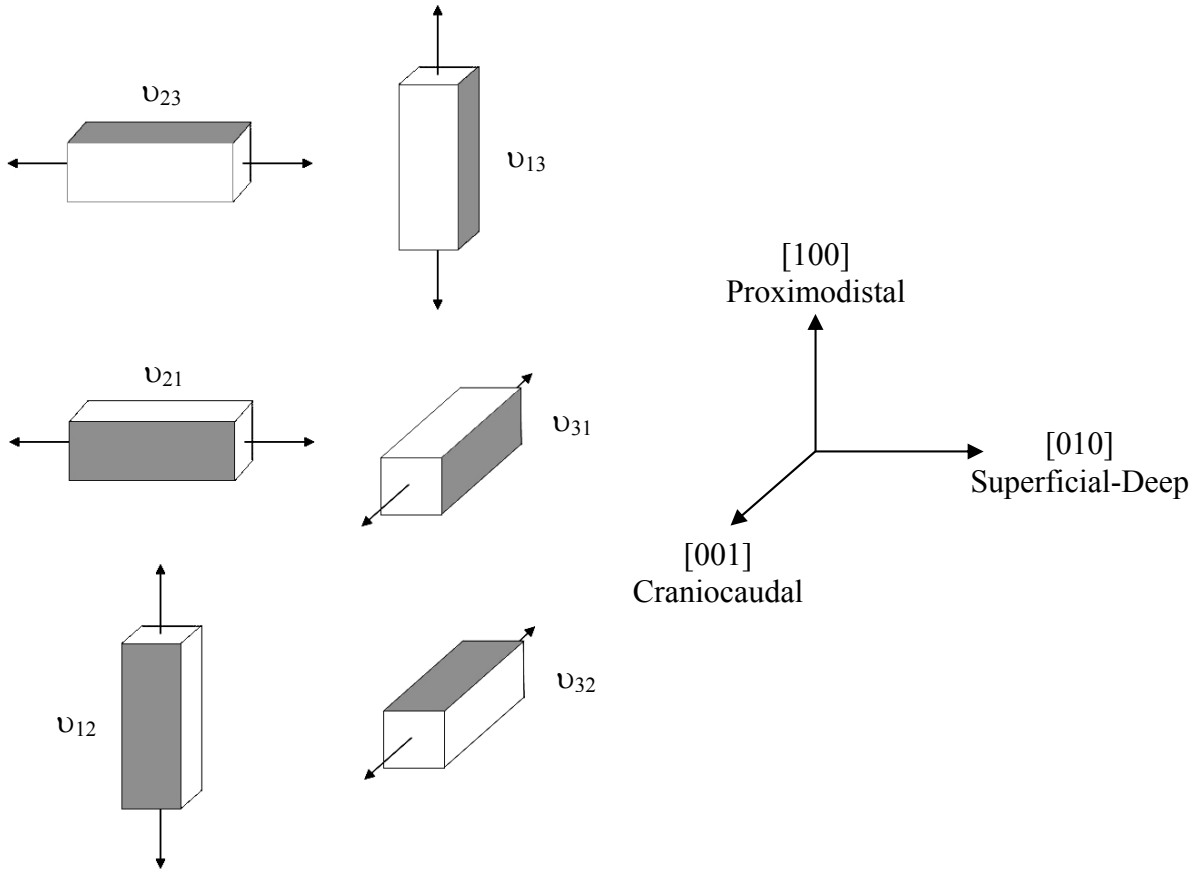


Figure 5-7. Nomenclature used for the Poisson's ratio analysis. Shaded faces represent the faces on which each respective Poisson's ratio was evaluated.

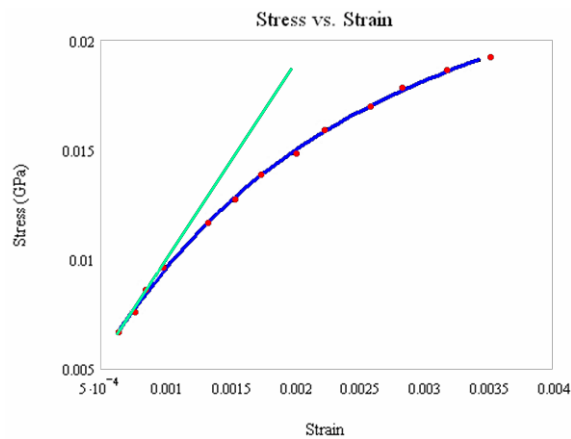


Figure 5-8. Stress-strain curve for a [010] specimen. The initial slope of the stress-strain curve (depicted in light green) is the elastic modulus for this specimen. The red dots represent the experimental data points obtained from the MIC analysis for each load step.

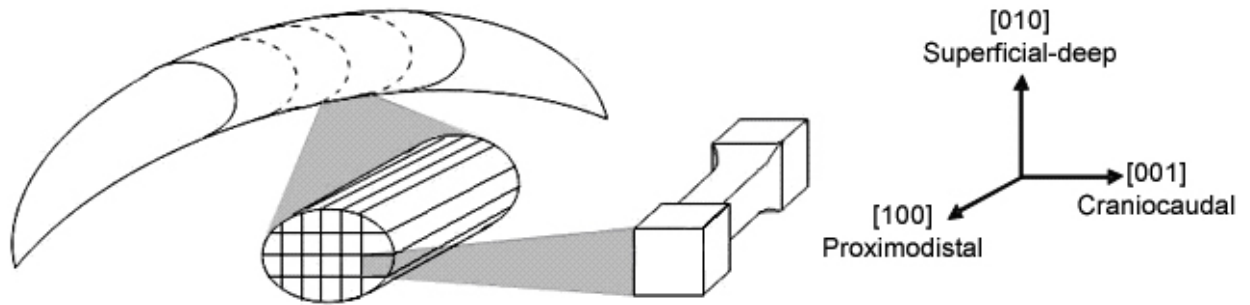


Figure 5-9. Schematic of Proximodistal [100] specimens prepared from the middle 1/3<sup>rd</sup> of an adult manatee rib bone.

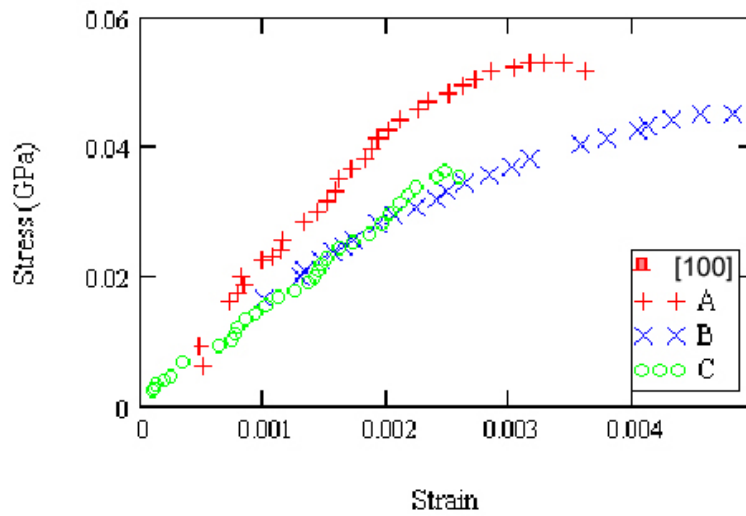


Figure 5-10. Proximodistal [100] stress-strain curve for three dry manatee rib bone specimens (A, B, and C) loaded to failure.

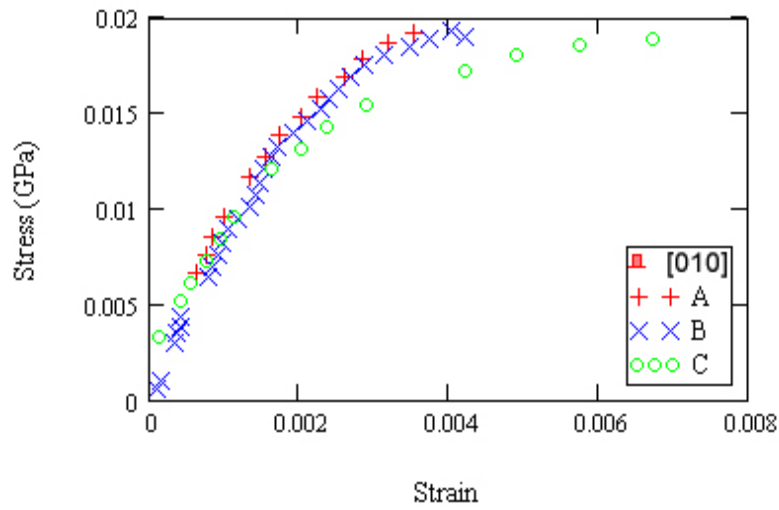


Figure 5-11. Superficial-Deep [010] stress-strain curve for three dry manatee rib bone specimens (A, B, and C) loaded to failure.

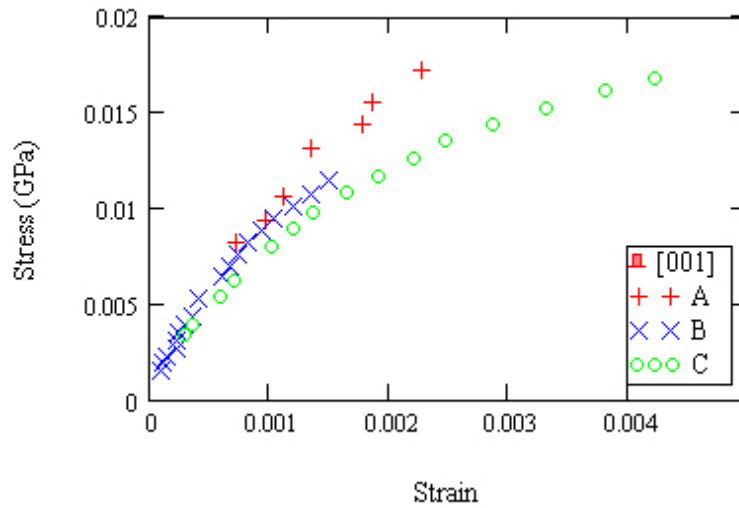


Figure 5-12. Craniocaudal [001] stress-strain curve for three dry manatee rib bone specimens (A, B, and C) loaded to failure.

## CHAPTER 6 ANISOTROPIC ELASTIC TENSILE PROPERTIES

### Short Summary

This chapter conveys the first study to analyze the nature of the anisotropy of manatee rib bone tensile properties. Three elastic moduli and three Poisson's ratios were determined using a non-contact, full-field deformation analysis technique called visual image correlation (VIC). Previously, tensile data existed for only one orientation of manatee rib bone. A complete set of anisotropic material data is required in order to develop constitutive models that are capable of predicting the material's response to loading. This chapter is the first part of a three part series of studies aimed at characterizing manatee rib bone material properties. The specific aim of Part 1 (Chapter 6) is to determine the tensile properties of the material, while Part 2 (Chapter 7) will identify the shear properties of manatee rib bone. Parts 1 and 2 will provide sufficient information for the completion of the anisotropic elastic constants matrix under the assumption of material orthotropy. Part 3 (Chapter 8) will verify the orthotropic assumption by means of comparing experimental and predicted strains in off-axis specimens using the constitutive model built for the material in Parts 1 and 2.

Visual image correlation is an ideal tool for assessing the strain field in heterogeneous materials such as bone, since the technique is capable of discerning localized effects within the gage section. The output from the VIC analysis is the three-dimensional position and deformation data in the gage region of each specimen. The derivative of the deformation with respect to the position is taken as the strain in each specimen ( $\varepsilon_x = dU/dX$  and  $\varepsilon_y = dV/dY$ ). Poisson's ratio is taken as the negative of the ratio between Poisson and normal strain ( $\nu_{xy} = -\varepsilon_x/\varepsilon_y$ ). Elastic modulus is taken as the initial slope of the stress-strain curve ( $E = \sigma/\varepsilon_y$ ). Elastic modulus was found to be  $16.9 \pm 1.5$  GPa in the proximodistal (longitudinal) direction of the bone,

8.4±1.2 GPa in the superficial-deep (in-plane transverse) direction, and 5.9±2.2 GPa in the craniocaudal (in-plane transverse) direction. Major Poisson's ratios were  $\nu_{12}=0.27\pm0.04$ ,  $\nu_{13}=0.25\pm0.04$ , and  $\nu_{23}=0.25\pm0.04$ , while the minor Poisson's ratios were  $\nu_{21}=0.16\pm0.06$ ,  $\nu_{31}=0.15\pm0.07$ , and  $\nu_{32}=0.28\pm0.08$ . The significant difference between elastic moduli in three orthogonal directions implies that the material is orthotropic, although material models that can prove this assumption still require input of shear modulus data.

### **Introduction**

To date, no experiments have demonstrated the anisotropic nature of manatee rib bone. Preliminary models of the material have been limited to isotropic assumptions due to the limited amount of material data available (Yan, 2002). Without the proper material property input (e.g., treating an anisotropic material as isotropic), constitutive models for anisotropic materials cannot be used to accurately predict material response to loading (Arakere and Swanson, 2002; Arakere et al., 2005; Ranjan and Arakere, 2007). It is important to understand the response of this brittle tissue to mechanical loading in order to promote efforts to reduce the high casualty rate in manatees resulting from collisions with watercraft: Twenty-five percent of all manatees are killed by collision with watercraft with more than half of these deaths attributed to rib bone fracture (Clifton, 2005). Crack propagation in manatee rib bone is facilitated by a high mineral density and a shortage of osteons that bridge and blunt cracks and assist in the healing process of bone in most mammals. The implication of these features is that manatee rib fractures are often fatal. This study aims to provide the initial data required to complete the orthotropic elastic constants matrix for manatee rib bone so that predictive modeling of bone fracture will be possible in the future.

Testing of cortical bone material properties presents several challenges due to material hierarchy, nonlinearity, anisotropy, and limitations in specimen thickness. Several levels of hierarchy have been identified for bone, each containing a unique set of properties and material characteristics (Weiner and Wagner, 1998; Rho et al., 1998). Tissue level properties were analyzed in the present study for the identification of direction dependent properties to help achieve the end goal of developing models of whole bone. In many mammals, cortical bone would be too thin at most anatomical sites in order to assess tissue level properties in the three orthogonal directions required for orthotropic materials. However, manatee rib bone is unique in that it possesses no marrow cavity and it is predominantly cortical bone, thus it is quite conducive towards obtaining material properties in any direction. The analysis technique used to measure deformations in the tensile specimens is called visual image correlation (VIC). Visual image correlation is a full-field deformation analysis technique capable of providing three-dimensional position and deformation information for the surface of a loaded specimen using stereoscopic imagery (Sutton et al., 1986; 1991; Schreier et al., 2000; Lichtenberger and Schreier, 2002). The full-field deformation analysis is capable of identifying localized effects in a specimen that could be indicative of material or structural inhomogeneities within the gage section that would go un-noticed using other deformation or strain analysis techniques (i.e., strain gages and extensometers average strain and deformation data, respectively, across the gage section of a material and localized effects cannot be identified). The technique is considered accurate from  $500 \mu\epsilon$  to 500% strain, thus it lends itself wonderfully towards testing biological materials undergoing large amounts of strain. Furthermore, commercial modules are available that allow for VIC to be performed at high speeds, thus impact and vibration testing is possible using the technique. Zhang et al. (2007) used a two-dimensional form of VIC (using a single

camera) to investigate the tensile properties of bovine hoof horn. The technique has also been used to measure microstructural strains in cortical bone (Nicoletta et al., 2001). To the authors' knowledge, this is the first study of the anisotropic material properties of cortical bone using VIC.

Bone is generally considered to be a transversely isotropic (Yoon et al., 1976; Gotzen et al., 2003; Dong and Guo, 2004) or orthotropic material (Ashman et al., 1984; Hoffmeister et al., 2000). Material property data for one specimen orientation is not sufficient for modeling the constitutive behavior of an anisotropic material. Therefore, this study will analyze manatee rib (cortical) bone tensile specimens along three orthogonal directions in order to assess the directional dependence (anisotropy) of the material. The nomenclature used to describe the directional dependence of the material is as follows: the proximodistal direction of the manatee was designated as the 1-direction (i.e., the longitudinal direction of the rib bone), superficial-deep as 2 (i.e., the in-plane transverse direction of the rib bone), and craniocaudal as 3 (i.e., the out-of-plane transverse direction of the rib). The numbers appear as subscripts in the material properties analysis to describe the direction(s) of measured strain. For example,  $E_1$  is the elastic modulus in the 1-direction, and  $\nu_{12}$  is the ratio of Poisson strain in the 2-direction to normal strain in the 1-direction.

## **Methods**

Manatee rib bones were obtained under US Fish and Wildlife permit #MA067116-0 issued to the Florida Fish and Wildlife Conservation Commission's (FWC) Marine Mammal Pathology Lab (MMPL). Use of the tissue was governed by University of Florida Institutional Animal Care and Use Committee (IACUC) protocol #E407. Ribs from the center third of several adult manatees (#s 9-11 of 17-19 ribs) were selected for this study (Figure 6-1), and specimens

were prepared from the middle third of the ribs since their properties were previously shown to vary as a function of anatomic position (Yan, 2006a). The manatee rib was stored with flesh intact to preserve material properties (An and Draughn, 2000) at -20° Celsius. Thirteen specimens were prepared for each orientation (proximodistal, superficial-deep, and craniocaudal). Specimens were rough-cut with a wet band saw, with close attention being paid to the orientation in which the specimens were harvested. Specimens were milled to their final dimensions (total length = 38 mm, width at grip = 12.7 mm, gage length = 19 mm, gage width = 6.4 mm, radius at gage section = 3.2 mm, and a square cross-section) under constant irrigation with water to prevent over-heating. Specimens were wrapped in gauze and soaked in saline solution while being stored in a refrigerator for up to a week prior to testing. Specimens were wiped dry, spray painted white and dusted with black spray paint to generate a random speckle pattern used by the VIC stereo system during image correlation. Specimens were then re-hydrated in saline solution for 3 hours before testing at room temperature. During testing, specimens were fixed in a uniaxial loading machine (MTI 30K, Measurement Technology, Inc., Roswell, GA) in custom holders that were designed and fabricated for this study in order to reduce shadows cast on the specimen by halogen lights used to improve image quality during testing. Optimal performance of the VIC stereo system was obtained when the cameras were placed ~13 mm behind the specimens with the cameras (Retiga 1300, Quantitative Imaging Corporation, Burnaby, British Columbia, Canada) arranged to form a near equilateral triangle with the specimens. The cameras were calibrated with a dot matrix calibration grid generated using custom software provided by Correlated Solutions, Inc. and image correlation software (VIC-3D Digital Image Correlation v2006.0.0, Correlated Solutions, Inc., West Columbia, SC). Specimens oriented in the medial-lateral direction were loaded to 670 N, those oriented in the

anterior-posterior direction were loaded to 1100 N, and specimens oriented in the cranial-caudal direction were loaded to 670 N at a rate of 1 mm/min (~5%/min). Loads were selected for each orientation based on results from a pilot study in which dry bone specimens of identical dimensions were loaded to failure at the same load rate. The maximum load in this study corresponds with the yield load for each orientation tested in the pilot study. Load data was monitored using a 1000-lb load cell (Interface SM-1000-38, Scottsdale, AZ), received and amplified by a terminal block and signal amplifier (SCXI-1321 and SCXI-1121, National Instruments Corporation, Austin, TX), and logged using a custom Labview program (Labview v.7.0, National Instruments Corporation, Austin, TX). Correlation analyses were performed on the gage sections of loaded specimen images (Figure 6-2) using VIC3D software. Output from the VIC analyses included position, deformation, and velocity for each data point on the specimen gage sections. Output files were exported from VIC3D and Labview and input into a custom Mathcad program (Mathcad v.12.1, Mathsoft Engineering and Education, Inc., Needham, MA) for further data reduction and analysis. Strains were calculated for each load step from the slope of the position versus deformation curves across the specimen gage sections, where  $\varepsilon_x = dU/dX$  (Poisson strain) and  $\varepsilon_y = dV/dY$  (normal strain) (Figure 6-3). Strains calculated for each load step were averaged over the linear range of the stress-strain curves for each specimen tested. Poisson's ratio was taken as negative the ratio of Poisson strain to normal strain ( $\nu_{yx} = -\varepsilon_x/\varepsilon_y$ ). Major Poisson's ratios are defined as  $\nu_{12}$ ,  $\nu_{13}$ , and  $\nu_{23}$ , while minor Poisson's ratios are defined as  $\nu_{21}$ ,  $\nu_{31}$ , and  $\nu_{32}$ . Differentiation of major and minor Poisson's ratios is necessary to support conventions used in the literature. Elastic modulus was calculated as the initial slope of the stress-strain curve (Figure 6-4). Anisotropic ratios ( $r_{xy}$ ) were taken as the ratio of the modulus in the  $x$ -direction to that in the  $y$ -direction.

One-way ANOVA was used to determine if elastic modulus or Poisson's ratio means varied significantly between any of the orientations. Independent group t-tests were performed on all possible pairs of specimen orientations to determine which means significantly differed, if any. Significance was taken if  $p < 0.05$ . Statistical analyses were performed using Statistics Calculator v.3.0 (StatPac, Inc., Bloomington, MN).

### Results

Table 6-1 shows the elastic modulus and Poisson's ratio of manatee rib bone as a function of orientation. One-way ANOVA revealed that at least one mean was significantly different from the others for modulus ( $p < 0.001$ ) and minor Poisson's ratio ( $p = 0.015$ ), while the major Poisson's ratios did not vary significantly from one another ( $p = 0.360$ ). Independent group t-test results demonstrated that elastic modulus varied significantly between all combinations of orientations ( $p < 0.001$  for  $E_1$  and  $E_2$ ,  $p < 0.001$  for  $E_1$  and  $E_3$ , and  $p = 0.0014$  for  $E_2$  and  $E_3$ ). Independent group t-test results for minors Poisson's ratios were:  $\nu_{21}$  and  $\nu_{31}$  did not significantly vary ( $p = 0.699$ ),  $\nu_{21}$  and  $\nu_{32}$  varied significantly ( $p = 0.021$ ), and  $\nu_{31}$  and  $\nu_{32}$  varied significantly ( $p = 0.014$ ). The anisotropic ratio was largest between  $E_1$  and  $E_3$  ( $r_{13} = 2.9$ ) and was smallest between  $E_2$  and  $E_3$  ( $r_{23} = 1.4$ ).

### Discussion

Results from this study agree with those from Clifton (2005) for a 3-point bend specimen from a center rib of the same manatee used in this study ( $E_I = 16.9 \pm 1.5$  GPa in this study compared to 15.7 and 16.4 GPa in the Clifton study (Table 6-2)). Poisson's ratios from this study are on the same order as those from Yan's ultrasound study (2002) (Table 6-2), although the results are not directly comparable since Poisson's ratio from Yan's study was calculated using isotropic assumptions ( $\nu = \frac{E}{2G} - 1$ ).

This study provides sufficient information to suggest the anisotropic nature of manatee rib bone. In this study, each of the three elastic moduli differed significantly from one another, implying that manatee rib bone elastic modulus is orthotropic. Although the anisotropic nature of manatee rib bone elastic modulus has been found, a complete characterization of manatee rib bone material properties would require the knowledge of the material's shear properties in addition to the tensile properties reported in this study. Part 2 of this series will assess the shear properties of manatee rib bone in order to provide sufficient information to fully characterize the anisotropy of manatee rib bone material properties (Part 3). Part 3 will use the major Poisson's ratios reported in this chapter in order to comply with the most commonly used convention for this variable. It should be noted that the minor Poisson's ratio can be calculated from the major Poisson's ratio and the elastic moduli according to the following relation:  $\nu_{yx} = \nu_{xy} \left( \frac{E_y}{E_x} \right)$  for  $x \neq y = 1, 2, 3$ .

Manatee rib bone is significantly more compliant in the transverse plane than in the longitudinal plane ( $E_1 \approx 2 \times E_2$  and  $\approx 3 \times E_3$ ). It is hypothesized that measures of toughness will follow suit with one orientation being significantly tougher than the other two orientations, thus previous analyses assessing manatee rib bone fracture toughness in the low-compliance direction (Clifton et al., 2003; Clifton, 2005; Yan et al., 2006a, b, and 2007) may over-estimate the toughness for the minimum toughness orientation of manatee bone. It has already been shown that manatee rib bone is less tough than other mammalian bone (Yan et al. 2006a). The results presented here imply that manatee rib bone may be far less tough than originally thought. Aside from being less tough than other bone, manatee rib bone is also unique in that the anisotropic ratio ( $r_{12}=2.9$ ) is much higher than what is found in plexiform bone of other animals ( $r_{LT}=1.18$ -

1.47 (Weiner and Wagner, 1998), where  $L$  is the longitudinal direction of bone and  $T$  is the transverse direction).

Manatee rib is predominantly primary plexiform bone and has very few pores or osteons. Plexiform bone is a rapidly forming bone with a brick-like structure that is generally found in large mammals (Martin and Burr, 1989). The organization of the microstructure is likely responsible for the high anisotropic ratio in this material. Gotzen et al. (2003) used histology to identify the organization of microstructural features around nutrient foramen, which are naturally forming holes in bone. They used the data they collected to build a finite element model to understand strain and modulus distribution in proximity to the foramen. A similar technique could be used to identify the effect of microstructural organization on the anisotropic ratios in manatee rib bone. However, the scope of this study was to quantify manatee rib tensile property anisotropy at the tissue level of the material, and investigation of microstructural effects on the elastic anisotropy of this material remains as future work.

Several benefits exist from the use of VIC over other measures of deformation and strain (e.g., compliance-based techniques, strain gages, and extensometers), including:

- Deformations are measured directly on the specimen and thus do not reflect machine compliance in the test rig.
- Reinforcement effects of strain gages and adhesives on low modulus specimens are not induced using VIC.
- Material heterogeneity can be accounted for using VIC by looking for changes in slope of the position versus deformation curves, while most other techniques average strains over the entire specimen gage section.
- The top-out limit in VIC measurements is on the order of 500% strain, while strain gages have a much lower top-out limit. Thus the failure strain of many materials cannot be recorded with strain gages while VIC is well-suited for capturing large, and even nonlinear, strains up to the failure of most materials.
- Localized strain (around notches or material imperfections) can be assessed using VIC, while they cannot with strain gages or extensometers.

The drawbacks of VIC include:

- The minimum strain magnitude captured by the VIC system is limited by image correlation algorithms (currently, strains are not considered accurate below 500  $\mu\epsilon$ ).
- Set-up time can be significant when considering time to position and focus the cameras and calibrate the stereo system, although once the set-up is in place, testing can take place very rapidly.

### Conclusions

It is concluded that VIC is not only a viable alternative to strain gages and extensometers, but it is also more versatile due to its ability to capture full-field deformation and strain data up to high strain magnitudes on the order of 500%. Furthermore, it was shown in this study that VIC is capable of providing material property data consistent with other testing techniques and in sufficient detail to determine the nature of the anisotropy of manatee rib bone tensile properties. The results from this study suggest the need to assess shear properties about three orthogonal axes in order to assess the anisotropic nature of manatee rib bone shear modulus under orthotropic assumptions. Part 2 of this three part series (Chapter 7) will identify three shear moduli for manatee rib bone, while Part 3 (Chapter 8) will demonstrate a material symmetry characterization analysis for anisotropic materials such as manatee rib bone.

Table 6-1. Tensile properties of the Florida manatee rib bone. Mean values are presented as a function of specimen orientation along with the standard deviation and number of specimens used to calculate each.

Component	Elastic modulus (GPa)			Major Poisson's ratio			Minor Poisson's ratio		
	$E_1$	$E_2$	$E_3$	$\nu_{12}$	$\nu_{13}$	$\nu_{23}$	$\nu_{21}$	$\nu_{31}$	$\nu_{32}$
Mean	16.9	8.4	5.9	0.27	0.25	0.25	0.16	0.15	0.23
SD	1.5	1.2	2.2	0.04	0.04	0.04	0.06	0.07	0.08
$n$	13	13	13	13	13	11	13	13	12

Table 6-2. Summary of known manatee rib material properties

Investigators	Testing method	Bone source	Load or wave direction	Elastic modulus (GPa)	Poisson's ratio	Shear modulus (GPa)
Yan (2002)	Ultrasonic	Manatee rib	Transverse	18.13±1.77	0.253±0.021	7.24±0.711
Clifton (2005)	3-point bend	MSW0253 <sup>1</sup>	Transverse	$E_I=15.7$	-	-
		MSW0239 <sup>2</sup>	Transverse	$E_I=16.4$	-	-

<sup>1,2</sup>MSW0253 and MSW0239 are the ID's of two manatees used in the present study as well as the Clifton study



Figure 6-1. Articulated manatee skeleton. Specimens were pulled from the middle third of each rib in the center section of the manatees to reduce variability between specimens. Image courtesy of Roger Reep (department of physiological sciences, University of Florida).

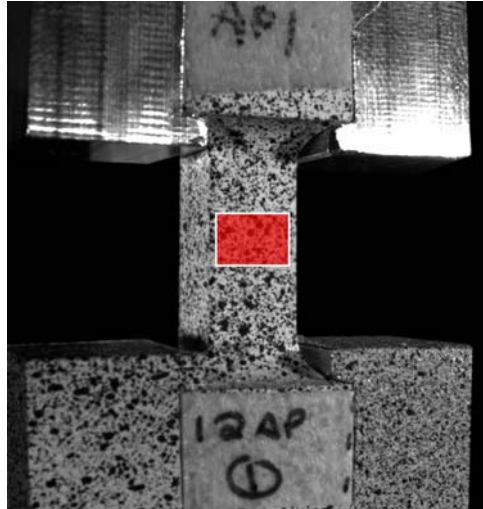


Figure 6-2. Visual image correlation performed on the gage section of a manatee rib bone tensile specimen. The highlighted section on the specimen is the area used for the visual image correlation (VIC) analysis.

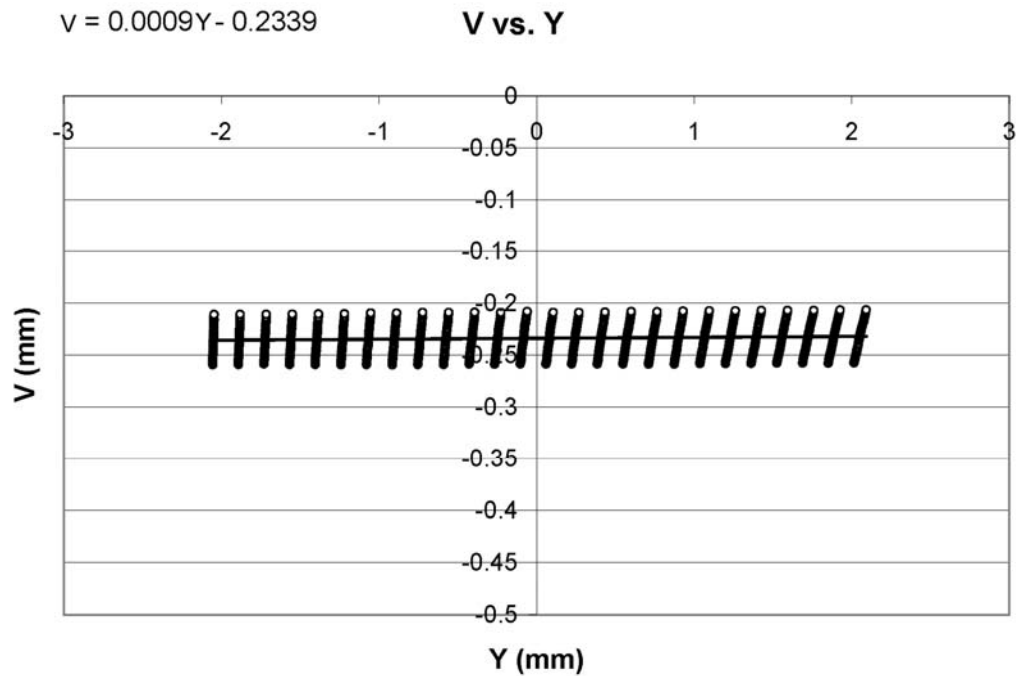


Figure 6-3. Plot of the deformation versus position data ( $dv$  vs.  $dy$ ) in the gage region of a tensile specimen. The strain at the load step plotted above was  $900 \mu\epsilon$ . Strain is calculated as the slope of the curve (i.e., the change in deformation with respect to the change in position is the strain ( $\epsilon_y = dv/dy$ )). The open circles represent all data points on the gage section while the line passing through the data points is a linear trend line used to fit the data in order to calculate strain.

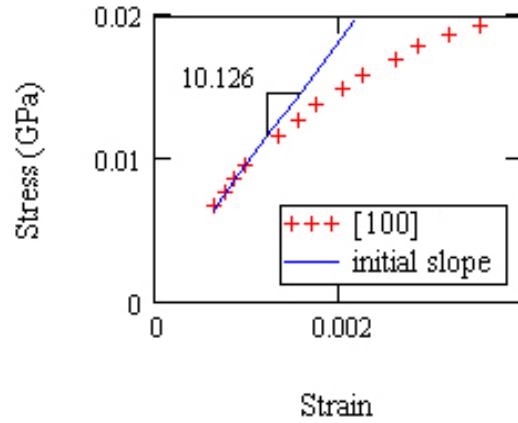


Figure 6-4. Stress-strain plot for a given load step during a VIC analysis. The initial slope of the stress-strain curve is the elastic modulus of the material. The elastic modulus for this particular specimen was 10.1 GPa. The +'s are representative of experimental data points from each load step, while the solid line represents the initial slope of the stress-strain curve.

## CHAPTER 7 ANISOTROPIC ELASTIC SHEAR PROPERTIES

### Short Summary

Shear testing of cortical bone presents many difficulties due to the limited thickness of cortical bone from most animals, the orthotropy of the material, and the hierarchical structure of bone. This study aims to assess a new method for the measurement of cortical bone shear properties that overcomes many of the challenges associated with shear testing of the material. Visual image correlation (VIC) is used to assess three orthogonal shear moduli of manatee rib (cortical) bone from Iosipescu specimens. Manatee rib bones are large, possess no marrow cavity, and are mostly cortical bone, so they are ideal for preparing large specimens (such as the Iosipescu specimen) of any material orientation. Shear strain from VIC is calculated as the sum of the slopes of the horizontal position versus vertical deformation and the vertical position versus horizontal deformation curves ( $\gamma_{xy} = dV/dX + dU/dY$ ). Shear modulus is taken as  $G_{xy} = \tau_{xy} / \gamma_{xy}$ , and is reported for both VIC and strain gage calculations.

Visual image correlation was performed directly on top of shear gages in order to provide a direct comparison of the results. Specimens were loaded on a uniaxial testing machine at a rate of 1 mm/min. For the VIC tests,  $G_{12} = 4.0 \pm 0.8$  GPa ( $n=3$ ),  $G_{13} = 4.1 \pm 0.4$  GPa ( $n=9$ ), and  $G_{23} = 2.7 \pm 0.4$  ( $n=5$ ), where the 1 direction corresponds with the proximodistal (longitudinal) direction of the rib, the 2 direction corresponds with the superficial-deep (in-plane transverse) direction of the rib, and the 3 direction corresponds with the craniocaudal (out-of-plane transverse) direction of the rib. For the shear gage tests,  $G_{12} = 4.9 \pm 0.4$  GPa ( $n=3$ ),  $G_{13} = 4.7 \pm 0.5$  GPa ( $n=2$ ), and  $G_{23} = 3.4 \pm 0.3$  ( $n=6$ ).

## Introduction

The anisotropic shear properties of manatee rib (cortical) bone have not yet been investigated. The shear properties of manatee rib bone are needed in order to fully characterize manatee rib bone material properties, which once characterized, can be useful in identifying critical loading scenarios that lead to failure of entire manatee ribs. The elastic constitutive matrix used to describe material behavior in response to loading is near complete with contributions from this study as well as a tensile properties study that aimed to determine the elastic moduli and Poisson's ratios of manatee rib bone under orthotropic assumptions (Chapter 6). Once manatee rib bone has been fully characterized and all of the elastic constitutive constants have been identified, accurate computer simulations that account for material anisotropy can be performed using finite element analysis to predict stress states and fracture properties of manatee rib in response to loading. To this point, material properties are known for only one orientation of manatee rib bone (Clifton et al. 2003; Clifton, 2005; Yan et al., 2006a, b, 2007) and computer simulations would not accurately depict the true response of manatee rib to loading with this limited input. This study will improve on the ability of computers to predict impact response of watercraft and manatees by identifying shear properties for three orthogonal orientations of rib bone.

Shear testing was done using Iosipescu specimens to determine the shear modulus of three orthogonal orientations of manatee rib bone. Iosipescu specimens were used in order to produce nearly pure-shear in the specimen gage sections (Iosipescu, 1967). This specimen is advantageous because test fixtures remove the translational and twisting motion of the upper and lower mounts caused by three-dimensional stresses generated by anisotropic materials during testing. Although size limitations of cortical bone from most animals prevent them from being prepared into Iosipescu specimens, manatee rib bone is large relative to other animals, it lacks a

medullary (hollow) cavity, and it has a large proportion of cortical bone to trabecular bone, so these specimens are appropriate for shear testing of manatee rib bone. Shear gages have been found to be an extremely accurate means of measuring shear strain in the test section of Iosipescu specimens (Ifju, 1994), and were used in the assessment of manatee rib bone shear modulus in this study.

A non-contact deformation analysis technique called visual image correlation (VIC) (Sutton et al., 1986 and 1991; Lichtenberger and Schreier, 2002) was also used in the calculation of manatee rib bone shear modulus. Visual image correlation has been used to assess biological tissue response to loading with applications including the investigation of tensile properties of bovine hoof horn, the mechanical behavior of arterial tissue, and the loosening of hip implants (Zhang and Arola, 2004). To the authors' knowledge, this is the first study to use VIC for the determination of shear properties of cortical bone. Visual image correlation discretizes a surface in order to provide 3-dimensional coordinates of points on the surface from images taken by two cameras placed at some distance from one another (Figure 7-1). Points on the object are then correlated between the images to provide object feature representation in 3D space. The analysis used here required that a random speckle pattern be applied to the test section of the specimen in order to provide sufficient contrast and texture to the specimen images for the correlation analysis to perform properly. Cross-correlation (CC) and normalized cross-correlation (NCC) are commonly used methods to determine object features (e.g., points, edges, etc.) for image correlation analyses. Once images have been correlated for a reference image of an unloaded specimen, the specimen is deformed and more stereoscopic images are taken. The position of the points in the deformed specimen images are compared to those from the reference image (Figure 7-2), and the full-field deformation of the specimen gage section can be found.

The aims of this study were to:

- Determine the shear modulus for 3-orientations of manatee rib bone using VIC and shear gages simultaneously
- Characterize the anisotropy of manatee rib bone shear modulus
- Determine if VIC is a viable alternative to shear gages in the calculation of shear modulus by comparison of the results
- Compare shear modulus results with those from ultrasound studies
- Determine the repeatability of each technique by performing cyclic tests and looking at the coefficient of variation ( $CV$ ) for all cycles

### **Methods**

Manatee rib bones were obtained under US Fish and Wildlife permit #MA067116-0 issued to the Florida Fish and Wildlife Conservation Commission's (FWC) Marine Mammal Pathology Lab (MMPL). Use of the tissue was governed by University of Florida Institutional Animal Care and Use Committee (IACUC) protocol #E407. Two center ribs (#'s 9 and 10 of 17-19 ribs) were selected for this study from two adult male manatees (Figure 7-3). The manatee ribs were stored with flesh intact to preserve material properties (An and Draughn, 2000) at  $-20^{\circ}$  Celsius, a temperature chosen to avoid freezer burn and, hence, tissue property degradation. Shear specimens were taken from the middle third of the selected ribs to meet specimen size requirements and to prevent site specific variation in material properties (Figures 7-4 and 7-5).

Iosipescu specimen dimensions are shown in Figure 7-6. The length dimension of one Iosipescu specimen orientation (oriented to obtain shear modulus  $G_{13}$ ) was limited by the cross-sectional width of manatee rib bone, thus the specimen length for this orientation was less than that used for the other two orientations. The cross-section of the middle portion of the ribs used in this study was elliptical in shape, with a minor axis dimension (in the superficial-deep direction) of  $\sim 40$  mm and a major axis dimension (in the craniocaudal direction) of  $\sim 65$  mm.

The middle sections of the ribs were cut into large, rectangular blocks using a wet band saw. The blocks were then milled to their dimensions, while keeping the thickness dimension as large as possible. Notches were milled into the specimens by mounting the specimens at a 45° angle relative a 1.59-mm radius end-mill. The specimens were then sliced to their appropriate thicknesses using a 102-mm wafering blade attached to an IsoMet low speed saw (Buehler Ltd., Lake Bluff, IL). Specimens were kept under constant irrigation with water during all machining operations. Specimens were wrapped in gauze, soaked in saline solution, and refrigerated until being brought to room temperature for shear gage and VIC preparation just before testing.

Shear gages (Vishay Micro-Measurements, Raleigh, NC) were mounted to the front and back test section of nine specimens ( $n=3$  for  $G_{12}$  and  $n=6$  for  $G_{23}$  specimens) and to the front test section of two  $G_{13}$  specimens. The test section of these and seven additional  $G_{13}$  specimens were then spray painted white (for increased contrast) and speckled with black spray paint to generate a random speckle pattern used by the VIC stereo system during image correlation (Figures 7-7 and 7-8). Specimens were fixed in mounts designed to prevent translation and twisting motion caused by 3-D stresses generated by anisotropic materials during testing. Specimens were loaded in tension on an MTI uniaxial loading machine (Measurement Technology, Inc., Roswell, GA), resulting in the generation of shear strains in the test section of the Iosipescu specimen. The  $G_{12}$  and  $G_{23}$  specimens were loaded to 650 N and unloaded, rotated 180° without removing the specimens from the mounts, and the test was run again. This was done to allow for VIC to be performed on both the front and back specimen test sections in case if results were to differ due to specimen preparation or to the test fixture. Results were averaged for both loading-unloading cycles. The two  $G_{13}$  specimens with a shear gage adhered to a single test section were loaded cyclically ( $n=11$  and  $n=6$ ) from 0 to 650 N while VIC was performed simultaneously with shear

gage testing. The seven  $G_{13}$  specimens prepared for VIC alone were tested to failure. All specimens were loaded at a rate of 1 mm/min.

The VIC system used to capture test section deformation information consisted of Cinegon CM120 lenses (Schneider-Kreuznach, Bad Kreuznach, Germany) mounted to a pair of Retiga 1300 digital cameras (Quantitative Imaging Corporation, Burnaby, British Columbia, Canada), which were arranged to form a near equilateral triangle with the specimens. The cameras were calibrated with a dot matrix calibration grid generated using custom software provided by Correlated Solutions, Inc. and image correlation software (VIC-3D Digital Image Correlation v.2006.0.0, Correlated Solutions, Inc., West Columbia, SC). Load data was monitored using a 1000-lb load cell (Interface SM-1000-38, Scottsdale, AZ), received by a National Instruments SCXI-1321 terminal block designed for use with the SCXI-1121 signal amplifier (National Instruments Corporation, Austin, TX), and logged using a custom Labview program (Labview v.7.0, National Instruments Corporation, Austin, TX). Correlation analyses were performed on the gage sections of loaded specimen images (Figure 7-3) using VIC3D software. Output from the VIC analyses included position and deformation for each data point on the specimen gage sections. Output files were exported from VIC3D and Labview and input into a custom Mathcad program (Mathcad v.12.1, Mathsoft Engineering and Education, Inc.) for further data reduction and analysis. Shear strain was calculated from VIC data by adding the horizontal position versus vertical deformation and the vertical position versus horizontal deformation curves ( $\gamma_{xy} = dV/dX + dU/dY$ ) (Figure 7-9). Shear strains calculated for each load step were averaged over the linear range of the stress-strain curves for each specimen tested. The strains from the front- and back-mounted shear gages were averaged to remove bending and twisting effects. Shear modulus was taken as  $G_{xy} = \tau_{xy} / \gamma_{xy}$  for both VIC and strain gage calculations.

## Statistics

One-way ANOVA was performed on the shear modulus means for all specimen orientations to determine if any means were significantly different from any other orientation as determined by both VIC and shear gages. Independent group t-tests were performed on all possible pairs of specimen orientations for both VIC and shear gage results to determine which means differed (if any). An independent group t-test was performed to determine if there was a significant difference between VIC and shear gage shear modulus means for any specimen orientation. Significance was taken when  $p < 0.05$ .

## Results

Results are provided in Tables 7-1 and 7-2. Mean values and standard deviations (*SD*) are presented for all shear moduli. Cyclic testing resulted in  $G_{13} = 4.6 \pm 0.6$  (VIC) and  $G_{13} = 5.3 \pm 0.2$  (shear gage) for the 11 cycles performed on specimen 1, and  $G_{13} = 3.6 \pm 0.2$  (VIC) and  $G_{13} = 4.2 \pm 0.1$  (shear gage) for the 6 cycles performed on specimen 2. The coefficient of variation (*CV*) for specimens 1 and 2 were 9% and 6% for VIC and 4% and 2% for shear gages. Shear modulus  $G_{12}$  was found to be  $4.0 \pm 0.8$  ( $n=3$ ) for VIC and  $4.9 \pm 0.4$  ( $n=3$ ) for shear gages, an 18% difference. Shear modulus  $G_{13}$  was found to be  $4.1 \pm 0.4$  ( $n=9$ ) for VIC and  $4.7 \pm 0.5$  ( $n=2$ ) for shear gages, a 13% difference. Shear modulus  $G_{23}$  was found to be  $2.7 \pm 0.4$  ( $n=5$ ) for VIC and  $3.4 \pm 0.3$  ( $n=6$ ) for shear gages with a 21% difference.

## Statistical Results

One-way ANOVA revealed that at least one of the specimen orientation means was different for both VIC and shear gage calculations of shear modulus ( $p < 0.001$ ). Independent group t-tests showed that  $G_{12}$  and  $G_{13}$  did not significantly differ for either VIC or shear gage calculations ( $p = 0.9139$  and  $p = 0.5933$ , respectively), while  $G_{12}$  differed from  $G_{23}$  ( $p = 0.0226$  for VIC;  $p < 0.001$  for gage), and  $G_{13}$  differed from  $G_{23}$  ( $p < 0.001$  for VIC;  $p = 0.0039$  for gage).

Independent group t-tests demonstrated a lack of significant difference between VIC and shear gage means for both the  $G_{12}$  and  $G_{13}$  moduli ( $p=0.1516$  and  $p=0.0991$ , respectively), although results for  $G_{23}$  differed significantly ( $p=0.0083$ ).

### **Discussion**

This was the first study to use VIC for the determination of cortical bone material properties and to characterize the shear modulus of manatee rib bone. Shear modulus  $G_{23}$  was found to differ from  $G_{12}$  and  $G_{13}$ , while  $G_{12}$  and  $G_{13}$  did not significantly differ from one another, implying that manatee rib bone shear modulus is transversely isotropic.

Visual image correlation results agreed reasonably well with those from shear gages, which were adhered to the specimen test sections for simultaneous comparison with VIC. It appears that VIC is a viable alternative to shear gages for the calculation of shear modulus as noted from the lack of significant difference between VIC and gage values for  $G_{12}$  and  $G_{13}$ . The significant difference between VIC and shear gage values for  $G_{23}$  specimens may be in part due the fact that  $G_{23}$  specimens were shorter than specimens from the other two orientations. Perhaps the stress state on the front and back of the Iosipescu specimen is influenced by specimen length, since it is possible that specimen slip can occur if not enough material is gripped in the mounts. The averaging of shear gage values from the front and back of the specimen would account for differences in shear stress magnitudes on the front and back of a specimen. However, the VIC results would not capture this difference since VIC was performed on only the front-facing test section of the specimens.

Visual image correlation position and deformation data were put into a shear strain algorithm that averages data across the entire test section. Figure 7-11 shows the sensitivity of VIC calculated shear modulus to shear strain. Shear modulus appears rather scattered until it collapses to a single value above  $\sim 700 \mu\epsilon$ . Shear gages directly measure shear strain on a

specimen test section using a  $\pm 45^\circ$  foil pattern. Shear gages are simple to align since they are designed specifically for the Iosipescu specimen (Ifju, 1994). Shear gage results have proven to be quite reliable for assessing composite material shear properties, because they account for the gradient in shear strain across the specimen test section by integrating over the entire test section (Ifju, 1995).

Results from this study do not entirely agree with those from an ultrasound study on the material properties of manatee rib bone (Yan, 2002). Yan's study reported a shear modulus of  $7.24 \pm 0.71$  GPa for manatee rib bone (with no mention of which shear modulus was measured), while the largest shear modulus measured in this study was from strain gage readings for the  $G_{12}$  orientation ( $4.9 \pm 0.4$  GPa). The differences between these studies may be at least partially explained by the common observation of ultrasonic methods yielding higher results than mechanical testing methods. Material differences could also have influenced the difference in results. For instance, age, porosity, mineral density, and location within a manatee or within a specific rib all have potential for influencing the results of a shear modulus test. Differences in values were also found between shear gage and VIC results in the current study: The shear modulus from the gages was always slightly higher than that from VIC. Higher shear modulus calculated from strain gages are the result of lower strain readings being output from the shear gages than from the VIC system. This discrepancy can be explained by the size differences of the effective gage region for each analysis method. The gage length used for the VIC analysis is slightly less than the effective gage length for the shear gages. A shorter effective gage length results in a higher shear strain measurement, because the near zero component of the non-uniform shear strain distribution is removed when averaging shear strain calculation (Figure 7-14). It is impossible to avoid a partial reduction in size of the selected VIC gage region, because

of the algorithms used by the VIC software to map localized deformations to the gage region. Therefore, measured shear strains will likely always be slightly smaller using VIC than when using shear gages. It should be noted that shear modulus differences were only significant for one of the three tested orientations, thus the influence of the reduced gage length from the VIC analysis compared to that from the shear gages is not substantial.

### **Conclusions**

In conclusion, shear modulus was found for 3 presumably primary orthogonal orientations of manatee rib bone using both VIC and strain gages. Manatee rib bone shear modulus was found to be transversely isotropic. Visual image correlation results consistently over-predicted strain gage shear strain due to smaller effective gage lengths being used in the VIC analyses than the shear gage analyses, causing a slight under-prediction of shear modulus in all cases (although this finding was not statistically significant for two of the three orientations tested). Visual image correlation is slightly less repeatable than shear gages when cyclically testing a single specimen ( $CV \leq 9\%$  for VIC and  $\leq 4\%$  for shear gages). Results from this study did not entirely agree with those from an ultrasound study conducted on manatee rib bone, although the higher ultrasound values compared to mechanical test values were consistent with findings from other researchers. Visual image correlation and shear gage results from this study agreed reasonably well, and the slight differences in values can be explained by the difference in effective gage lengths between the two methods. It may therefore be possible to develop a correction factor to account for the slight under-prediction of shear modulus by VIC. The findings from this study demonstrate that VIC is a viable alternative to shear gages in the calculation of cortical bone shear modulus.

Table 7-1. Shear modulus and coefficient of variation (*CV*) from cyclic tests. Mean values are presented  $\pm$  standard deviations.

Cyclic tests	Specimen 1 (11 cycles)		Specimen 2 (6 cycles)	
	$\bar{G}_{13}$ (GPa)	<i>CV</i> (%)	$\bar{G}_{13}$ (GPa)	<i>CV</i> (%)
VIC	4.6 $\pm$ 0.4	9	3.6 $\pm$ 0.2	6
Gage	5.3 $\pm$ 0.2	4	4.2 $\pm$ 0.1	2

Table 7-2. Shear modulus of three orthogonal orientations of manatee rib bone. Mean values are presented  $\pm$  standard deviations along with the number of specimens used (*n*).

Shear tests	Shear modulus (GPa)		
	$G_{12}$	$G_{13}$	$G_{23}$
VIC	4.0 $\pm$ 0.8 ( <i>n</i> =3)	4.1 $\pm$ 0.4 ( <i>n</i> =9)	2.7 $\pm$ 0.4 ( <i>n</i> =5)
Gage	4.9 $\pm$ 0.4 ( <i>n</i> =3)	4.7 $\pm$ 0.5 ( <i>n</i> =2)	3.4 $\pm$ 0.3 ( <i>n</i> =6)
Difference (%)	18	13	21

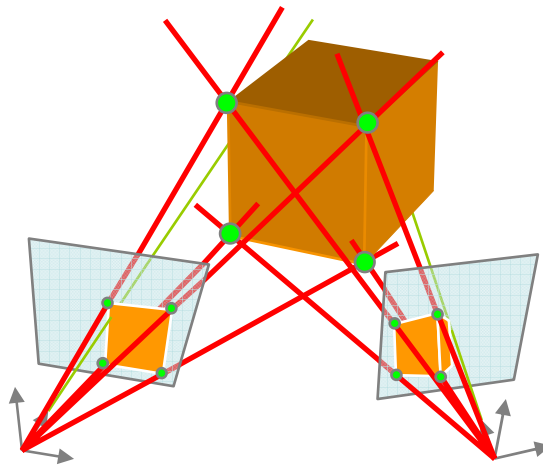


Figure 7-1. Three-dimensional surface as seen by two imaging sensors (courtesy of Correlated Solutions, Inc, West Columbia, SC). The image demonstrates the stereographic set-up used in VIC analyses. The depicted imaging planes represent the 2-D viewing area for each camera.

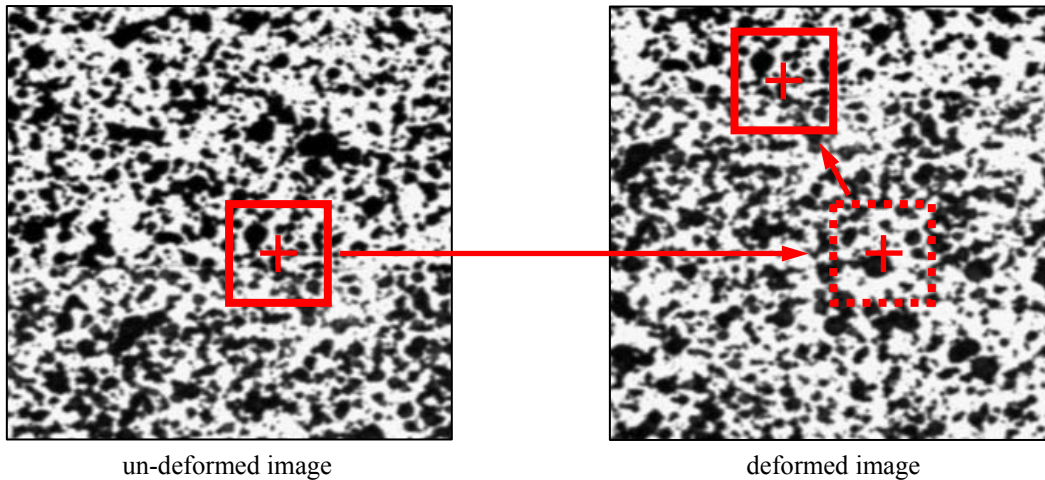


Figure 7-2. Movement of a sample square subset used for cross-correlation function estimation in the VIC analysis. Image courtesy of Correlated Solutions, Inc., West Columbia, SC.

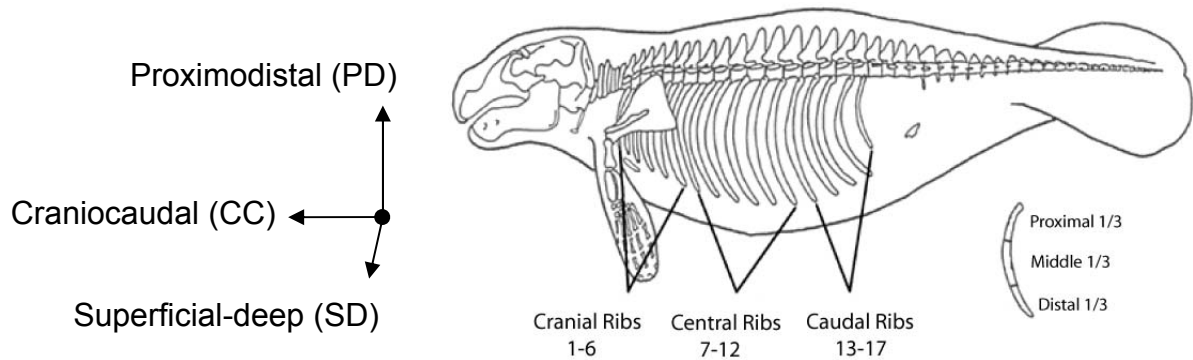


Figure 7-3. Manatee skeleton. Modified with permission from Yan, J., 2002. Biomechanical properties of manatee rib bone and analytical study using finite element analysis. M.S. Thesis, University of Florida, Gainesville, Figure 3-2, p. 19.

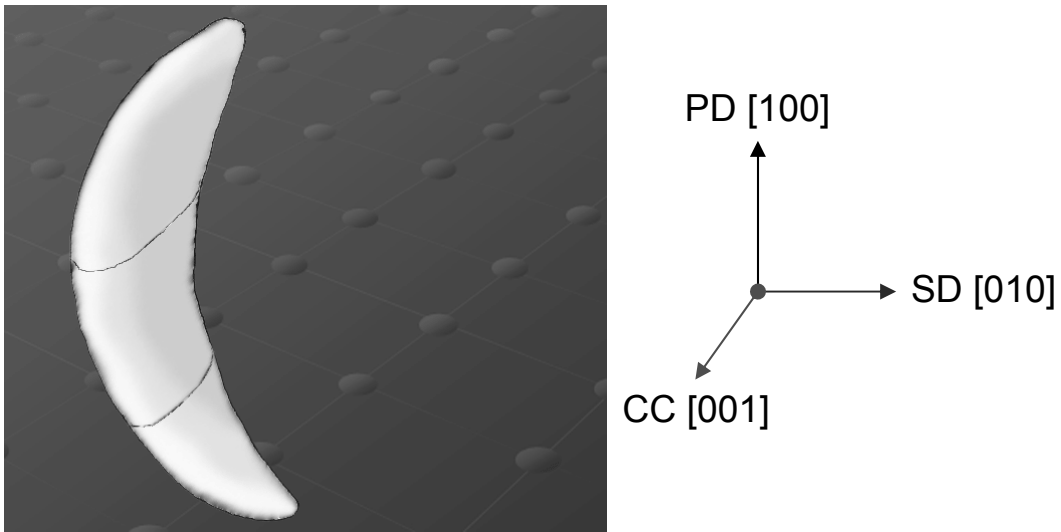


Figure 7-4. The middle third of each rib was used for the analysis to reduce potential site-specific variability between specimens. The coordinate system used in the analysis is defined in terms of both anatomical directions and Miller indices. The proximodistal (PD) direction corresponds to the [100] direction in Miller indices, while the superficial-deep (SD) direction corresponds to the [010] direction and the craniocaudal (CC) direction corresponds to the [001] direction.

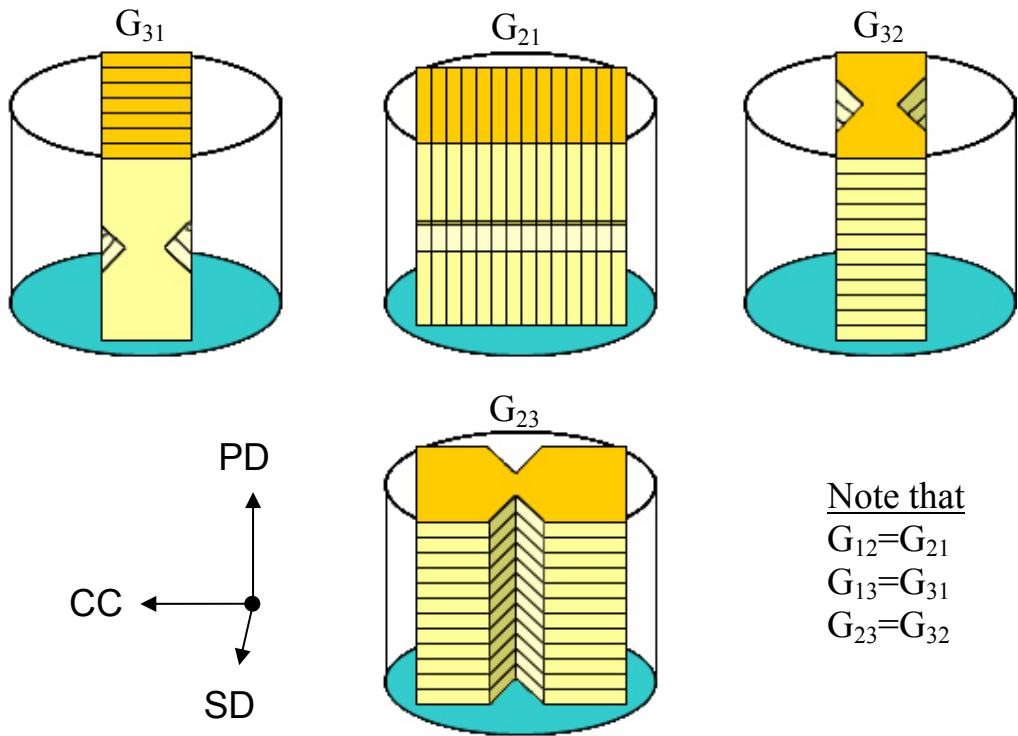


Figure 7-5. Orientation and sectioning of the shear specimens used in this study. The number of specimens available from each section depended on the dimensions of that section. Six to eight specimens were obtained for the  $G_{31}$  (reported herein as  $G_{13}$ ) orientation, while eight to ten could be prepared for the  $G_{21}$  (reported herein as  $G_{12}$ ) orientation. The number of specimens available from the  $G_{31}$  and  $G_{13}$  orientations depended on the length of the section cut for those orientations, rather than being limited by the ribs cross-sectional dimensions.

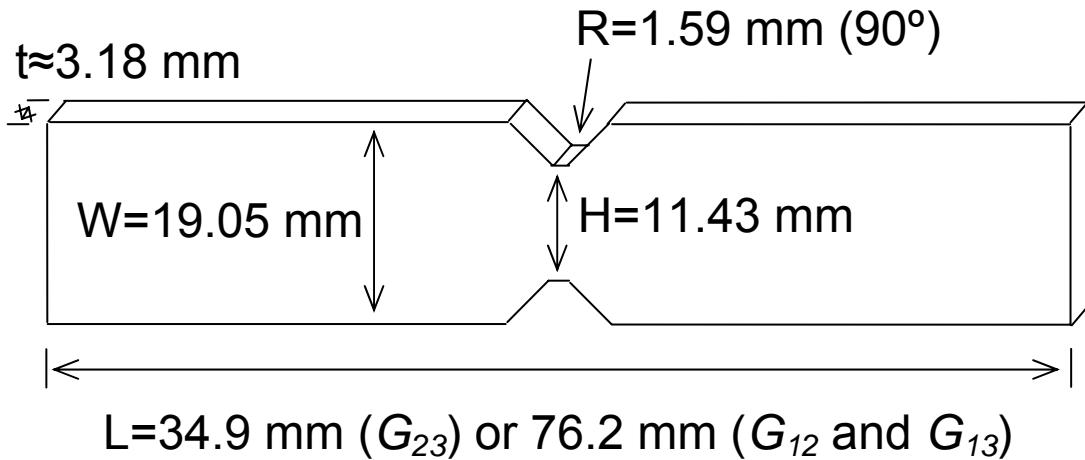


Figure 7-6. Iosipescu specimen dimensions. The length of the  $G_{23}$  specimens was limited by the physical dimensions of the manatee rib cross section.

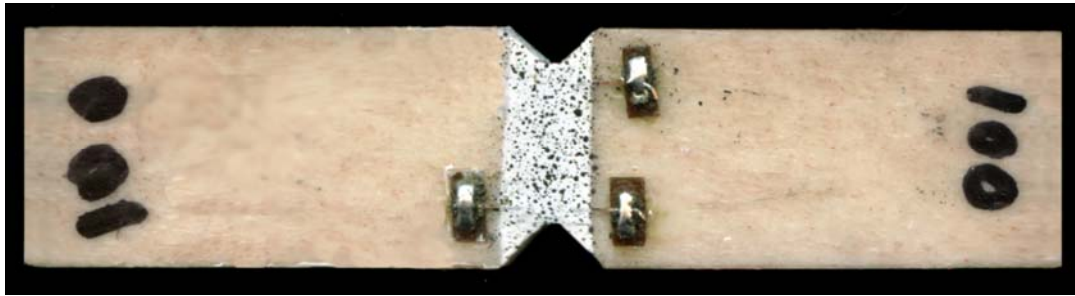


Figure 7-7. Iosipescu specimen prepared for simultaneous shear gage and VIC testing. The test section first had a shear gage applied followed by being spray painted white and speckled with black spray paint for the VIC analysis.

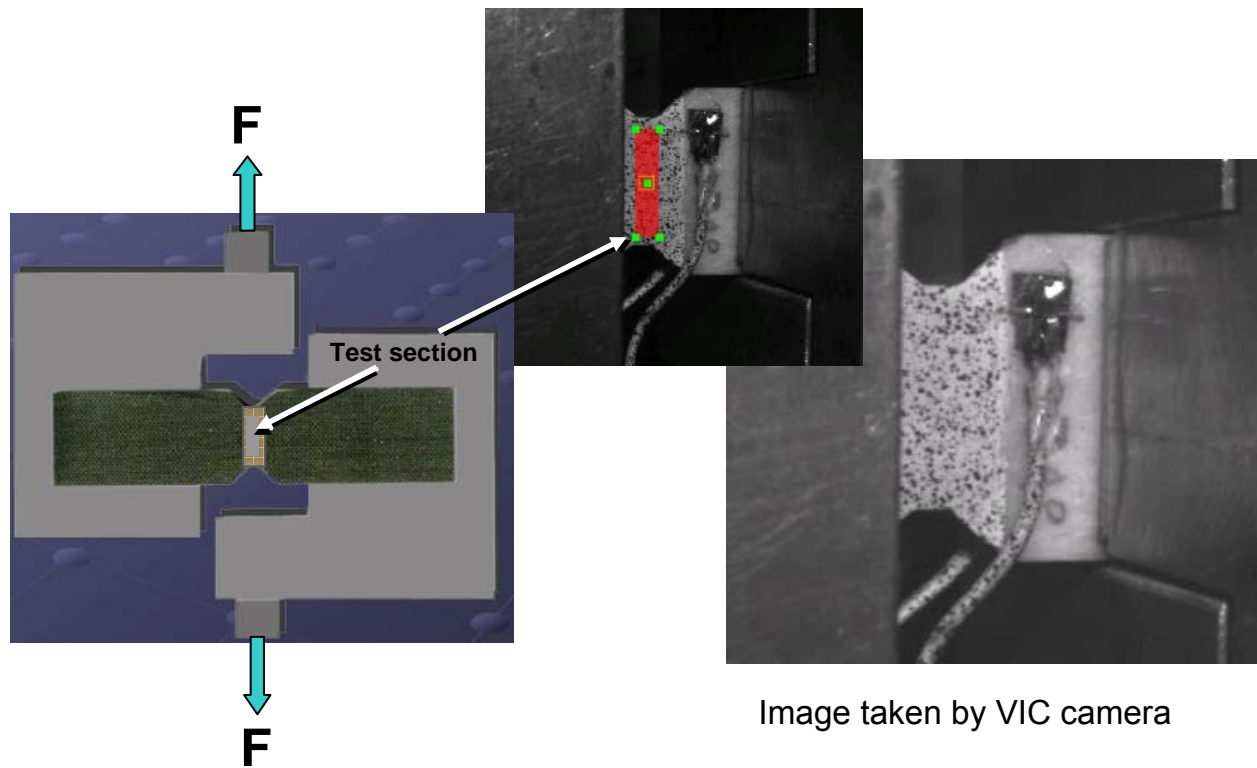


Figure 7-8. Image showing the test section and loading of an Iosipescu specimen prepared for simultaneous VIC and shear gage testing. A uniaxial load is applied to the specimen (left), while a shear gage and the VIC system measure deformations in the test section (left and middle images). An actual image used in the VIC analysis is shown in the image to the right. The image is partially obstructed by the large Iosipescu specimen holders, although the stereographic set-up was arranged to allow for the test section to be in view of both cameras.

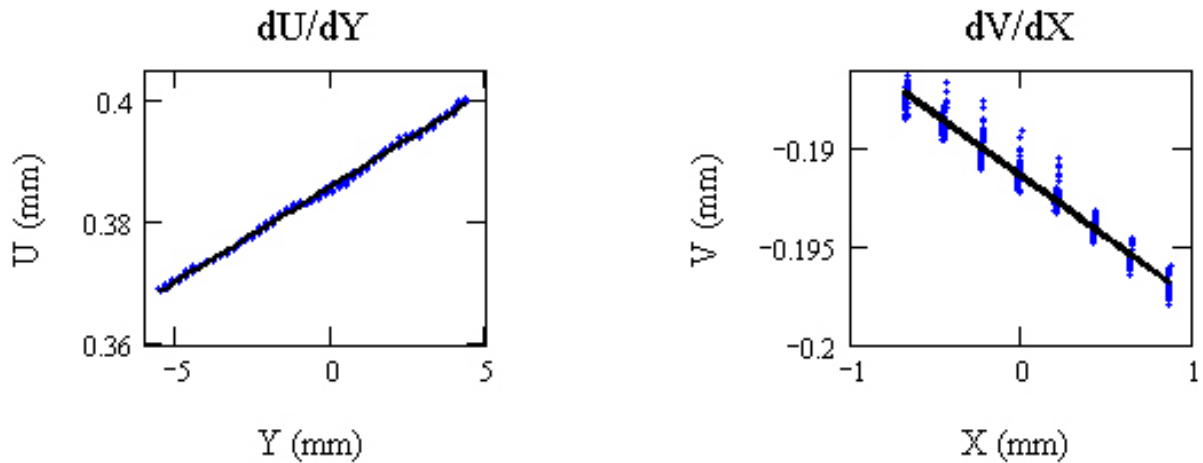


Figure 7-9. Plots showing the high correlation of the  $dU/dY$  and  $dV/dX$  data points across the entire test section of an Iosipescu VIC specimen. The blue dots represent VIC data points captured from the test section at a given load level, while the slope of the linear trend line was used in the shear strain algorithm ( $\gamma_{xy}=dU/dY+dV/dX$ ).

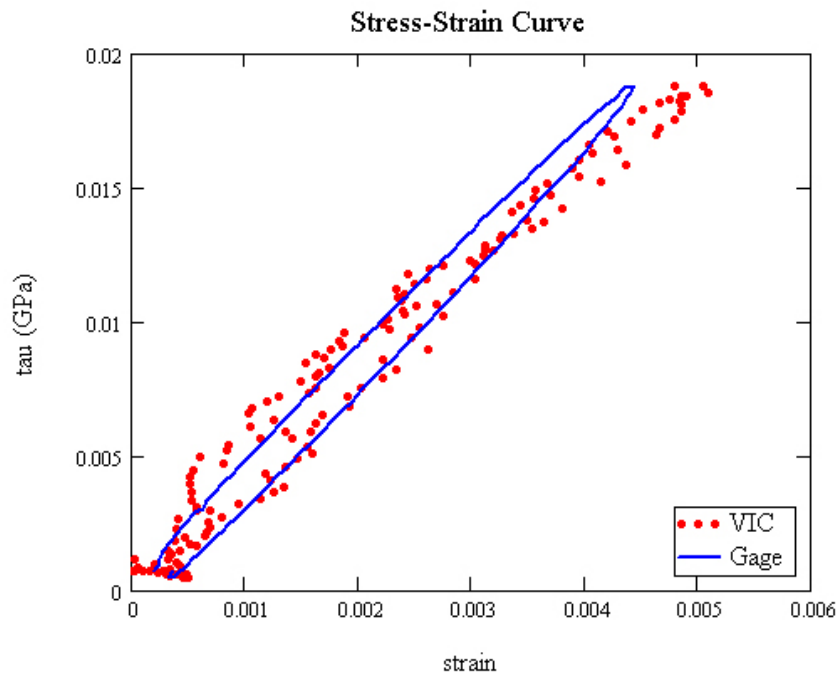


Figure 7-10. Typical stress-strain plot obtained from VIC and shear gages. The peak strain measured by VIC (dots) is larger than that measured by shear gages (line).

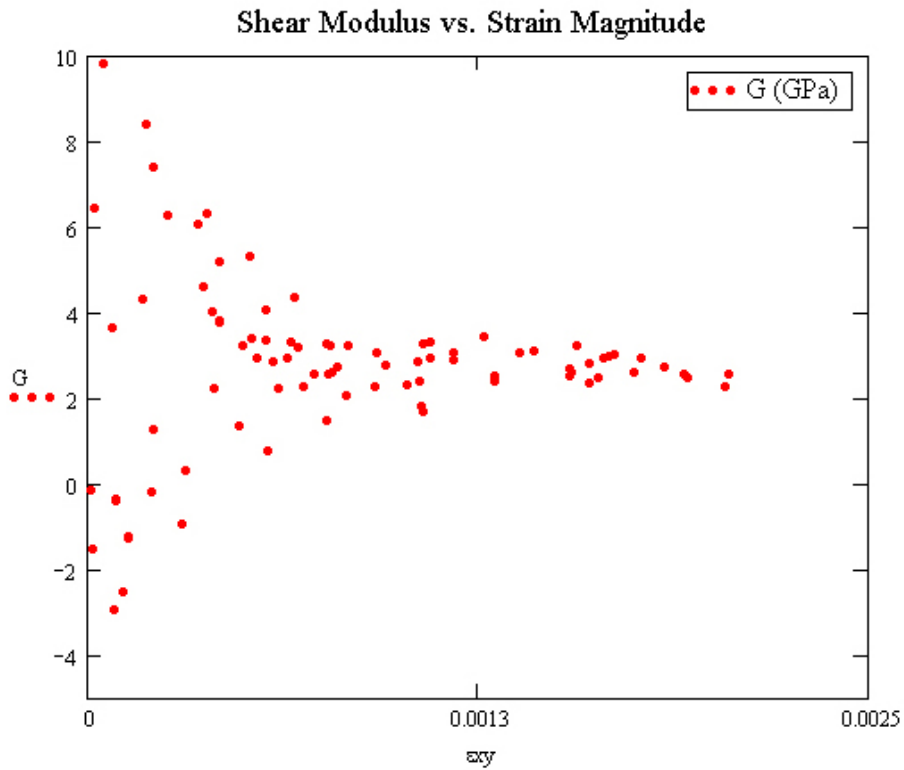


Figure 7-11. Sensitivity of VIC analysis to shear strain magnitude. Note the convergence of shear strain values at this load step at strains approaching and above  $1000 \mu\epsilon$ . This plot demonstrates the inability of the VIC system and shear strain algorithm to accurately capture strains below this cut-off value.

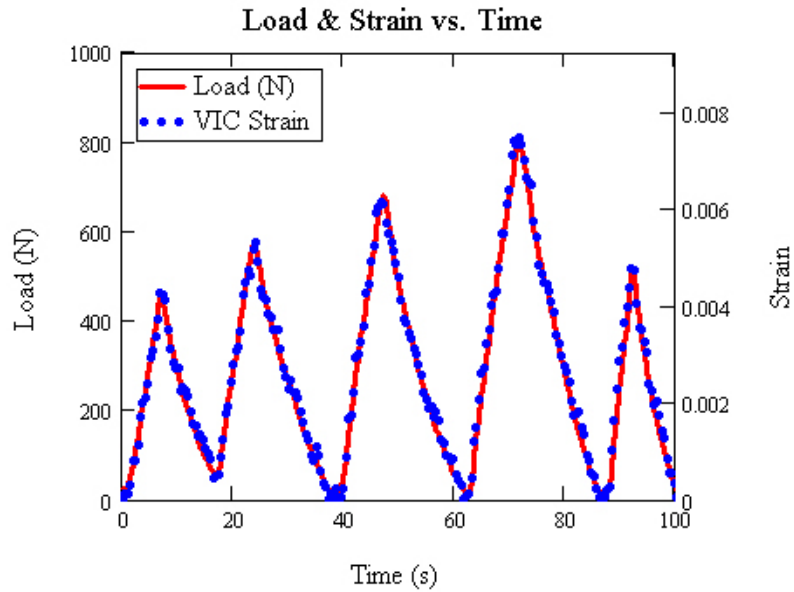


Figure 7-12. Plot showing how VIC-calculated shear strain accurately follows cyclic load curves. Note that this plot was not used in the cyclic analysis and is presented only to demonstrate how well VIC can track load even at low load levels.

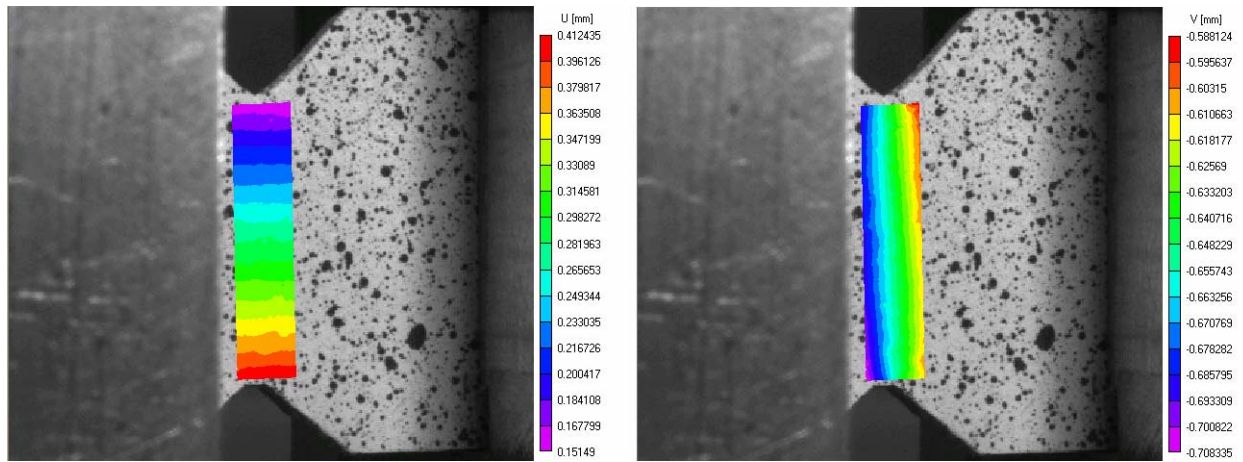


Figure 7-13. (Left)  $U$  and (right)  $V$  deformation contour plots for the test region of an Iosipescu shear specimen during a VIC analysis. For the pictured load step,  $U$  deformations ranged from 0.15 (purple) to 0.41 mm (red), while  $V$  deformations ranged from -0.59 (red) to -0.71 mm (purple).

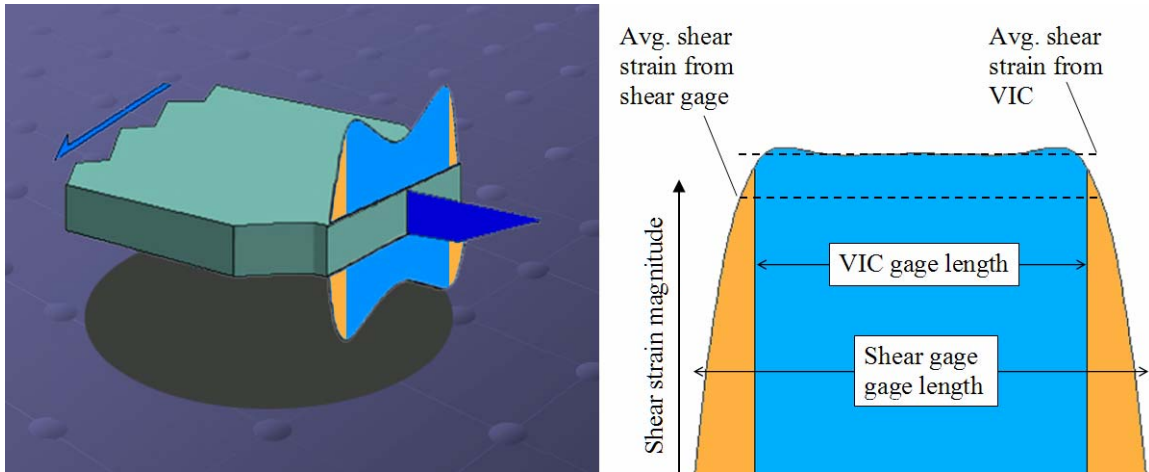


Figure 7-14. Shear strain distribution and effective shear gage and VIC gage lengths in manatee rib bone Iosipescu specimens. Note that shear strain can vary through the thickness of a specimen (dark blue region in the left image) and that shear strain is non-uniform across the test section. Also note the difference in average shear strain measured by VIC and shear gages resulting from the reduced effective VIC gage length (right). The blue region represents shear strain measured by VIC, while the orange region represents the additional shear strain measured by shear gages.

## CHAPTER 8 MATERIAL SYMMETRY ANALYSIS

### **Short Summary**

Traditionally, bone is presumed to be either transversely isotropic or orthotropic with no verification of the material's symmetry. Models that utilize incorrectly defined material properties (often assuming the material is isotropic) are prevalent in the literature, although the accuracy of such models must be called into question. A proper material properties characterization analysis requires verification of the material symmetry. In Chapters 6 and 7, experiments were performed on tensile and shear specimens, respectively, oriented about three axes presumed to be principal material axes. These tests were used to determine the nine independent elastic constants required to define the constitutive behavior of an orthotropic material. Miller indices were used to define material axes, with the [100] direction defining the proximodistal axis, [010] defining the superficial-deep axis, and [001] defining the craniocaudal axis in anatomic coordinates. This study examines the symmetry of the material by comparing predicted and experimentally determined strains in off-axis specimens. Tensile tests were performed on specimens oriented along three off-axis directions ([110], [101], and [011]). Visual image correlation was used as the experimental measure to determine the strain in each off-axis specimen, while three material symmetry models (isotropic, transversely isotropic, and orthotropic Hooke's law) were each used to predict strain the off-axis directions from the previously determined nine independent elastic constants. The material symmetry was determined by quantifying the difference between the predicted and experimental strain values and choosing the model that best fit the experimental data. The agreement between predicted and

experimental strains in all three off-axis directions was the greatest for the orthotropic model, thus it was concluded that manatee rib bone is orthotropic.

### **Introduction**

Cortical bone is generally assumed to be either transversely isotropic (Yoon et al., 1976; Gotzen et al., 2003; Dong and Guo, 2004) or orthotropic (Ashman et al., 1984; Hoffmeister et al., 2000). However, very little effort has gone into verifying the symmetry of the material. Part of the difficulty in characterizing the symmetry of bone comes from specimen size limitations. Cortical bone is generally quite thin depending on the location and the animal from which the specimens are harvested (An and Draughn, 2000). In cancellous bone, size limitations have been overcome by the use of micro-finite-element ( $\mu$ FE) models generated from high resolution images of the trabecular structure (van Rietbergen et al., 1996; van Rietbergen et al., 1998). Testing can take place along any number of directions using this FE-based direct mechanics approach, and the elastic anisotropic constitutive behavior of the bone can be found. In cortical bone, micro- and ultra-structural constituents are responsible for the anisotropy of the material (Turner et al., 1995) and a similar FE approach can be used to model the material (Gotzen et al., 2003). However, the technique has not yet been used to fully reveal cortical bone elastic anisotropic constitutive properties. The method that Gotzen et al. (2003) used to reveal localized properties is quite involved because it requires the histological sectioning, imaging, and modeling of many slices of bone, thus the analysis is rather time consuming. Yang et al. (1999) made use of a previously developed methodology for averaging anisotropic elastic constants called spectral decomposition (Mehrabadi and Cowin, 1990) in order to demonstrate the compositional dependence of the elastic constants of cancellous bone and wood. While the wood data was assumed to be orthotropic from the start, the cancellous bone data was collected in a

sufficient manner to fully populate the anisotropic elastic constants matrix using  $\mu$ FE. Yang et al. demonstrated with 95% certainty that cancellous bone is orthotropic. Due to the *a priori* assumption for the material symmetry of wood, no such conclusion could be made to verify the orthotropy of the material (i.e., not enough data was available to statistically reduce the wood dataset as was done for cancellous bone). The present study demonstrates that with the additional testing of an off-axis (non-principal) specimen orientation, that testing under an *a priori* assumption of material symmetry is sufficient for concluding the symmetry of a material. The specific objective of the present investigation is to determine the symmetry model that best fits experimental data collected from off-axis specimens. This objective is accomplished by comparing experimentally determined strains in off-axis specimens with those found by transforming the isotropic, transversely isotropic, and orthotropic compliance matrix in Hooke's law.

An essential component of the present analysis is to identify the principal material directions of manatee rib bone. The longitudinal and two transverse axes are chosen according to the geometry of the bone's cross-section. A caveat here is that principal material axes of micro and ultrastructural bone structures may not necessarily align with external geometry (Turner et al., 1995), but given the structure-function relationship of bone (Cowin, 2002), a good initial guess for the principal material axes of an elliptically-shaped bone such as the rib places the principal axes along the major and minor axes of the cross-section. An alternative approach for determining the principal axes of bone would be to examine the microstructure (Wirtz et al., 2000) and orientation of constituents of the tissue (Gotzen et al., 2003). In our study, it is assumed that principal material directions correspond to macroscopic bone geometry.

The nomenclature used in our analysis crosses several disciplines in order to simplify mathematics involved with coordinate system transformations as well as to make clear the specimen orientations relative the anatomic coordinate system. Miller indices, traditionally used in the analysis of crystalline materials, were used to define material axes, with the [100] direction defining the proximodistal axis (also referred to as the 1-axis), [010] defining the superficial-deep (2) axis, and [001] defining the cranial-caudal (3) axis in anatomic (material) coordinates.

Chapters 6 and 7 provide the results required to fully populate the orthotropic compliance matrix. Manatee rib bone tensile modulus was found to differ in all three orthogonal directions (Chapter 6), while shear modulus was found to vary in one direction but not the other two (Chapter 7). Although it would appear that manatee rib bone is orthotropic at the macroscopic length scale due to findings from the tensile tests, the symmetry must be verified to ensure that the orthotropic material model best predicts material response to loading in non-principal directions. Our analysis is used to discern which material model best predicts strains in off-axis specimens. The method utilized in our study for examining the material symmetry of a previously uncharacterized material minimizes the number of tests required to verify the symmetry of the material, since only one additional specimen axis is required to be tested above and beyond the number of tests required for the material model chosen for the analysis.

### **Material Symmetry**

There are a total of eight types of linear elastic material symmetry: monoclinic, triclinic, orthotropic, cubic, tetragonal, trigonal, hexagonal (transversely isotropic), and isotropic (Mehrabadi and Cowin, 1990). The case of no material symmetry is called anisotropy. Our analysis will discern which material characterization best matches the observed constitutive response of manatee rib bone. In order to achieve this goal while minimizing the number of required tests, manatee rib is initially assumed to be orthotropic, which, other than mono- and tri-

clinic, exhibits the least symmetry. Our analysis is not capable of discerning which lesser symmetry scenario best fits the material or if anisotropy is a better fit, but it will distinguish between greater symmetries.

### **Hooke's Law**

Hooke's law relates the stresses to the strains in a material. Various forms of Hooke's law exist depending on the number of elastic constants required to define the constitutive matrix. Several forms of Hooke's law are presented to describe the elastic constitutive response of materials with different material symmetries. The general form of Hooke's law is provided in Equation 8-1.

$$\varepsilon_j = s_{ij}\sigma_i \quad (\text{Eq. 8-1})$$

where  $\sigma_i$  and  $\varepsilon_j$  are the components of the stress and strain tensors, respectively, and  $s_{ij}$  is the compliance matrix for  $i,j=1\dots6$ . Equation 8-1 can be rewritten in terms of the stiffness matrix,  $c_{ij}$ , which can be used to solve for stresses from strains.

$$\sigma_i = c_{ij}\varepsilon_j \quad (\text{Eq. 8-2})$$

Material properties can be calculated from Hooke's law given that the stresses and strains are known. Example 8-1 demonstrates the calculation of material properties from strain measurements and applied loads.

### **Isotropic Materials**

The simplest form of Hooke's law is used to describe isotropic materials. Isotropic materials generally have randomly distributed constituents, which causes these materials to have properties that are invariant to rotation (Boresi and Schmidt, 2003). This means that isotropic

materials respond identically to loading in all directions. The compliance matrix for an isotropic material is written as follows:

$$[c]^{-1} = [s] = \begin{pmatrix} \frac{1}{E} & -\frac{\nu}{E} & -\frac{\nu}{E} & 0 & 0 & 0 \\ -\frac{\nu}{E} & \frac{1}{E} & -\frac{\nu}{E} & 0 & 0 & 0 \\ -\frac{\nu}{E} & -\frac{\nu}{E} & \frac{1}{E} & 0 & 0 & 0 \\ 0 & 0 & 0 & \frac{1}{G} & 0 & 0 \\ 0 & 0 & 0 & 0 & \frac{1}{G} & 0 \\ 0 & 0 & 0 & 0 & 0 & \frac{1}{G} \end{pmatrix} \quad (\text{Eq. 8-3})$$

where  $E$  is the elastic modulus,  $G$  is the shear modulus, and  $\nu$  is the Poisson's ratio of the material. There are two independent elastic constants in an isotropic material (any two of:  $E$ ,  $\nu$ , and  $G$ , where  $G = E/[2(1 + \nu)]$ ).

### Transverse Isotropy

Transverse isotropy exists when a material exhibits isotropy in one material plane. An example of a transversely isotropic material is a fiber reinforced composite with uni-directional fibers. The plane that cuts across the fibers is the transverse plane. The compliance matrix for a transversely isotropic material is as follows:

$$[c]^{-1} = [s] = \begin{pmatrix} \frac{1}{E_L} & -\frac{\nu_L}{E_T} & -\frac{\nu_L}{E_T} & 0 & 0 & 0 \\ -\frac{\nu_L}{E_L} & \frac{1}{E_T} & -\frac{\nu_T}{E_T} & 0 & 0 & 0 \\ -\frac{\nu_L}{E_L} & -\frac{\nu_T}{E_T} & \frac{1}{E_T} & 0 & 0 & 0 \\ 0 & 0 & 0 & \frac{2(1+\nu_T)}{E_T} & 0 & 0 \\ 0 & 0 & 0 & 0 & \frac{1}{G_L} & 0 \\ 0 & 0 & 0 & 0 & 0 & \frac{1}{G_L} \end{pmatrix} \quad (\text{Eq. 8-4})$$

where  $E_T$  is the elastic modulus in the transverse plane,  $E_L$  is the elastic modulus normal to the transverse plane,  $G_L$  is the shear modulus in the direction normal to the transverse plane,  $\nu_T$  is the Poisson's ratio in the transverse plane, and  $\nu_L$  is the Poisson's ratio normal to the transverse plane of the material. There are 5 independent elastic constants in a transversely isotropic material ( $E_T$ ,  $E_L$ ,  $\nu_T$ ,  $\nu_L$ , and  $G_L$ ).

### Orthotropy

Orthotropy is generally the least symmetry used to describe bone in the literature. Orthotropy implies that material properties vary in three orthogonal directions (i.e., three orthogonal planes of material symmetry exist in an orthotropic material). The compliance matrix for orthotropic materials is as follows:

$$[c]^{-1} = [s] = \begin{pmatrix} \frac{1}{E_1} & -\frac{\nu_{21}}{E_2} & -\frac{\nu_{31}}{E_3} & 0 & 0 & 0 \\ -\frac{\nu_{12}}{E_1} & \frac{1}{E_2} & -\frac{\nu_{32}}{E_3} & 0 & 0 & 0 \\ -\frac{\nu_{13}}{E_1} & -\frac{\nu_{23}}{E_2} & \frac{1}{E_3} & 0 & 0 & 0 \\ 0 & 0 & 0 & \frac{1}{G_{23}} & 0 & 0 \\ 0 & 0 & 0 & 0 & \frac{1}{G_{31}} & 0 \\ 0 & 0 & 0 & 0 & 0 & \frac{1}{G_{12}} \end{pmatrix} \quad (\text{Eq. 8-5})$$

where indices 1, 2, and 3 represent three primary orthogonal directions. There are 9 independent elastic constants in an orthotropic material ( $E_1, E_2, E_3, \nu_{12}, \nu_{13}, \nu_{23}, G_{12}, G_{13}, G_{23}$ ). Note that

$$G_{ij} = G_{ji} \text{ and } \frac{\nu_{ij}}{E_i} = \frac{\nu_{ji}}{E_j} \text{ for } i \neq j = 1, 2, 3 \text{ due to symmetry of the material and the elastic constants}$$

matrix.

### Anisotropy

Anisotropic materials respond differently to loads applied in all directions. A fully anisotropic material has a fully populated elastic constants matrix (Equation 8-6). The 36 coefficients reduce to 21 independent elastic constants due to symmetry of the elastic constants matrix.

$$[s] = \begin{pmatrix} s_{11} & s_{12} & s_{13} & s_{14} & s_{15} & s_{16} \\ s_{21} & s_{22} & s_{23} & s_{24} & s_{25} & s_{26} \\ s_{31} & s_{32} & s_{33} & s_{34} & s_{35} & s_{36} \\ s_{41} & s_{42} & s_{43} & s_{44} & s_{45} & s_{46} \\ s_{51} & s_{52} & s_{53} & s_{54} & s_{55} & s_{56} \\ s_{61} & s_{62} & s_{63} & s_{64} & s_{65} & s_{66} \end{pmatrix} \quad (\text{Eq. 8-6})$$

## **Transformations in Anisotropic Materials**

Lekhnitskii (1968) is well referenced for his work in the area of transforming stresses and strains from material to specimen coordinates and vice versa when the two coordinate systems do not align with one another. An analysis of a specimen with its loading axis rotated away from its principal material direction requires a transformation of the elastic constants matrix (see Example 8-2). Given the compliance matrix for the principal material directions and strains in a specimen loaded in a non-principal direction, the compliance matrix can be transformed to predict the experimental strains if an appropriate material model is selected for Hooke's law. For example, if a material is orthotropic, we should be able to apply orthotropic Hooke's law to predict strains in off-axis specimens (i.e., specimens not aligned along principal material axes). Our analysis uses this technique to determine the material symmetry of manatee rib bone. Example 8-3 demonstrates the use of the transformed compliance matrix for the calculation of strains in a specimen loaded along a non-principal direction.

## **Thermodynamic Restrictions on Elastic Constants**

There are two requirements that must be met in order to ensure that thermodynamic restrictions imposed on elastic materials are satisfied (Cowin, 2002). The physical significance of these requirements is that the work done on an elastic material must be positive (e.g., tensile loads produce positive extension and hydrostatic compression will not result in expansion of the material) (Bertholet, J., 1999). The requirements are presented below in equation form. These equations will be used to verify the validity of experimentally determined elastic constants.

### **Requirement 1**

The stiffness and compliance matrices must be positive:

$$S_{11}, S_{22}, S_{33}, S_{44}, S_{55}, S_{66} > 0,$$

$$\begin{vmatrix} s_{11} & s_{12} \\ s_{12} & s_{22} \end{vmatrix} > 0, \begin{vmatrix} s_{22} & s_{23} \\ s_{23} & s_{33} \end{vmatrix} > 0, \begin{vmatrix} s_{11} & s_{13} \\ s_{13} & s_{33} \end{vmatrix} > 0,$$

and

$$\begin{vmatrix} s_{11} & s_{12} & s_{13} \\ s_{12} & s_{22} & s_{23} \\ s_{13} & s_{23} & s_{33} \end{vmatrix} > 0 \quad (\text{Eq. 8-7})$$

## Requirement 2

The following conditions for the components of the stiffness matrix must be satisfied:

$$E_1, E_2, E_3, G_{23}, G_{31}, G_{12} > 0,$$

$$(1 - \nu_{23}\nu_{32}), (1 - \nu_{13}\nu_{31}), (1 - \nu_{12}\nu_{21}) > 0,$$

and

$$1 - \nu_{12}\nu_{21} - \nu_{23}\nu_{32} - \nu_{31}\nu_{13} - 2\nu_{21}\nu_{32}\nu_{13} > 0. \quad (\text{Eq. 8-8})$$

## Tensile Testing

Manatee rib bones were obtained under US Fish and Wildlife permit #MA067116-0 issued to the Florida Fish and Wildlife Conservation Commission's (FWC) Marine Mammal Pathology Lab (MMPL). Use of the tissue was governed by University of Florida Institutional Animal Care and Use Committee (IACUC) protocol #E407. Ribs from the center of several adult manatees (numbers 9-10 of 17-19 ribs) were selected for this study. The manatee rib was stored with flesh intact to preserve material properties (An and Draughn, 2000) at -20° Celsius. Specimens were prepared from the middle third of the selected ribs to conform to testing procedures outlined in Chapters 6 and 7, thus reducing variability associated with site-specific material properties. Dog-bone shaped specimens with a square cross-section were machined to the following dimensions using a vertical end mill: length = 38 mm, width = 12.7 mm, gage length = 19 mm, gage width =

6.4 mm, radius at gage section = 3.2 mm. Four to ten specimens were prepared in each of the [110], [101], and [011] directions (Figure 8-1). The harvest angles for off-axis specimens were measured and found to be within 15° of their target angle of 45° off-axis from the principal axes in each principal plane. All machining was done under constant irrigation with water to prevent over-heating. Specimens were wrapped in gauze, soaked in saline solution, and refrigerated for up to 1 week prior to testing. Specimens were wet when they were loaded to ~1100 N at a rate of 1 mm/min at room temperature with a uniaxial loading machine (MTI 30K, Measurement Technology, Inc., Roswell, GA). The load level was selected from within the linear range of the material based on results from a pilot study in which several air-dried specimens from each presumed primary orientation were loaded to failure (Chapter 5). Loads were recorded for each specimen from readings taken by a 1000-lb load cell (Interface SM-1000-38, Scottsdale, AZ). Strains were acquired using visual (digital) image correlation (VIC) (Figure 8-2). Strains measured by VIC are considered valid between 500  $\mu\epsilon$  and 500% when using VIC3D software (VIC-3D Digital Image Correlation v.2006.0.0, Correlated Solutions, Inc., West Columbia, SC). In the current analysis, Poisson (lateral) strains fell below the 500  $\mu\epsilon$  level, so normal strains (ranging from three to ten times Poisson strains) were used for comparison in the orthotropic verification analysis.

### **Material Symmetry Analysis**

In the prerequisite studies (Chapters 6 and 7), manatee rib shear and tensile properties were measured along the major and minor axes of the transverse cross section and along the longitudinal direction of the rib bone (Table 8-1), thus completing the constitutive matrix relating stresses to strains for this presumably orthotropic material. The constitutive matrix can now be transformed into any coordinate system desired. In our analysis, three sets of coordinate system

transformations were performed, consisting of a 45° rotation about each of the presumed principal axes within the principal planes to correspond to the experimental specimens. The rotation was done for each of three material models (isotropic, transversely isotropic, and orthotropic) in order to demonstrate which model best predicts experimentally measured strains. A 500-N load was selected for implementation into the Hooke's law models, since most of the experimental data contained strain data for this load level. The material model yielding the lowest error when comparing predicted strains to experimental strains is the material model of choice for future analyses involving the manatee rib bone. If none of the models reasonably predict experimental strains, two potential conclusions could be drawn: 1) the material is of lesser symmetry than orthotropic, or 2) the axes selected for the original material property collection studies (Chapters 6 and 7) are not the principal material axes. To test the whether manatee rib bone material properties exhibit less than orthotropic symmetry, additional experiments would be required in a number sufficient to complete the elastic constants matrix for whichever material model is being tested. To determine if additional testing is necessary, an error tolerance was chosen for our predicted strains to be plus or minus one standard deviation (*SD*) from the mean experimental strain. Predicted strains within one *SD* of the mean suggest that the material model yielding this result is a probable material symmetry for manatee rib bone.

## **Results**

Table 8-1 shows the results from Chapters 6 and 7 including nine independent elastic constants, their standard deviations, and the number of specimens used to calculate each. The values found in Chapters 6 and 7 satisfy thermodynamic restrictions listed in Equations 8-7 and 8-8. Table 8-2 shows the results from the off-axis Hooke's law tests for various material models. Table 8-3 shows the measured normal strain values (mean  $\pm$  *SD*) for specimens loaded in each off-axis direction. Table 8-4 shows the percent error associated with each material model when

comparing results to those obtained experimentally. It was found that the orthotropic model produced strains within one standard deviation from the mean for each orientation tested experimentally, while the transversely isotropic model was within one standard deviation from the mean for two of the three orientations, and the isotropic model only produced strains within one standard deviation of the mean for one orientation. Although the transversely isotropic model predicted strains quite well, it did not meet the criteria defined in this paper for selection as the material symmetry model for manatee rib bone. The only model to meet the criteria was the orthotropic model. It is therefore concluded that manatee rib bone material properties are orthotropic.

Material property plots for this orthotropic material take the form of an ellipsoid with vertices equal in magnitude to the material properties measured about each respective principal axis (Figure 8-3). The amount of deviation from a spherical shape is proportional to the value of the anisotropic ratios between material axes.

### **Discussion**

Manatee rib material properties were previously measured only about the longitudinal axis of the bone (Yan, 2002; Clifton, 2005; Yan 2006a, b, 2007). Chapters 6 and 7 were used to expand the dataset for this material by obtaining nine independent elastic constants of manatee rib bone under the assumption that the material is orthotropic. The analysis presented in this study was used to quantify the error in modeling bone using orthotropic Hooke's law for off-axis specimens (i.e., specimens aligned in non-principal directions). Relatively few tests were required to determine which symmetry (orthotropy or greater) exists or if symmetry is less than orthotropic: Three presumed principal directions are tested to generate the orthotropic compliance matrix and at least one off-axis direction is experimentally tested for comparison to strain predictions from Hooke's law. A limitation of the present method is that it is incapable of

distinguishing between lesser symmetries than assumed in the experimental analysis. Therefore, the least symmetry expected for the material should be assumed for the experimental component of the analysis. The distinction between greater symmetries is only possible if testing those particular symmetry models using Hooke's law. In Chapter 6, tensile properties were found to significantly vary in all three directions, thus orthotropy is the least symmetry possible for manatee rib bone. Our present analysis demonstrated that models with greater symmetry than orthotropic did not produce strains within allowable tolerances as defined in this chapter for selection as the material symmetry model for manatee rib bone. Furthermore, our analysis confirms the finding that manatee rib bone is orthotropic by showing that error criteria were met and this model is valid for the material. Although we chose to apply our analysis technique to verify the material symmetry of manatee rib bone, the technique could be applied to any material exhibiting linear-elastic behavior.

Table 8-1. Mean tensile and shear properties of manatee rib bone (from Chapters 6 and 7, respectively) used in the Hooke's law analyses. Components selected for each of the material models (e.g., orthotropic, transversely isotropic, and isotropic) are also provided. Standard deviations (*SD*) are presented along with the number of specimens used to obtain each constant (*n*).

Property	Elastic moduli (GPa)			Major Poisson's ratios			Shear moduli (GPa)		
	$E_1, E_L, E$	$E_2$	$E_3, E_T$	$\nu_{12}$	$\nu_{13}, \nu_L$	$\nu_{23}, \nu_T, \nu$	$G_{12}$	$G_{13}, G_L$	$G_{23}, G_T, G$
<i>Mean</i>	16.9	8.4	5.9	0.27	0.25	0.25	4.0	4.1	2.7
<i>SD</i>	1.5	1.2	2.2	0.04	0.04	0.04	0.8	0.4	0.4
<i>n</i>	13	13	13	13	13	11	3	9	5

Table 8-2. Predicted strain as a function of orientation and material model. The strains were obtained by rotating the compliance matrix for various material models (isotropic, transversely isotropic, and orthotropic) to conform to off-axis specimen orientations ([110], [101], and [011]) and applying a 500 N load using Hooke's law.

Orientation	Predicted strain (Hooke's law)		
	Isotropic	Transversely isotropic	Orthotropic
[110]	0.00142	0.00129	0.00122
[101]	0.00142	0.00129	0.00137
[011]	0.00142	0.00210	0.00186

Table 8-3. Strain measured by visual image correlation. Values are provided as a function of specimen orientation for off-axis specimens ([110], [101], and [011]) with an applied load level of 500 N.

Orientation	Measured strain (visual image correlation)		
	Mean	<i>SD</i>	<i>n</i>
[110]	0.00126	0.00019	6*
[101]	0.00121	0.00018	5**
[011]	0.00187	0.00020	6

\*Results from four outlier specimens were removed from the mean and *SD* calculations

\*\*Results from three outlier specimens were removed from the mean and *SD* calculations

Table 8-4. Error in Hooke's law predicted strains as a function of orientation and material model. Percent error was calculated as  $(\epsilon_{\text{measured}} - \epsilon_{\text{predicted}}) / \epsilon_{\text{measured}} * 100\%$ .

Orientation	Percent error in Hooke's law predicted strain		
	Isotropic	Transversely isotropic	Orthotropic
[110]	-13%	-2%	3%
[101]	-17%	-7%	-13%
[011]	24%	-12%	1%

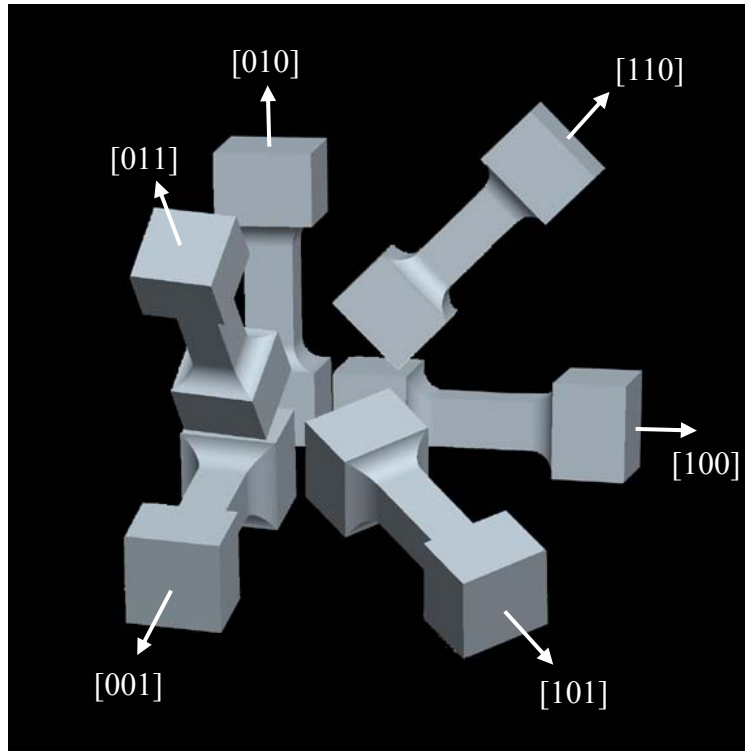


Figure 8-1. Specimen orientations used in the present analysis.

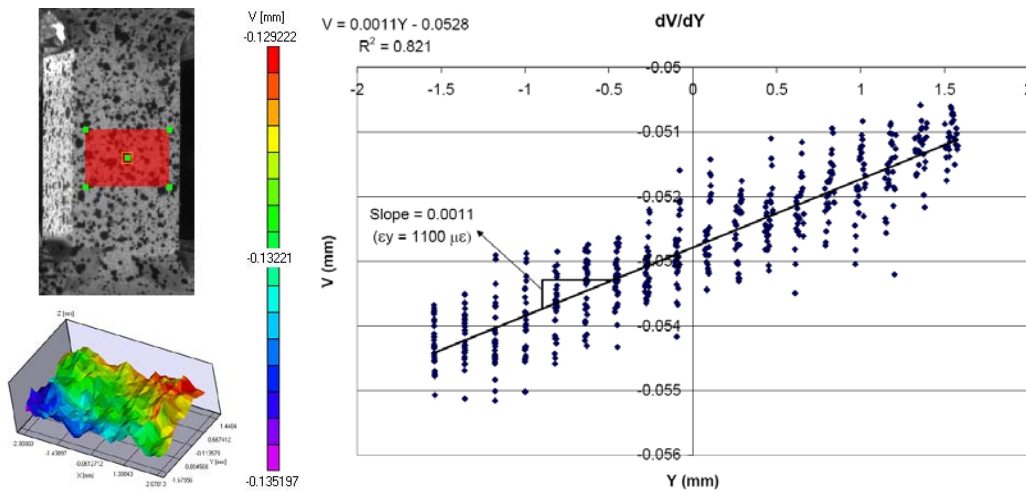
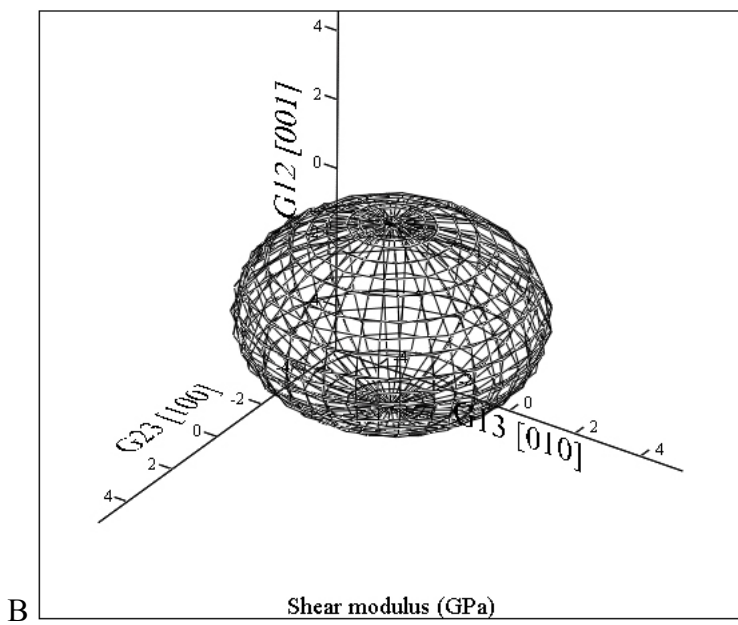
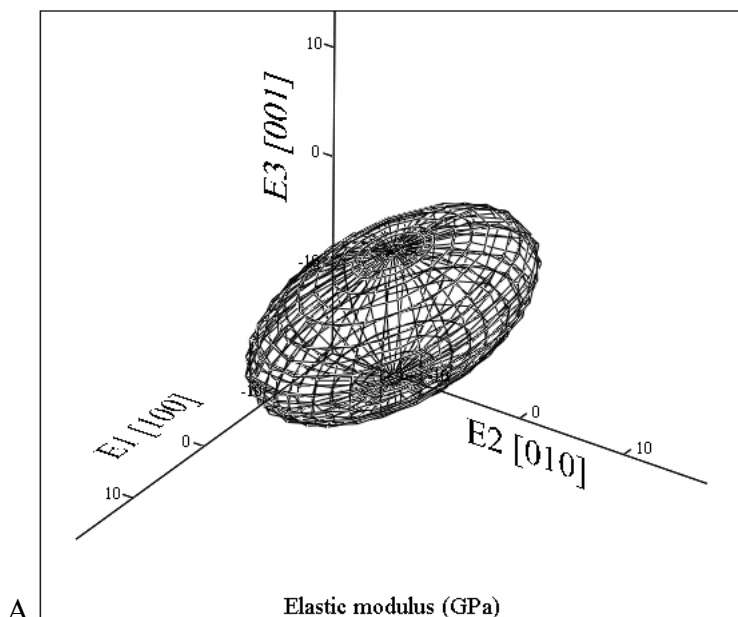


Figure 8-2. Typical vertical position versus vertical deformation ( $dV/dY$ ) curve (right) showing data points from the gage section of a manatee rib bone tensile specimen (upper left). The data points were generated using visual image correlation. The normal strain (slope of the curve) is  $1100 \mu\epsilon$  for this particular specimen and load step. A linear trend line fits the data reasonably well ( $R^2=0.821$ ), hence the strain distribution along the gage length of the specimen is fairly uniform. Inhomogeneities, if present, would cause there to be a non-uniform strain distribution noted by a change in slope of the  $dV/dY$  curve. The 3D plot (lower left) maps the contour of the vertical deformations ( $V$ ) onto the specimen surface. Values of  $V$  vary from  $-0.129$  (red) to  $-0.135$  mm (purple).



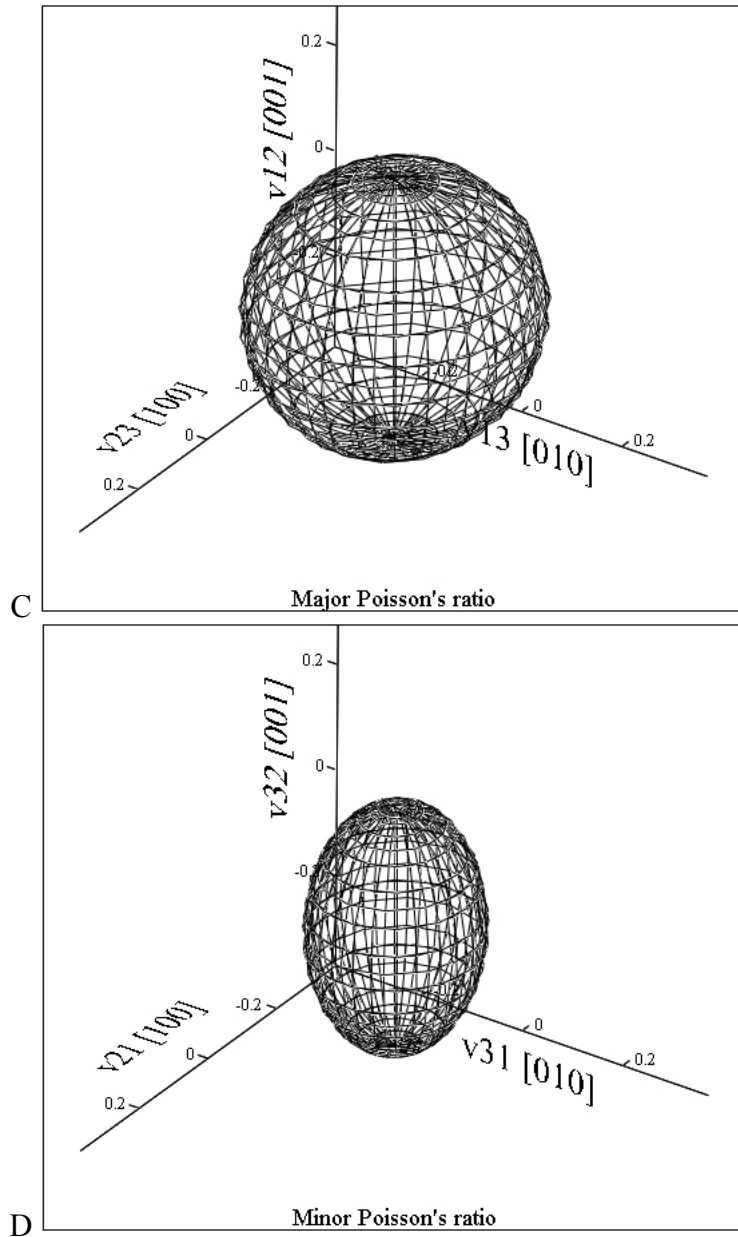
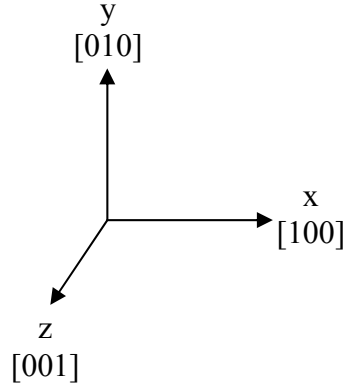


Figure 8-3. Surface plots showing the variation in material properties with material axes: A) elastic modulus, B) shear modulus, C) major Poisson's ratio, D) minor Poisson's ratio. The values used to generate the minor Poisson's ratio plot are listed in Chapter 6. The surface plot for an orthotropic material is an ellipsoid, whereas an isotropic material forms a sphere. Note that the material property axes coincide with the principal material directions. That is, for example,  $E_1$ ,  $E_2$ , and  $E_3$  coincide with the  $[100]$ ,  $[010]$ , and  $[001]$  material directions, respectively.

**Example 8-1.**

Calculate the elastic modulus and Poisson's ratio for the following scenario:

Strains have been recorded on the surface of a specimen using a biaxial strain gage. Foil orientations correspond to the loading axis direction [010] and the direction perpendicular to the loading axis [100]. Assume the material is orthotropic. Provide your response in variable form.



**Solution**

Orthotropic Hooke's law relates the stresses to the strains using the following relationship:

$$\begin{bmatrix} \varepsilon_1 \\ \varepsilon_2 \\ \varepsilon_3 \\ \gamma_{23} \\ \gamma_{31} \\ \gamma_{12} \end{bmatrix} = \begin{pmatrix} \frac{\sigma_1}{E_1} & -\sigma_2 \cdot \frac{\nu_{21}}{E_2} & -\sigma_3 \cdot \frac{\nu_{31}}{E_3} & 0 & 0 & 0 \\ -\sigma_1 \cdot \frac{\nu_{12}}{E_1} & \frac{\sigma_2}{E_2} & -\sigma_3 \cdot \frac{\nu_{32}}{E_3} & 0 & 0 & 0 \\ -\sigma_1 \cdot \frac{\nu_{13}}{E_1} & -\sigma_2 \cdot \frac{\nu_{23}}{E_2} & \frac{\sigma_3}{E_3} & 0 & 0 & 0 \\ 0 & 0 & 0 & \frac{\sigma_{23}}{G_{23}} & 0 & 0 \\ 0 & 0 & 0 & 0 & \frac{\sigma_{31}}{G_{31}} & 0 \\ 0 & 0 & 0 & 0 & 0 & \frac{\sigma_{12}}{G_{12}} \end{pmatrix} \tag{Eq. 8-9}$$

where  $\gamma_{ij} = \varepsilon_{ij} + \varepsilon_{ji} = 2 \cdot \varepsilon_{ij}$  for  $i \neq j = 1, 2, 3$ .

The load is applied in the [010] material direction, thus the only component of stress acting on the system is  $\sigma_2$ , which is calculated by dividing applied load by the cross-sectional area of the specimen gage section.

Break Equation 8-9 into 6 equations.

$$\begin{aligned}\varepsilon_1 &= \frac{\sigma_1}{E_1} - \sigma_2 \cdot \frac{\nu_{21}}{E_2} - \sigma_3 \cdot \frac{\nu_{31}}{E_3} \\ \varepsilon_2 &= -\sigma_1 \cdot \frac{\nu_{12}}{E_1} + \frac{\sigma_2}{E_2} - \sigma_3 \cdot \frac{\nu_{32}}{E_3} \\ \varepsilon_3 &= -\sigma_1 \cdot \frac{\nu_{13}}{E_1} - \sigma_2 \cdot \frac{\nu_{23}}{E_2} + \frac{\sigma_3}{E_3} \\ \gamma_{23} &= \frac{\sigma_{23}}{G_{23}} \\ \gamma_{31} &= \frac{\sigma_{31}}{G_{31}} \\ \gamma_{12} &= \frac{\sigma_{12}}{G_{12}}\end{aligned}\tag{Eq. 8-10}$$

Because  $\sigma_2$  is the only applied stress, set all other stresses equal to 0. Also note that  $\varepsilon_3$  was not measured and should therefore be excluded from further calculations.

$$\begin{aligned}\varepsilon_1 &= -\sigma_2 \cdot \frac{\nu_{21}}{E_2} \\ \varepsilon_2 &= \frac{\sigma_2}{E_2}\end{aligned}\tag{Eq. 8-11}$$

Solve for  $E_2$  and  $\nu_{12}$ .

$$\boxed{E_2 = \sigma_2 / \varepsilon_2}$$

$$\boxed{\nu_{12} = -\varepsilon_1 / \varepsilon_2}$$

### Example 8-2

Calculate the compliance matrix,  $[s]$ , for a tensile specimen oriented in the  $[110]$  material direction assuming the specimen underwent in-plane rotation about the  $[001]$  material coordinate system axis.

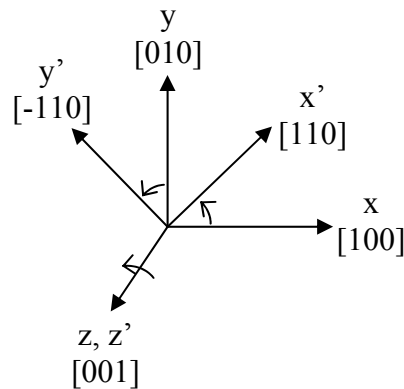


Figure 8-5. Rotation of the material coordinates to specimen coordinates for a specimen lying in the  $[110]$  material direction.

Given:

$$[s] = \begin{pmatrix} 0.063 & -0.016 & -0.015 & 0 & 0 & 0 \\ -0.016 & 0.042 & -0.012 & 0 & 0 & 0 \\ -0.015 & -0.012 & 0.059 & 0 & 0 & 0 \\ 0 & 0 & 0 & 0.143 & 0 & 0 \\ 0 & 0 & 0 & 0 & 0.152 & 0 \\ 0 & 0 & 0 & 0 & 0 & 0.144 \end{pmatrix} [GPa^{-1}]$$

### Solution

Define the specimen coordinates in the material coordinate system.

$$\begin{aligned}
[X' \text{ axis}] &\rightarrow [110] \rightarrow L_{11} = 1, L_{12} = 1, L_{13} = 0 \\
[Y' \text{ axis}] &\rightarrow [-110] \rightarrow L_{21} = -1, L_{22} = 1, L_{23} = 0 \\
[Z' \text{ axis}] &\rightarrow [001] \rightarrow L_{31} = 0, L_{32} = 0, L_{33} = 1
\end{aligned}$$

Solve for the direction cosines matrix  $a_{ij}$ .

$$\begin{aligned}
\alpha_1 &= \frac{L_{11}}{\sqrt{L_{11}^2 + L_{12}^2 + L_{13}^2}}, \beta_1 = \frac{L_{11}}{\sqrt{L_{11}^2 + L_{12}^2 + L_{13}^2}}, \gamma_1 = \frac{L_{11}}{\sqrt{L_{11}^2 + L_{12}^2 + L_{13}^2}} \\
\alpha_2 &= \frac{L_{21}}{\sqrt{L_{21}^2 + L_{22}^2 + L_{23}^2}}, \beta_2 = \frac{L_{22}}{\sqrt{L_{21}^2 + L_{22}^2 + L_{23}^2}}, \gamma_2 = \frac{L_{23}}{\sqrt{L_{21}^2 + L_{22}^2 + L_{23}^2}} \\
\alpha_3 &= \frac{L_{31}}{\sqrt{L_{31}^2 + L_{32}^2 + L_{33}^2}}, \beta_3 = \frac{L_{32}}{\sqrt{L_{31}^2 + L_{32}^2 + L_{33}^2}}, \gamma_3 = \frac{L_{33}}{\sqrt{L_{31}^2 + L_{32}^2 + L_{33}^2}}
\end{aligned} \tag{Eq. 8-12}$$

$$[a] = \begin{bmatrix} \alpha_1 & \beta_1 & \gamma_1 \\ \alpha_2 & \beta_2 & \gamma_2 \\ \alpha_3 & \beta_3 & \gamma_3 \end{bmatrix} = \begin{bmatrix} 0.707 & 0.707 & 0 \\ -0.707 & 0.707 & 0 \\ 0 & 0 & 1 \end{bmatrix}$$

Input the components of the direction cosines matrix into the Q-matrix.

$$[Q] = \begin{bmatrix} \alpha_1^2 & \alpha_2^2 & \alpha_3^2 & 2 \cdot \alpha_2 \cdot \alpha_3 & 2 \cdot \alpha_3 \cdot \alpha_1 & 2 \cdot \alpha_1 \cdot \alpha_2 \\ \beta_1^2 & \beta_2^2 & \beta_3^2 & 2 \cdot \beta_2 \cdot \beta_3 & 2 \cdot \beta_3 \cdot \beta_1 & 2 \cdot \beta_1 \cdot \beta_2 \\ \gamma_1^2 & \gamma_2^2 & \gamma_3^2 & 2 \cdot \gamma_2 \cdot \gamma_3 & 2 \cdot \gamma_3 \cdot \gamma_1 & 2 \cdot \gamma_1 \cdot \gamma_2 \\ \beta_1 \cdot \gamma_1 & \beta_2 \cdot \gamma_2 & \beta_3 \cdot \gamma_3 & \beta_2 \cdot \gamma_3 + \beta_3 \cdot \gamma_2 & \beta_1 \cdot \gamma_3 + \beta_3 \cdot \gamma_1 & \beta_1 \cdot \gamma_2 + \beta_2 \cdot \gamma_1 \\ \lambda_1 \cdot \alpha_1 & \lambda_2 \cdot \alpha_2 & \lambda_3 \cdot \alpha_3 & \gamma_2 \cdot \alpha_3 + \gamma_3 \cdot \alpha_2 & \gamma_1 \cdot \alpha_3 + \gamma_3 \cdot \alpha_1 & \gamma_1 \cdot \alpha_2 + \gamma_2 \cdot \alpha_1 \\ \alpha_1 \cdot \beta_1 & \alpha_2 \cdot \beta_2 & \alpha_3 \cdot \beta_3 & \alpha_2 \cdot \beta_3 + \alpha_3 \cdot \beta_2 & \alpha_1 \cdot \beta_3 + \alpha_3 \cdot \beta_1 & \alpha_1 \cdot \beta_2 + \alpha_2 \cdot \beta_1 \end{bmatrix} \tag{Eq. 8-13}$$

Compute the compliance matrix in terms of the specimen orientation

$$[s'] = [Q]^T [s] [Q] \tag{Eq. 8-14}$$

$$[s'] = \begin{pmatrix} 0.054 & -0.018 & -0.014 & 0 & 0 & -0.01 \\ -0.018 & 0.054 & -0.014 & 0 & 0 & -0.01 \\ -0.014 & -0.014 & 0.059 & 0 & 0 & 0.003 \\ 0 & 0 & 0 & 0.147 & -0.0045 & 0 \\ 0 & 0 & 0 & -0.0045 & 0.147 & 0 \\ -0.011 & -0.011 & 0.003 & 0 & 0 & 0.137 \end{pmatrix} [GPa^{-1}]$$

### Example 8-3

Calculate the stresses and strains in a specimen when it is loaded in the [110] orientation (Figure 8-5), reporting values in both specimen and material coordinate systems. Use the compliance matrix from Example 8-2. Note that the values from the compliance matrix correspond to units of GigaPascals (GPa). Assume an applied stress along the specimen [100] axis (which corresponds to the material [110] axis) of 0.1 GPa. Note that an apostrophe after a variable signifies that the values for that variable are reported in specimen rather than material coordinates.

Given:

$$\sigma' = \begin{bmatrix} \sigma_1' \\ \sigma_2' \\ \sigma_3' \\ \sigma_{23}' \\ \sigma_{31}' \\ \sigma_{12}' \end{bmatrix} = \begin{bmatrix} 0.1 \\ 0 \\ 0 \\ 0 \\ 0 \\ 0 \end{bmatrix} [GPa]$$

Solve for the stresses in the material coordinate system.

$$[\sigma] = [Q]^{-1} [\sigma']$$

$$\sigma = \begin{bmatrix} \sigma_1 \\ \sigma_2 \\ \sigma_3 \\ \sigma_{23} \\ \sigma_{31} \\ \sigma_{12} \end{bmatrix} = \begin{bmatrix} 0.05 \\ 0.05 \\ 0 \\ 0 \\ 0 \\ 0.05 \end{bmatrix} \quad [GPa]$$

Solve for the strains in the material coordinate system.

$$[\varepsilon] = [s][\sigma]$$

$$\varepsilon = \begin{bmatrix} \varepsilon_1 \\ \varepsilon_2 \\ \varepsilon_3 \\ \gamma_{23} \\ \gamma_{31} \\ \gamma_{12} \end{bmatrix} = \begin{bmatrix} 0.00235 \\ 0.00130 \\ -0.00135 \\ 0 \\ 0 \\ 0.00720 \end{bmatrix}$$

Solve for the strains in the specimen coordinate system.

$$[\varepsilon'] = [Q]^T [\varepsilon] [Q]$$

$$\varepsilon' = \begin{bmatrix} \varepsilon_1' \\ \varepsilon_2' \\ \varepsilon_3' \\ \gamma_{23}' \\ \gamma_{31}' \\ \gamma_{12}' \end{bmatrix} = \begin{bmatrix} 0.00543 \\ -0.00178 \\ -0.00135 \\ 0 \\ 0 \\ -0.00105 \end{bmatrix}$$

CHAPTER 9  
ANISOTROPIC FRACTURE PROPERTIES OF MANATEE RIB (CORTICAL) BONE: A  
NUMERICAL AND EXPERIMENTAL INVESTIGATION

**Short Summary**

The fracture toughness of manatee rib (cortical) bone was found using a finite element (FE) model incorporating an anisotropic stress intensity factor formulation. Experiments were performed on six to twelve notched double-edge crack tensile (wet) bone specimens for each of six crack orientations in order to obtain fracture parameters used in the FE model. The specimens were loaded to failure at room temperature at 1 mm/min. Tensile loading in the longitudinal direction with cracks propagated in the out-of-plane transverse direction resulted in the greatest fracture toughness ( $K_{IC}^{13}$ ), while specimens loaded in the out-of-plane transverse direction with cracks propagated in the in-plane transverse direction had the lowest fracture toughness ( $K_{IC}^{32}$ ), where superscript 1 represents the proximodistal (longitudinal) axis, 2 denotes the superficial-deep (in-plane transverse) axis, and 3 denotes the craniocaudal (out-of-plane transverse) axis in anatomic coordinates. Anisotropy was extremely significant in this study given the ~4-fold difference between the maximum and minimum fracture toughness values of various orientations. The numerical tests resulted in fracture toughness values of [ $K_{IC}^{12}$   $K_{IC}^{13}$   $K_{IC}^{23}$   $K_{IC}^{21}$   $K_{IC}^{31}$   $K_{IC}^{32}$ ]= [3.2 3.4 1.0 1.1 1.0 0.8] MPa√m. Results from traditional, isotropic-based experimental calculations ( $[K_{IC}^{12}$   $K_{IC}^{13}$   $K_{IC}^{23}$   $K_{IC}^{21}$   $K_{IC}^{31}$   $K_{IC}^{32}]$ =[3.2 3.2 0.9 1.1 0.9 0.7] MPa√m) agreed well with those from the numerical analysis. The procedures used in the present analysis can be used as a template for further cortical bone fracture studies that aim to discern a broader spectrum of fracture resistance values by combining numerical simulation with experimental fracture parameters.

## Introduction

A substantial body of literature exists on the fracture mechanics of human and bovine bone. The bulk of the literature is confined to reports of fracture properties for a single mode of fracture for one orientation of bone (Cooke et al., 1973; Pope and Murphy, 1974; Wright and Hayes, 1976; Wright and Hayes, 1977; Alto and Pope, 1979; Behiri and Bonfield, 1980; 1984; Moyle and Gavens, 1986; Norman et al., 1995; Zioupos and Currey, 1998; Yeni and Norman, 2000). Most of the existing literature neglects the anisotropic nature of bone, and hence, valuable information on orientation-dependent fracture properties is not always presented. There exists only a small body of literature that investigates the fracture properties of cortical bone as a function of material orientation (Bonfield, et al., 1985; Bonfield, 1987; Behiri and Bonfield, 1989; Wang and Agrawal, 1996; Hoffmeister et al., 2000; Lucksanambool et al., 2001; Nalla et al., 2005b). None of these studies, however, report the six values of fracture toughness necessary to fully describe the fracture properties of an orthotropic material (Schachner et al., 2000) such as bone. In addition, all of the studies to date have used experimental calculations valid only for isotropic materials (Stanzl-Tschegg et al., 1995). Yan (2002) modeled manatee rib bone with isotropic material properties using 3-D finite element analysis (FEA) in order to determine how an entire rib behaves in response to transverse loading. Paruchuru et al. (2002) modeled bone as a 2-D, isotropic material using FEA to determine the fracture toughness of small cortical bone specimens. Norman et al. (1992) modeled cortical bone fracture using 2-D FEA to compare several fracture property formulations. Groteenboer and Weersink (1982) used a 2-D model for single-edge notched specimens of human cortical bone. None of these models accounted for the effects of anisotropy in 3-dimensions, and hence the models are unable to cope with the 3-D stresses generated by material anisotropy (Arakere and Swanson, 2002; Arakere et al., 2005; Ranjan and Arakere, 2007; Knudsen and Arakere, 2006). In this study, an anisotropic stress

intensity factor (SIF) formulation was used in combination with experimentally determined anisotropic elastic constants and fracture parameters to determine the mode I (opening mode) critical SIF, or fracture toughness ( $K_{IC}$ ), for each of six crack orientations. To the best of the authors' knowledge, this is the first study to combine 3-D numerical simulation of cortical bone fracture using anisotropic stress intensity factor formulations and experiment to analyze the fracture behavior of manatee rib bone as a function of its orientation.

### **Materials and Methods**

Manatee rib bone is primary plexiform bone and does not contain a medullar canal. As such, larger specimens can be obtained from manatee rib bones than from bones of most other animals. Manatee rib bones were obtained under US Fish and Wildlife permit #MA067116-0 issued to the Florida Fish and Wildlife Conservation Commission's (FWC) Marine Mammal Pathology Lab (MMPL). Use of the tissue was governed by University of Florida Institutional Animal Care and Use Committee (IACUC) protocol #E407. Ribs from the center of several adult manatees (#s 9-10 of 17-19 ribs) were selected for this study (Figure 9-1). The manatee rib was stored with flesh intact to preserve material properties (An and Draughn, 2000) at -20° Celsius. The middle third of the selected rib was used for testing, since Yan (2002) found that the fracture properties of manatee rib bone vary from the middle of each rib to the ends of the bone. Close attention was paid to the orientation in which the specimens were cut from the middle third of the rib bone (Figure 9-2). Dog-bone shaped specimens with a square cross-section were machined to the following dimensions using a vertical end mill: length = 38 mm, width = 12.7 mm, gage length = 19 mm, gage width = 6.4 mm, radius at gage section = 3.2 mm. Notches were introduced on opposite sides of the specimens using a low speed wafering saw (Isomet low speed saw, Buehler Ltd., Lake Bluff, IL). All machining was done under constant irrigation with water to prevent over-heating. A v-notch (used in place of a pre-crack) was introduced at the notch tips

by pressing a sharp razor blade into the specimen (Yan, 2006b). Yan estimated the radius of the v-notches in his manatee rib bone specimens to be on the order of 1  $\mu\text{m}$  when using this same technique as applied in the present study. The resulting crack tip radius is governed by the material rather than the sharpness of the razor blade, since the razor blade effectively acts as a wedge that forces the material to crack to a characteristic notch radius specific to the material. Specimens were wrapped in gauze, soaked in saline solution, and refrigerated for up to 1 week prior to testing. Notch lengths were measured from digital photographs taken of the specimens prior to loading. The wet bone specimens were loaded to failure at a rate of 1 mm/min at room temperature with a uniaxial loading machine (MTI 30K, Measurement Technology, Inc., Roswell, GA). Failure load was recorded for each specimen from readings taken by a 1000-lb load cell (Interface SM-1000-38, Scottsdale, AZ). Failure loads and notch lengths were averaged for each specimen orientation and the coefficient of variation ( $CV$ ) was noted for each orientation ( $CV = \frac{SD}{\mu}$ , where  $SD$  is the standard deviation and  $\mu$  is the mean).

A three-dimensional model of the notched, double edge crack tensile specimen was generated using CAD software (Pro-Engineer Wildfire 3.0, Parametric Technology Corporation, Needham, MA). Notch lengths were the only varying parameter between the models for each specimen orientation. A v-notch (0.2 mm (Yan 2006b)) was introduced at the tip of the right notch before exporting the file in IGES format. The CAD models were imported into finite element software (ANSYS 10.0, ANSYS, Inc., Canonsburg, PA) for further analysis. Orthotropic material properties found during a prerequisite experimental study (chapters 6 and 7) were input into the finite element (FE) model ( $E_1=16.9$  GPa,  $E_2=8.4$  GPa,  $E_3=5.9$  GPa,  $\nu_{12}=0.27$ ,  $\nu_{13}=0.25$ ,  $\nu_{23}=0.25$ ,  $G_{12}=4.0$  GPa,  $G_{13}=4.1$  GPa,  $G_{23}=2.7$  GPa). A crucial step of the analysis was to implement direction cosines that transform the element coordinate system into material

coordinates. The material coordinates were verified by comparing numerical stress analysis results from an un-notched specimen of each orientation with analytical results. Next, a 2-dimensional finite element mesh was applied to an area of the specimen associated with the right notch, where concentrated key points were applied at the crack tip to generate quarter-point (singular) elements at that location. The 2-D mesh was swept through the thickness of the specimen using 20-node brick elements (solid 95). A free mesh (also constructed using 20-node brick elements) was generated for the rest of the model. Boundary conditions that closely resembled the physical constraints of the test fixture were applied to the appropriate nodes of the models along with experimentally-determined failure loads. Swenson and Ingraffea (1987; 1988a; 1988b) at the Cornell Fracture Group have developed FEA based fracture software: FRANC2D and FRANC3D. With an adaptive mesh technique, this fracture software can simulate crack growth without prescribing the crack path. Their work has provided fundamental understandings for the simulation of dynamic crack propagation based on FEA. We have adapted FRANC3D to compute anisotropic stress intensity factors for cortical bone specimens as a function of material orientation. The volume of the model associated with the left notch was exported to FRANC3D where an edge crack (0.2 mm (Yan 2006b)) was introduced at the tip of the notch. The volume was re-meshed by FRANC3D with 3-D 10-node tetrahedral elements (solid 92) and solid 95 elements. The re-meshed volume was re-inserted into ANSYS and the model was solved (Figure 9-3). The resulting nodal displacements were sent to FRANC3D for stress intensity factor (SIF) calculations. The SIFs were computed about the left crack tip according to the procedure outlined in the FRANC3D documentation (FRANC3D Concepts and Users Guide, 2003), which are elaborated upon in Knudsen (2006).

Experimental calculations were performed using theory for a double-edge crack plate in tension (Hertzberg, 1989) as a check for the numerical results. For plane strain,

$K_{IC} = C \cdot \sigma_c \cdot \sqrt{\pi \cdot a}$ , where  $\sigma_c$  is the measured failure stress,  $a$  is the measured crack length, and

$C$  is the geometry factor ( $C = \left(\frac{2w}{\pi a}\right)^{\frac{1}{2}} \cdot \left(\tan\left(\frac{\pi a}{2w}\right) + 0.1 \sin\left(\frac{\pi a}{w}\right)\right)^{\frac{1}{2}}$ , where  $w$  is the specimen (far

field) width). The effect of stress concentrations ( $k_t$ ) near the notch on crack-tip stresses were checked by comparing the following approximation to the v-notch (crack) length ( $a'$ ):

$$d \cong 0.13\sqrt{D \cdot r}, \quad (\text{Eq. 9-1})$$

where  $D$  is the notch length and  $r$  is the notch radius (Figure 9-3). The stress concentration factor should be included in the  $K_{IC}$  calculations ( $K_{IC} = k_t \cdot C \cdot \sigma_c \cdot \sqrt{\pi \cdot a}$ ) if  $a' > d$ . The yield stress of bovine (plexiform) cortical bone is 141 MPa (Martin et al., 1998), and was used to determine whether plain strain or plain stress conditions prevailed in the notched tensile specimens, since yield strength,  $\sigma_Y$ , of manatee bone was not investigated in our study. Plain strain prevails if the specimen thickness,  $B$ , is greater than or equal to the right side of Equation 9-2.

$$B \geq 2.5 \left( \frac{K_{IC}}{\sigma_Y} \right)^2 \quad (\text{Eq. 9-2})$$

A plastic zone is generated ahead of the crack tip in most materials. The plastic zone, if sufficiently large, affects the calculation of  $K_{IC}$ . The plastic zone radius is found according to Equation 9-3 for plain strain and plane stress conditions, respectively.

$$r_{Y\varepsilon} = \frac{1}{2\pi} \left( \frac{K_{IC}}{\sigma_Y} \right)^2$$

$$r_{Y\sigma} = \frac{1}{6\pi} \left( \frac{K_{IC}}{\sigma_Y} \right)^2 \quad (\text{Eq. 9-3})$$

In our study, the plastic zone is added to the crack length in the calculation of  $K_{IC}$  if the plastic zone radius exceeds 10% of the crack length.

Experimental results were obtained by performing calculations using two different averaging techniques. First, the average failure load and average critical crack length for each crack orientation were used in the experimental fracture toughness calculation in order to provide a direct comparison to computational results, which used the same input. Second, failure load and critical crack lengths were used to determine fracture toughness for each specimen and averaged for each crack orientation. The latter results provide a standard deviation for fracture toughness.

## Results

Fracture toughness values, crack lengths, and failure loads can be found in Table 9-1, while graphs of  $K_{IC}$  versus normalized crack front are provided in Figure 9-4. As can be seen, mode I SIFs are non-uniform across the crack front with lesser values being found at the surfaces than in the middle of the specimen. Fracture toughness was found to vary with specimen orientation with numerically evaluated values ranging from 0.8 to 3.4 MPa $\sqrt{m}$ . Cracks propagated in the transverse direction relative to the rib were most resistant to fracture with fracture toughness values on the order of 4-times that of specimens with longitudinally propagated cracks. In particular, specimens loaded in the proximodistal direction with cracks propagated in the craniocaudal direction resulted in the highest fracture toughness, while specimens loaded in the proximodistal direction with cracks propagated in the superficial-deep direction resulted in the lowest fracture toughness. Experimental calculation results were very similar to those from the numerical assessment, ranging from 0.9 to 3.2 MPa $\sqrt{m}$ .

According to Equation 9-1, the effect of the stress concentration at the notch was deemed negligible to the mode I SIF computed at the crack tip. According to Equation 9-2, plane strain

conditions prevailed in the notched specimens. From Equation 9-3, it was determined that the plastic zone radius should not be included in the  $K_{IC}$  calculations because the value was small relative to the crack lengths (<10%).

Computation time varied from fifteen to forty minutes for each model using a Dell Optiplex GX280 work station with a 3.4 GHz Pentium 4 processor and 1 GB of RAM. Models each contained approximately 120K nodes.

### Discussion

According to Akkus et al. (2004), anisotropy and inhomogeneity of bone tissue are the primary complications in modeling fracture behavior of bone. Both of these complications were accounted for in the present analysis. First, the SIF formulations utilized by the fracture analysis software are generalized for anisotropic materials. Next, the inhomogeneities of the specimens were assessed during the material property evaluation that preceded this study. A non-contact, full-field deformation analysis technique (Sutton et al., 1986; Sutton et al., 1991; Schreier et al., 2000; Lichtenberger and Schreier, 2002) was used to decipher position and deformation of every discretized point on the gage sections of tensile and shear specimens. Sudden changes in the strain magnitude are indicative of inhomogeneities in the specimen gage section. Strains were calculated as the slope of the change in position versus change in deformation curves

$(\epsilon_x = \frac{\partial u}{\partial x}; \epsilon_y = \frac{\partial v}{\partial y}; \gamma_{xy} = \frac{\partial u}{\partial y} + \frac{\partial v}{\partial x})$ , where  $\epsilon_x$ ,  $\epsilon_y$ , and  $\gamma_{xy}$  are the Poisson, normal, and shear

strains, respectively,  $x$ ,  $y$ , and  $z$  are the positions and  $u$ ,  $v$ , and  $w$  are the corresponding deformations in Cartesian coordinates. None of the specimens exhibited deviation from a linear slope (i.e., there were no changes in strain magnitude across the specimen gage sections).

Therefore it was concluded that, at the length scale of bone being studied here, inhomogeneities do not influence the apparent fracture toughness of the specimens.

Interpretation of results from experimental fracture toughness calculations is complicated by the small thickness available for most cortical bone (Akkus et al., 2004). This is because traditional fracture toughness calculations require an assumption of plane stress or strain, which is determined from Equation 9-2. Replacing the unknown yield stress of manatee bone with that of bovine cortical bone shows that plane strain conditions prevailed in the notched specimens. The anisotropic stress intensity factor formulation used in the numerical analysis did not require an assumption of plane stress or strain, thus some of the guess work for “border line” materials with a thickness that approaches the above inequality is removed when interpreting the results. Furthermore, yield stresses are not required as input to the numerical model. Because of the generalization of the SIF formulation used in this study to anisotropic materials of any thickness and the fact that experimental calculations use a geometry factor determined from isotropic materials, the numerical  $K_{IC}$  values were previously thought to be more accurate than those found from experimental calculations. To further support this perception, Stanzl-Tschegg (2006) commented on the inappropriateness of utilizing the experimental  $K_{IC}$  formulae for orthotropic materials. This is because the geometry factors used in  $K_{IC}$  formulae are the result of fitting numerical or photoelastic data to experimental data from an isotropic material (Raju and Newman, 1979). However, it was found in this study that the numerical fracture model results agreed quite well with experimental calculations of  $K_{IC}$ , thus suggesting the negligible effects of utilizing an isotropic-based geometry factor in the  $K_{IC}$  calculation.

The difference in  $K_{IC}$  between transverse and longitudinal orientations in this study is far larger than documented for other animals (Table 9-2). It appears that this difference is related to microstructural differences between specimen orientations (Figure 9-5). Manatee rib bone is mostly primary plexiform bone and contains very few osteons (Yan et al., 2006a). During

testing, sheets (or planes) of fibers bridged cracks in transversely loaded specimens as illustrated in Figure 9-6. Essentially, fracture in transversely loaded specimens occurred by “peeling” of fibrous sheets from one another. This would suggest that manatee rib bone tissue consists of layers of fibers oriented along the longitudinal axis of the bone.

Nalla et al. (2005b) found  $K_{IC}$  in human cortical bone to be between 51-140% greater for cracks propagated in the transverse direction relative to the rib than for cracks propagated in the longitudinal direction. The increase in toughness for cracks propagated in the transverse direction is the result of a  $\sim 90^\circ$  kink, or deflection, in the crack’s path. Yeni and Norman (2000) found that cracks in osteonal bone can deflect from a transverse direction of propagation to grow along the cement line interface between an osteon and the surrounding mineral matrix. The cement line acts as a path of least resistance, causing the crack to redirect away from the nominal path of maximum stress.

Evidence suggests that failure of manatee rib cortical bone is governed by mode I loading even in the presence of mixed mode of loading. A characteristic of mode I failure that is not present during mode II or mode III failure is the ability to identify the fracture origin and the geometry of the flaw: These features were found during our study. Fracture toughness for all orientations of manatee rib bone is therefore reported as mode I fracture toughness.

The toughness values found here were  $\sim 28\%$  less for transversely propagated cracks than in Yan et al.’s manatee rib single edge v-notch beam (SEVNB) study (2006b) ( $K_{IC}=4.7\pm 0.3$  for transversely propagated cracks in Yan’s study). Factors such as specimen size and microstructural variation within a single animal or between animals may be responsible for the difference in  $K_{IC}$  values between these two studies.

It should also be noted that bone is considered an R-curve material, meaning that fracture resistance increases with crack length. In bone, the R-curve behavior is due predominantly to microstructural toughening mechanisms such as fiber bridging (Nalla et al., 2005a). Other studies in manatee bone fracture support the idea of R-curve behavior. Yan (2006a) found a  $K_{IC}$  value of 2 MPa $\sqrt{m}$  for a crack size of 0.2 mm; in another study Yan determined a  $K_{IC}$  value of 3 MPa $\sqrt{m}$  for a crack size range of 0.3-0.6 mm; and in the 2006b study, a  $K_{IC}$  of 4.7 MPa $\sqrt{m}$  for a crack size of 1 mm. Clifton et al. (2007) found a toughness of  $\sim 8$  MPa $\sqrt{m}$  for a crack size of 2-3.5 mm. Thus, all of the different studies are consistent with the concept of R-curve behavior in manatee bone (Figure 9-7) and with previous studies in other bone materials. Future studies on manatee rib should address the issue of R-curve behavior in a more systematic manner. The procedures used in the present analysis can be used as a template for further cortical bone fracture studies that aim to discern a broader spectrum of fracture resistance values by combining numerical simulation with experimental fracture parameters.

### **Conclusions**

Fracture toughness values from the computational analysis were nearly identical to results found using traditional experimental calculations for all crack orientations. The small difference between experimental and computational results reveals that the isotropic assumption placed on the geometry factor for the experimental calculation does not significantly influence fracture toughness results, and it shows that computational analyses may not be necessary to determine fracture properties in cortical bone. The largest anisotropic ratio for fracture toughness values in manatee rib was found to be 4.3 in our study, which is a much larger ratio than what is traditionally found in cortical bone (1.3-2.0). Further investigations should look into the mechanisms responsible for such a large ratio of maximum to minimum fracture toughness.

Table 9-1. Orientation dependent fracture toughness and fracture parameters of manatee rib (cortical) bone. Mean values are presented for crack length and failure load along with the coefficient of variation,  $CV$ , (in parentheses) for each fracture toughness orientation. The number of specimens ( $n$ ) used during the experimental component of the test are also presented. Stress intensity factors (SIFs) are denoted for varying orientations as  $K^{xy}$ , where  $x$  is the loading direction and  $y$  is the crack growth direction. The critical stress intensity factors (fracture toughness,  $K_{IC}$ ) are obtained by implementing the mean crack lengths and failure loads into the models. Fracture toughness values calculated by finite element analysis are reported as  $K_{IC\ FEA}$ , while experimental plane strain fracture toughness values with identical parameters to those used in the numerical model are reported as  $K_{IC\ exp1}$ . Mean and standard deviations for plain strain fracture toughness calculated using traditional equations and averaging methods are reported as  $K_{IC\ exp2}$ .

SIF Orientation	$K^{12}$ ( $n=7$ )	$K^{13}$ ( $n=6$ )	$K^{23}$ ( $n=8$ )	$K^{21}$ ( $n=12$ )	$K^{31}$ ( $n=8$ )	$K^{32}$ ( $n=8$ )
Crack Length (mm)	1.27 (31%)	1.30 (18%)	1.63 (19%)	1.14 (19%)	1.09 (14%)	1.17 (24%)
Failure Load (N)	1856 (15%)	1860 (18%)	448 (26%)	641 (17%)	592 (25%)	448 (16%)
$K_{IC\ FEA}$ (MPa $\sqrt{m}$ )	3.2	3.4	1.0	1.1	1.0	0.8
$K_{IC\ exp1}$ (MPa $\sqrt{m}$ )	3.2	3.2	0.9	1.1	0.9	0.7
$K_{IC\ exp2}$ (MPa $\sqrt{m}$ )	3.4 $\pm$ 0.5	3.5 $\pm$ 0.7	0.9 $\pm$ 0.2	1.1 $\pm$ 0.2	1.1 $\pm$ 0.3	0.8 $\pm$ 0.2

Table 9-2. Selected studies measuring fracture toughness of compact bone (modified from Yan (2005)).

Investigators	Testing Method	Bone Source	Fracture Direction	Fracture Toughness (MPa·√m)
Melvin and Evans (1973)	Single-edge notched beam	Bovine femur	Longitudinal	3.21±0.43
			Transverse	5.58±0.52
Behiri and Bonfield (1984)	Compact tension	Bovine tibia	Longitudinal	2.8-6.3
Norman et al. (1992)	Compact tension	Bovine tibia	Transverse	4.93-12.64
Vashishth et al. (1997)	Compact tension	Human tibia	Longitudinal	1.6-2.5
Wang et al. (1996)	Compact sandwich	Baboon femur	Longitudinal	2.25±0.18
Zioupos and Currey (1998)	Single-edge notched beam	Human femur	Longitudinal	6.41
Wang et al. (2002)	Single-edge notched beam	Human femur	Transverse	5.09±0.98
De Santis et al. (2000)	Chevron-notched short rod	Bovine femur	Longitudinal	4.8±0.5
Nalla et al. (2003)	Fatigue precracked flexure	Human humerus	Longitudinal	3.53±0.13
			Transverse	5.33±0.41
Yan et al. (2006a)	3-point bend	Manatee rib	Transverse	2.3±0.4
Yan et al. (2007)	Chevron-notched beam	Manatee rib	Transverse	4.5±0.5
		Bovine femur	Transverse	5.8±0.5
Yan et al. (2006b)	Single-edge V-notched beam	Manatee rib	Transverse	4.7±0.3



Figure 9-1. Manatee skeleton. Center ribs from adult manatees were used in this study. All specimens were harvested from the middle third of the ribs to reduce variability in fracture toughness results. Image courtesy of Roger Reep (department of physiological sciences, University of Florida).

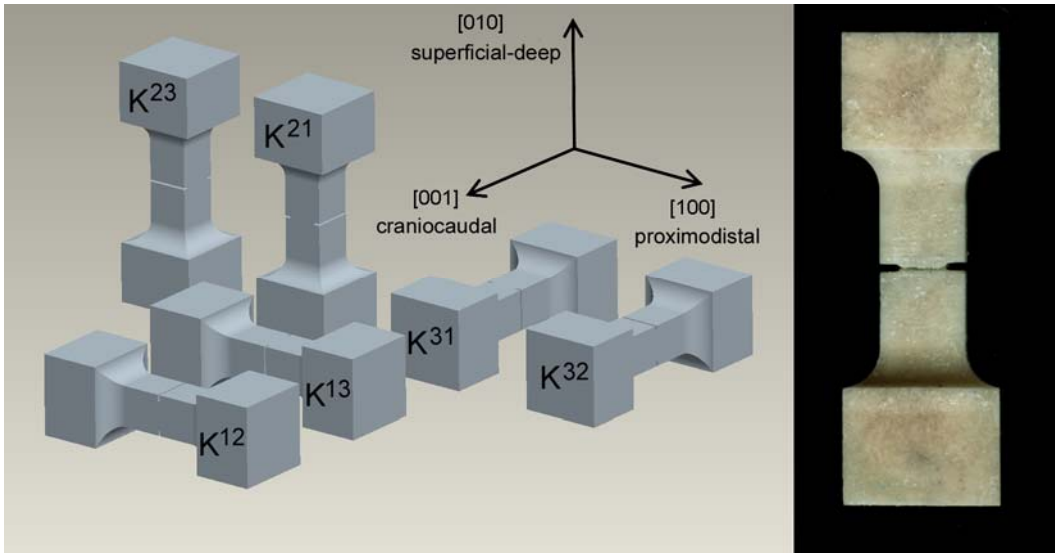


Figure 9-2. Mode I (opening mode) stress intensity factor (SIF) nomenclature (left). Mode I SIF is presented for each specimen orientation as  $K^{ij}$ , where superscript  $i$  denotes the loading direction and  $j$  denotes the crack growth direction. Note that the 1, 2, and 3 directions are denoted as [100], [010], and [001] in Miller index notation and as medial-lateral, anterior-posterior, and cranial-caudal, respectively, in anatomic coordinates relative the manatee. The photograph (right) shows a failed cranial-caudal specimen ( $K^{31}$ ).

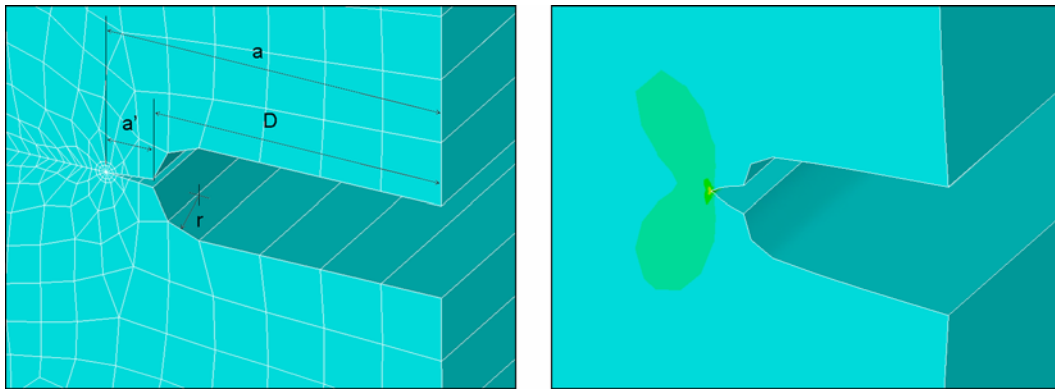


Figure 9-3. Notch tip geometry showing an illustration of the finite elements and variables used in the fracture toughness models (left), and vertical (opening mode) component stress contour at the crack tip (right).

### K<sub>IC</sub> vs. normalized crack front

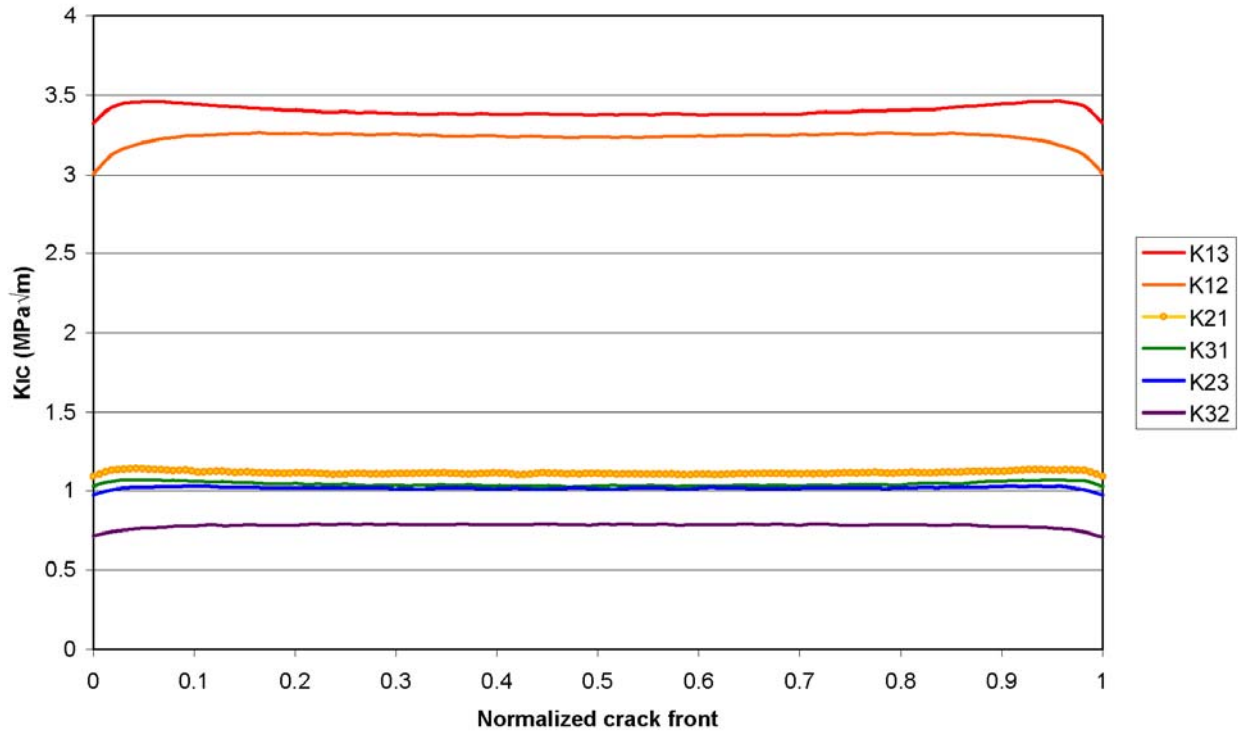


Figure 9-4. Numerically-determined mode I SIF versus normalized crack front. The SIF values presented in this figure can be taken as the fracture toughness ( $K_{IC}$ ) of the specimens because experimentally-measured crack lengths and failure loads were inserted into the numerical model. The legend shows the fracture toughness values in descending order.

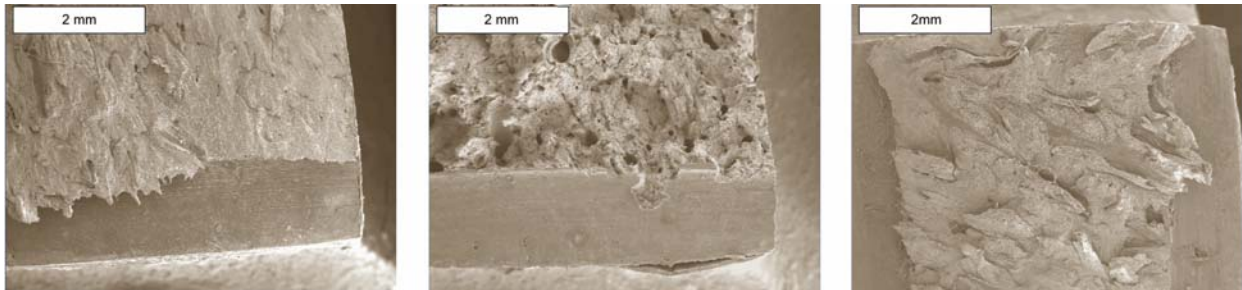


Figure 9-5. Scanning electron micrographs of typical fracture surfaces from specimens loaded in each of the three principal orthogonal directions: superficial-deep (left), proximodistal (middle), and craniocaudal (right). Notice the variation in microstructure with specimen orientation. The smooth regions in the images are the notches.

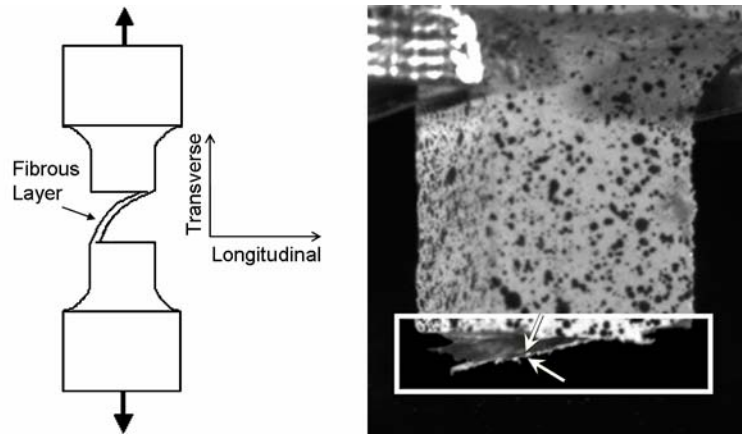


Figure 9-6. Schematic (left) demonstrating the “peeling” of fibrous layers during the fracture experiments. Transverse ( $K^{I2}$ ) fracture specimen (right) showing the overlap of two oppositely facing cracks growing in the longitudinal direction, separated by a sheet of fibrous plexiform bone tissue (highlighted region).

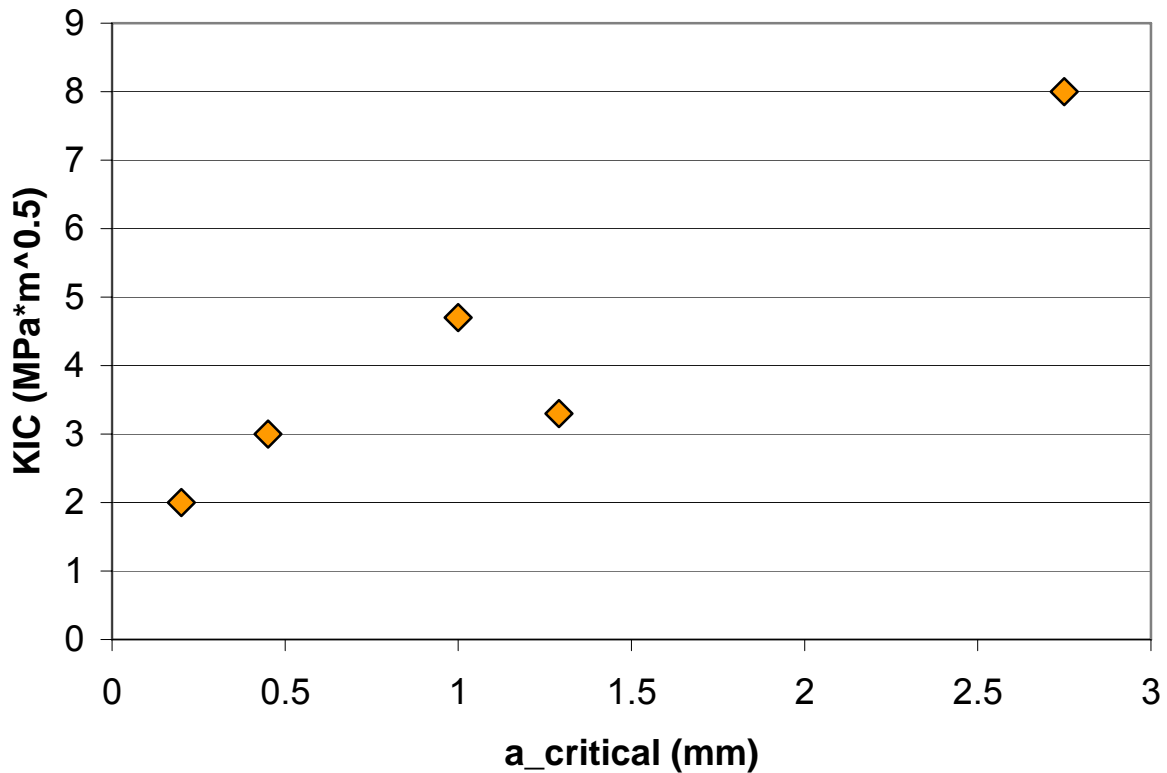


Figure 9-7. R-curve behavior of manatee rib bone demonstrating a trend of increasing fracture toughness with increasing critical crack length. The data in this plot is presented from several experiments involving manatee rib bone with various crack lengths (Yan, 2006a, b; Clifton et al., 2007; and the present study).

## CHAPTER 10 CONCLUDING REMARKS

The objectives of the present work were to develop an understanding of fracture in cortical bone and to characterize and document the material and fracture properties of manatee rib bone as a function of orientation. The former aspect is achieved via a unique synthesis of experimental and computational analyses that have never been performed on cortical bone. This document provides the framework for bone mechanics researchers to obtain more information on the orientation dependence of bone fracture than was previously available. The efficacy of this combined experimental and numerical technique is tested on manatee rib.

The manatee rib bone work presented here supports previous work aimed at reducing the “impact” of watercraft on the manatee population. Prior to this work, fracture toughness was only known for cracks propagating along the transverse direction of the rib bone. When considering the potential for watercraft to impact a manatee at various angles, the next step is to identify the fragility of manatee rib bone as a function of material orientation. In our study, we analyzed fracture toughness for cracks traversing the longitudinal direction of the rib bones and determined that this never before analyzed crack orientation produced fracture toughness values ~4 times smaller than for transversely propagating cracks, which were also analyzed in our study. The anisotropic ratio for fracture toughness in this study is higher than that reported for bones from other animals (4.3 here compared to 1.3-2.0 elsewhere). Furthermore, findings from this study suggest that manatee rib material properties are more anisotropic than plexiform bone from other animals (2.9 here compared to 1.18-1.47 in other animals).

In conclusion, manatee rib bone material and fracture properties were found to vary strongly as a function of material orientation. The symmetry of manatee rib bone was determined

to be orthotropic. Testing of specimens that had been air-dried for 2 weeks demonstrated the nonlinear behavior of the material. Complete removal of the water content should result in a linear stress strain curve, suggesting that the water content was not completely removed from the specimens in our study. However, the sources of the nonlinearity were not fully investigated in this study, although an attempt was made to determine whether or not manatee rib bone is viscoelastic. Unfortunately, malfunction of the universal testing machine used to load the specimens in this study caused the strain rates to not vary significantly enough to provide strong evidence for the conclusion that manatee rib bone elastic modulus is strain rate dependent (i.e., viscoelastic). However, strain rate data varied significantly for one specimen, and that specimen demonstrated viscoelastic behavior (i.e., there was an increase in elastic modulus with an increased applied strain rate) (see Appendix A). Additional testing at largely differing strain rates on a plurality of specimens could be conducted to confirm the viscoelasticity of the material. This would further support the evidence of viscoelasticity found by cyclically loading several specimens into the non-linear range of the material that demonstrated a lack of hysteresis. Other sources of nonlinearity could be investigated using histology. Histological staining could be performed during cyclic testing to confirm the presence of microcracking.

Chapter 9 discusses the R-curve behavior of bone and provides evidence that manatee rib bone is an R-curve material. However, additional testing could further elucidate the effects of differing crack lengths on the fracture toughness of the material. The effects of crack turning for transversely oriented cracks could also be further investigated. Transverse cracks were found to deviate from their initial trajectory as the cracks grew in the manatee rib bone specimens. Several crack-turning models are available in the literature, and each could be used to determine which model best fits the manatee rib bone experimental fracture test data. Furthermore, grooves could

be machined into these specimens to keep the cracks from deviating from their initial trajectory so that there is no mixed mode loading in these specimens. This approach has been used by several authors to retain opening mode failure in cortical bone specimens.

Lastly, it is not known to what degree soft tissues surrounding the rib reduce localized trauma on the rib during impact with watercraft. This is an area of research that should be conducted to provide a direct link between fracture in manatee rib and collisions with watercraft. However, the scientific evidence presented in this work as well as that presented by Drs. Kari Clifton, Jiahau Yan, Roger Reep, John Mecholsky, Jr., and Laurie Gower on skeletal tissue mechanics of the Florida manatee strongly suggest a need to modify boater activities in manatee populated waterways to help protect this endangered species. Suggested modifications to boater activities include: enforcement of reduced watercraft speeds, mandatory polarized sunglasses for all watercraft operators, technologies that alert manatees to approaching watercraft by making use of their unique sensory organs, and enforcement of safe watercraft operation practices.

APPENDIX A  
TENSILE TESTING AT VARIOUS CROSSHEAD SPEEDS

Various strain rates (calculated from crosshead speeds and specimen gage lengths) were applied to tensile specimens fixed with strain gages. Four dog-bone shaped specimens oriented about each of two material directions (superficial-deep and proximodistal) were loaded and unloaded for three to five cycles at presumably different strain rates. A rheostat on the universal testing machine (MTI 30K, Materials Testing, Inc., Roswell, GA) was adjusted to three different positions (one for each load cycle). The same three rheostat settings were used for all specimens. However, issues with one of the control modules in the testing machine resulted in crosshead speeds varying less with a load present than during the zero-load crosshead speed calibration. This caused the crosshead speeds to not vary significantly between each test, and thus the modulus values for all but one specimen did not vary significantly between tests. Results from the only specimen yielding significantly different elastic moduli between tests are provided in the table below. The cyclic tests at each rheostat setting did not result in any hysteresis although several specimens were loaded into their nonlinear range. This demonstrates the viscoelasticity of manatee rib bone. The viscoelastic behavior of manatee rib bone can be further investigated by testing additional specimens at strain rates significantly different from one another to determine the strain rate dependence of the material's elastic modulus.

Table A-1. Viscoelastic properties of manatee rib bone. Three cross-head speeds were tested for their effect on elastic modulus for one specimen loaded in the proximodistal direction.

Manatee rib bone viscoelasticity			
Crosshead speeds (mm/min)	0.58	0.80	0.91
Elastic modulus (GPa)	16.1	18.8	22.3

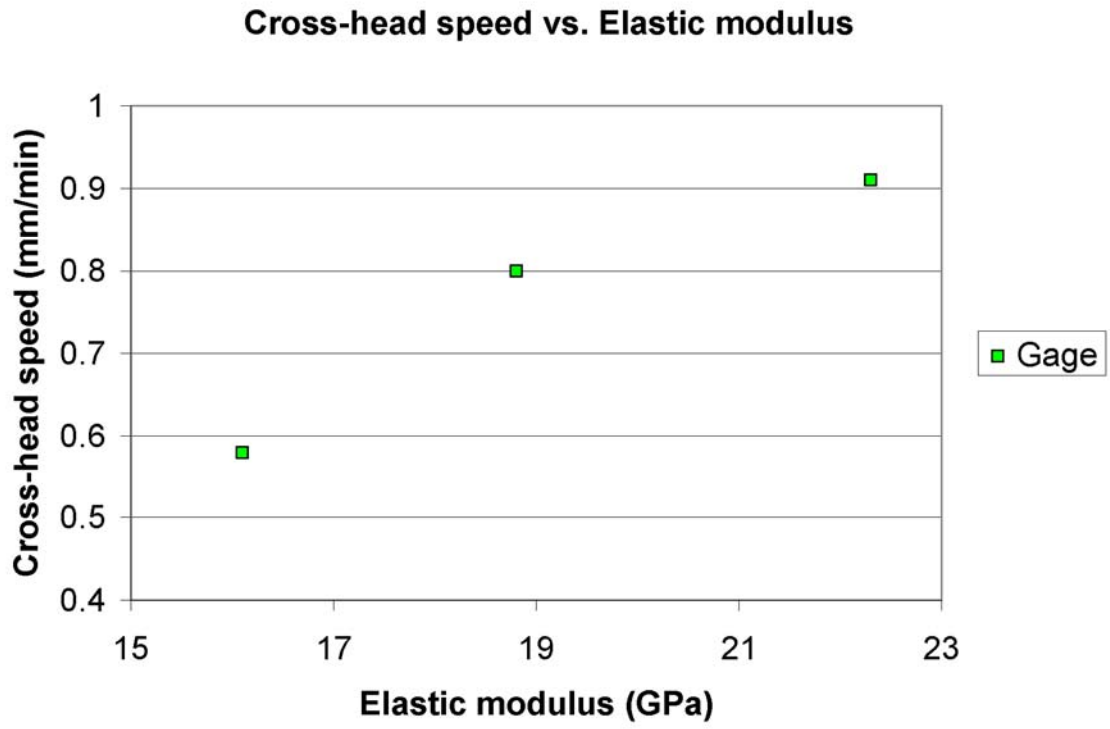


Figure A-1. Viscoelastic properties of manatee rib bone. Results are shown for one proximodistal specimen loaded at three different strain rates.

## APPENDIX B MATERIAL PROPERTY CALCULATIONS

The following pages show the custom Mathcad code (Mathcad v.12.1, Mathsoft Engineering and Education, Inc.) used to average deformation rates and calculate strains, Poisson's ratios, and elastic moduli from VIC data for three orientations of tensile specimens. Files generated by VIC3D (VIC-3D Digital Image Correlation v.2006.0.0, Correlated Solutions, Inc., West Columbia, SC) were input into Mathcad for manipulation. The input data files included position, deformation, and deformation rate information for the data points on the front and back gage sections of MIC tensile specimens. After performing filtering operations to remove potentially erroneous data, the deformation rate was calculated for data points within the gage section of the specimen. Next, the normal and Poisson strains are calculated as the slope of the vertical and horizontal position versus deformation data, respectively. Strains and deformation rates are averaged from the front and back specimen gage sections to increase the data available for the analysis thereby reducing the error of the analysis compared to analyzing only one specimen face. Also, averaging the data removes the effects of unwanted bending in the tensile specimens so the strains are those due only to tensile (not bending) loads. Poisson's ratio is calculated as negative the ratio of Poisson to normal strain. Poisson strain, normal strain, deformation rate, and Poisson's ratio were next exported from the custom program for use in a data compilation file that links data from each load step (including Labview generated load data) in order to calculate elastic modulus for each specimen. A third program (not shown) was written to link data from each specimen in order to determine mean Poisson's ratios and elastic moduli and to determine the standard deviations for each specimen orientation. Similar programs were also developed for the shear tests.

## Mathcad File Used to Find the Strains and Displacement Rate for a Single Pair of Images

MSW 0253 (Manatee I.D.)  
1ML (Specimen I.D.)  
Image 23 (Image I.D.)

Begin the origin of arrays and matrices with subscript 1, not 0 as is the default  
ORIGIN:= 1

Read input data from Excel file (import raw data from .csv file)  
Data file: 1ML\_023\_0.csv

front := 

	1
1	0

      back := 

	1
1	0

Column I.D.  
1 2 3 4 ... 7 8 9 ... 16 17 18  
X Y Z correlation ... U V W ... dU/dt dV/dt dW/dt ...

Sort data (ascending order for column 4)

front := csort(front, 4)  
back := csort(back, 4)

rows (front)

i\_mf := rows(front)      i\_mf =  $5.872 \times 10^3$   
if := 1, 2.. i\_mf

columns (front)

j\_mf := cols(front)      j\_mf = 21  
jf := 1, 2.. j\_mf

rows (back)

i\_mb := rows(back)      i\_mb =  $3.286 \times 10^3$   
ib := 1, 2.. i\_mb

columns (back)

j\_mb := cols(back)      j\_mb = 21  
jb := 1, 2.. j\_mb

Extract vector elements to determine how many data points must be filtered from the dataset

corr\_f := submatrix(front, 1, i\_mf, 4, 4)  
corr\_b := submatrix(back, 1, i\_mb, 4, 4)

Only allow data points with correlation values greater than zero

cf(xf) := 0 < x1

cb(xb) := 0 < xt

```
Extractf(Qf, cf) := | if ← 1
                    | Nf ← 1
                    | for jf ∈ 1..rows(Qf) - 1
                    |   if cf(Qfjf) = 1
                    |     | Nfif ← Qfjf
                    |     | if ← if + 1
                    | Nf
Extractb(Qb, cb) := | ib ← 1
                    | Nb ← 1
                    | for jb ∈ 1..rows(Qb) - 1
                    |   if cb(Qbjb) = 1
                    |     | Nbib ← Qbjb
                    |     | ib ← ib + 1
                    | Nb
```

corr<sub>f</sub> := Extractf(corr<sub>f</sub>, cf)

corr<sub>b</sub> := Extractb(corr<sub>b</sub>, cb)

### Remaining rows after removing poorly correlated data

i<sub>mf</sub> := rows(corr<sub>f</sub>)                      i<sub>mf</sub> = 4.687 × 10<sup>3</sup>

if := 1, 2.. i<sub>mf</sub>

i<sub>mb</sub> := rows(corr<sub>b</sub>)                      i<sub>mb</sub> = 2.7 × 10<sup>3</sup>

ib := 1, 2.. i<sub>mb</sub>

### Reverse the order of the matrix so the poorly correlated data points appear at the bottom and crop the matrix to remove poorly correlated data

front := reverse(front)

front := submatrix(front, 1, i<sub>mf</sub>, 1, j<sub>mf</sub>)

back := reverse(back)

back := submatrix(back, 1, i<sub>mb</sub>, 1, j<sub>mb</sub>)

### Re-order the matrix in ascending order of Y-axis position

front := csort(front, 2)

back := csort(back, 2)

### Filter out W values less than or greater than 2\*stdev from the mean

W<sub>f</sub> := submatrix(front, 1, i<sub>mf</sub>, 9, 9)

W<sub>b</sub> := submatrix(back, 1, i<sub>mb</sub>, 9, 9)

$cf(xf) := -2 \text{stdev}(Wf) + \text{mean}(Wf) < xf < 2 \text{stdev}(Wf) + \text{mean}(Wf)$   
 $cb(xb) := -2 \text{stdev}(Wb) + \text{mean}(Wb) < xb < 2 \text{stdev}(Wb) + \text{mean}(Wb)$

```

Extractf(Qf, cf) :=
  if ← 1
  Nf ← 1
  for jf ∈ 1..rows(Qf) - 1
    if cf(Qf_jf) = 1
      Nf_if ← Qf_jf
      if ← if + 1
  Nf
Extractb(Qb, cb) :=
  ib ← 1
  Nb ← 1
  for jb ∈ 1..rows(Qb) - 1
    if cb(Qb_jb) = 1
      Nb_ib ← Qb_jb
      ib ← ib + 1
  Nb

```

$Wf := \text{Extractf}(Wf, cf)$   
 $Wb := \text{Extractb}(Wb, cb)$

### Redefine rows after removing data with excessive out-of-plane displacement noise

$i\_mf := \text{rows}(Wf) \quad i\_mf = 4.515 \times 10^3$   
 $if := 1, 2.. i\_mf$

$i\_mb := \text{rows}(Wb) \quad i\_mb = 2.583 \times 10^3$   
 $ib := 1, 2.. i\_mb$

### Reverse the order of the matrix so the data points with excessive noise appear at the bottom and crop the matrix to remove the noisy data

$front := \text{reverse}(front)$   
 $front := \text{submatrix}(front, 1, i\_mf, 1, j\_mf)$

$back := \text{reverse}(back)$   
 $back := \text{submatrix}(back, 1, i\_mb, 1, j\_mb)$

### Re-order the matrix in ascending order of Y-axis position

$front := \text{csort}(front, 2)$   
 $back := \text{csort}(back, 2)$

### Extract individual components from the input matrix

```
Xf := submatrix(front, 1, i_mf, 1, 1)
Xb := submatrix(back, 1, i_mb, 1, 1)
Yf := submatrix(front, 1, i_mf, 2, 2)
Yb := submatrix(back, 1, i_mb, 2, 2)
Zf := submatrix(front, 1, i_mf, 3, 3)
Zb := submatrix(back, 1, i_mb, 3, 3)
Uf := submatrix(front, 1, i_mf, 7, 7)
Ub := submatrix(back, 1, i_mb, 7, 7)
Vf := submatrix(front, 1, i_mf, 8, 8)
Vb := submatrix(back, 1, i_mb, 8, 8)
Wf := submatrix(front, 1, i_mf, 9, 9)
Wb := submatrix(back, 1, i_mb, 9, 9)
```

### Find the average rate of deformation for the data set

Note- use the last 4/5ths of the data (bottom fifth of target region) since velocity in this region is representative of the cross-head speed

```
dV_dt_f := submatrix( front,  $\frac{4}{5}$ i_mf, i_mf, 17, 17 )
```

```
dV_dt_f := mean(dV_dt_f)·60
```

```
dV_dt_b := submatrix( back,  $\frac{4}{5}$ i_mb, i_mb, 17, 17 )
```

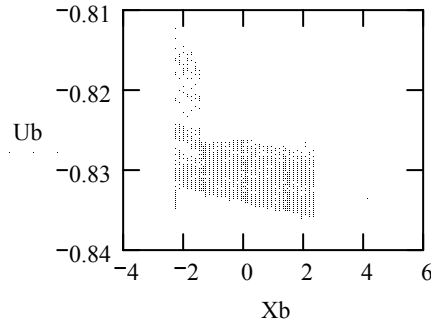
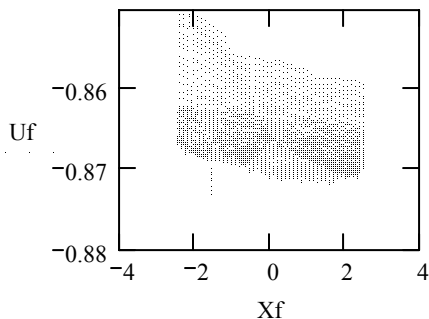
```
dV_dt_b := mean(dV_dt_b)·60
```

### Average rate of deformation (mm/min)

$$\overline{dV\_dt\_f} = -0.988$$

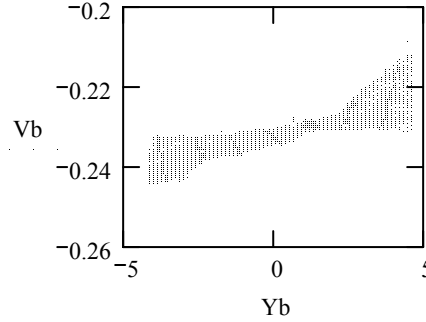
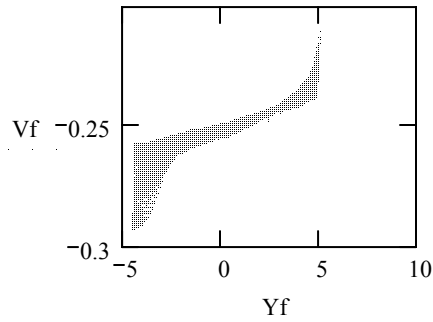
$$\overline{dV\_dt\_b} = -0.836$$

### Strain in the X-direction (X and U are presented in mm)



$$exf := \text{slope}(Xf, Uf) = (-8.371 \times 10^{-4}) \quad exb := \text{slope}(Xb, Ub) = (-9.334 \times 10^{-4})$$

### Strain in the Y-direction (Y and V are presented in mm)



$$\begin{aligned} \text{eyf} &:= \text{slope}(Yf, Vf) & \text{eyf} &= 4.183 \times 10^{-3} \\ \text{eyb} &:= \text{slope}(Yb, Vb) & \text{eyb} &= 2.062 \times 10^{-3} \end{aligned}$$

Average the strains and strain rates from the front and the back of the specimen

$$\begin{aligned} \epsilon_x &:= \frac{\epsilon_{xf} + \epsilon_{xb}}{2} & \epsilon_x &= -8.852 \times 10^{-4} \\ \epsilon_y &:= \frac{\epsilon_{yf} + \epsilon_{yb}}{2} & \epsilon_y &= 3.122 \times 10^{-3} \\ dV_{dt} &:= \frac{dV_{dt\_f} + dV_{dt\_b}}{2} & dV_{dt} &= -0.912 \text{ mm/min} \end{aligned}$$

Calculate Poisson's Ratio

$$\nu_{xy} := -\frac{\epsilon_x}{\epsilon_y} \quad \nu_{xy} = 0.284$$

Write the results to a file using the “prn” format

$$\text{Results} := \begin{pmatrix} \epsilon_x \\ \epsilon_y \\ \nu_{xy} \\ dV_{dt} \end{pmatrix}$$

WRITEPRN(“C:\Jeff\School\...\MSW 0253\1ML\ML 1 023.prn”) = Results

### **Mathcad File Used to Compile Datasets From a Single Specimen and to Calculate Elastic Modulus**

MSW 0253 (Manatee I.D.)  
1ML (Specimen I.D.)

Begin the origin of arrays and matrices with subscript 1, not 0 as is the default

ORIGIN:= 1

Read data sets (manually input each results data file)

Results\_001=READPRN(“C:\Jeff\School\...\1ML\_001.prn”) = Results  
Results\_002=READPRN(“C:\Jeff\School\...\1ML\_002.prn”) = Results

...  
 Results\_024=READPRN("C:\Jeff\School\...\1ML\_024.prn")=Results

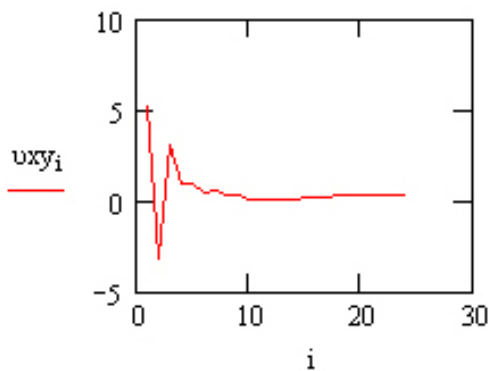
Compile data sets

Results=augment(Results\_001,Results\_002,...,Results\_024)

Extract individual components of the compiled data set

ex := submatrix(Results, 1, 1, 1, cols(Results))      ex :=  $\mathbf{ex}^T$   
 ey := submatrix(Results, 2, 2, 1, cols(Results))      ey :=  $\mathbf{ey}^T$   
 ez := submatrix(Results, 3, 3, 1, cols(Results))      ez :=  $\mathbf{ez}^T$   
 dV\_dt := submatrix(Results, 4, 4, 1, cols(Results))      dV\_dt :=  $\mathbf{dV\_dt}^T$   
 mean(dV\_dt) = -0.589  $\frac{\text{mm}}{\text{min}}$   
 vxy := submatrix(Results, 5, 5, 1, cols(Results))      vxy :=  $\mathbf{vxy}^T$

i := 1, 2.. rows(vxy)



Filter out all invalid values of Poisson's ratio

c(v)=0<v<0.5

Extract(Q, c) :=  $\left\{ \begin{array}{l} i \leftarrow 1 \\ N \leftarrow 1 \\ \text{for } j \in 1.. \text{rows}(Q) - 1 \\ \quad \text{if } c(Q_j) = 1 \\ \quad \quad \left\{ \begin{array}{l} N_i \leftarrow Q_j \\ i \leftarrow i + 1 \end{array} \right. \\ N \end{array} \right.$

vxy := Extract(vxy, c)

Read input data from Excel file (raw data from .xls file)

Data file: 1ML Front Face.xls

loadfile :=

	1
1	0

Column I.D.

1 2 3 ...  
count load (lbs) time (s) ...

rows

i\_mf := rows(loadfile) i\_mf = 48  
if := 1,2..i\_mf

columns

j\_mf := cols(loadfile) j\_mf = 3  
jf := 1,2..j\_mf

Extract the load and time vectors from the loadfile matrix

load := submatrix(loadfile, 24, i\_mf, 2, 2)  
time := submatrix(loadfile, 24, i\_mf, 3, 3)

Calculate stresses

area = 0.05806 mm<sup>2</sup>  
stress :=  $\frac{\text{load}}{\text{area}}$  psi

Calculate the elastic modulus for each dataset

modulus\_psi<sub>i</sub> :=  $\frac{\text{stress}_i}{\epsilon y_i}$  psi

Convert stresses to GPa for comparison with Bratt and Kari's reporting of elastic modulus

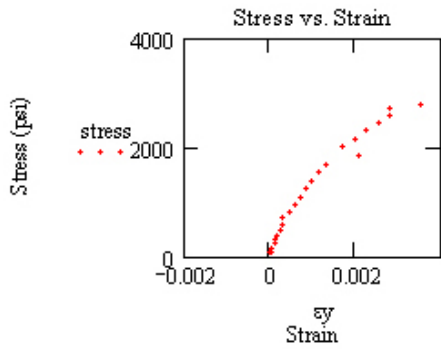
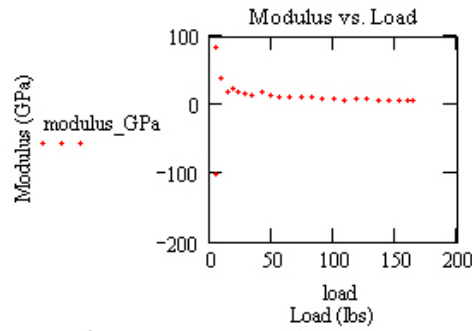
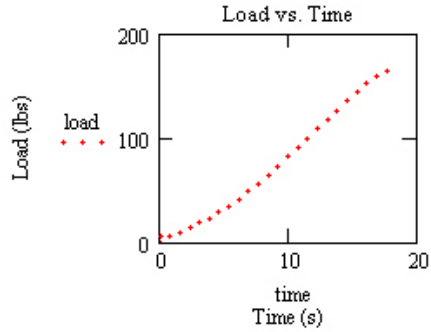
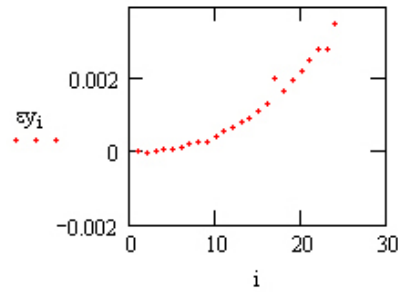
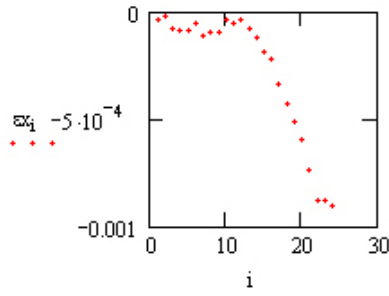
psi2GPa := 6.8947610<sup>-6</sup>

Finn := ",,.,.,m,.,.,mmm"

Jake := "Gfff 0020"

modulus\_GPa := modulus\_psi · psi2GPa

Plot or tabulate the data to check for reasonableness of the values



	1
1	0.388
2	0.342
3	0.342
4	0.101
5	0.125
6	0.162
7	0.166
8	0.165
9	0.251
10	0.26
11	0.268
12	0.291
13	0.313
14	0.313

	1
1	84.848
2	-101.453
3	39.045
4	18.604
5	23.763
6	19.902
7	15.414
8	14.493
9	17.582
10	13.471
11	11.261
12	10.949
13	10.523
14	10.151
15	9.365
16	8.933

## APPENDIX C VISUAL IMAGE CORRELATION (VIC) EQUIPMENT TUTORIAL

University of Florida  
Mechanical and Aerospace Engineering  
Location (Responsible Faculty): 118 NEB (Dr. Peter Ifju)

### In This Document

- Specimen Preparation
- Equipment Setup
- Computer Setup
- Pre-Photo Adjustments
- Camera Calibration
- VIC Testing
- Pre-VIC Analysis
- VIC Analysis
- Example Analysis

### Specimen Preparation

Begin by **painting** your **specimen white** (if it is not already light in coloration).

Slightly **enlarge the nozzle** of a **black spray paint can** using a pin (to increase droplet size).

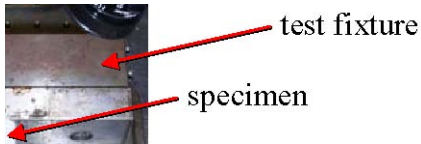
**Speckle** the **specimen** with the black spray paint (do not overspray).



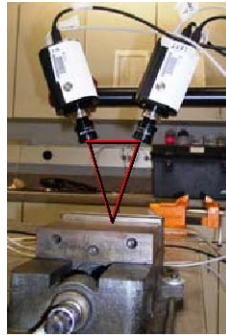
### Equipment Setup

**Place specimen in test fixture.**





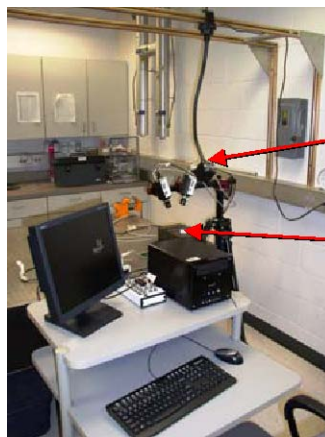
**Position the cameras** to form an **equilateral triangle** with the specimen. However, if imaging 2 perpendicular surfaces at a time, you may need to place the cameras closer together. Note that any deviation from an equilateral triangle degrades the calibration of the equipment.



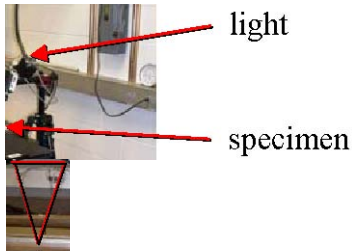
**Connect wires** to appropriately labeled components.



**Place light** so that it illuminates the specimen.



**Remove lens covers** from cameras.



## Computer Setup

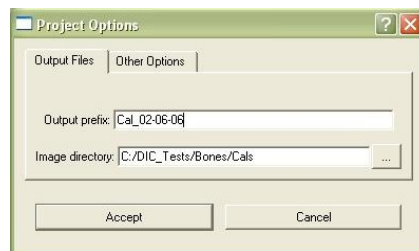
Turn on the computer and **log on** (user name = █; password = █).

Open **Windows Explorer** and **create a new directory** for your images (named “pics/date/” or some other identifiable name) and one for your calibration images (named “cals/date/” or some other identifiable name).

On the **Windows Start Menu**, click on the shortcut to “VicSnap”.



Enter the **calibration image directory** name you provided earlier at the **Image Directory** prompt and choose a **prefix** name for you images (e.g., “cal\_date\_name”). Your prefix will be followed by a numeric sequence (000, 001, 002, etc.) as images are stored to the computer. Images are stored in tiff format (.tif).



## Pre-photo Adjustments

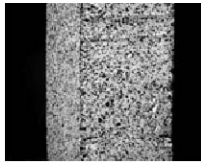
Turn on **camera power** (turn switches to **1394 PWR**, not Aux PWR).

Flip the **transformer power switch on** (located on the surge protector).



 VicSnap  
Turn on the **light**.

If you have not already opened **VicSnap**, do so now. You should be able to see the specimen in the VicSnap image viewer window on the computer screen.



Adjust the **position of the light** to optimize the view of the specimen on the computer screen. An optimal image shows good visibility of the specimen without over- or under-exposure. If viewing two perpendicular surfaces at once, try to position the camera to illuminate both surfaces equally.

**Lighting exposure** can be adjusted using the slider on the camera lens. Exposure can also be adjusted by moving a slider bar in the VicSnap window, but it is recommended that the slider bar remain in the middle of the range.

If the **image** is out of **focus**, use an **allen wrench** to adjust the lens focal length. Be careful not to loosen the set screw too much or the lens will detach completely from the camera.



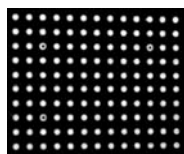
## Camera Calibration

Change the directory to the “*cal/date/*” **directory** if you did not specify this directory when you started VicSnap. This will require closing VicSnap and reopening the program (start menu => VicSnap) if you are in an alternate directory.

If you did not yet adjust the camera focus and light exposure with your specimen in place, do that now. Otherwise, move on to the next step.

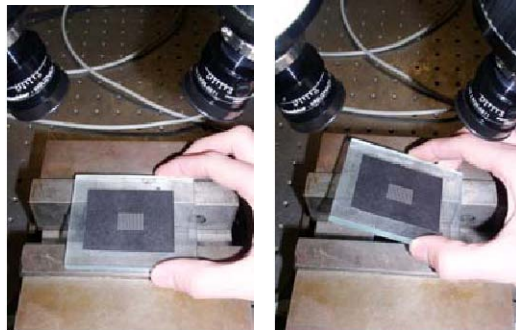
 set screw

Select a **calibration dot-matrix image** (black paper with white dots) according to your image resolution needs. Dot spaces range from 1.5 to 3mm. The closer your specimen is to the camera, the smaller dot spacing you should use (and the higher the image resolution will be).



Glue the calibration dot-matrix paper to a hard, flat surface that is close to the size of the paper.

Remove the specimen and **place the calibration paper in front of the camera**. Take **at least 20 photos** while **adjusting the position and angle** of the paper, being sure to keep all dots in view of both cameras for each photo (**press the space bar to take photos**). Two images will be stored to your calibration image directory each time you press the space bar (one from the left camera and one from the right).



Turn the **light off**.

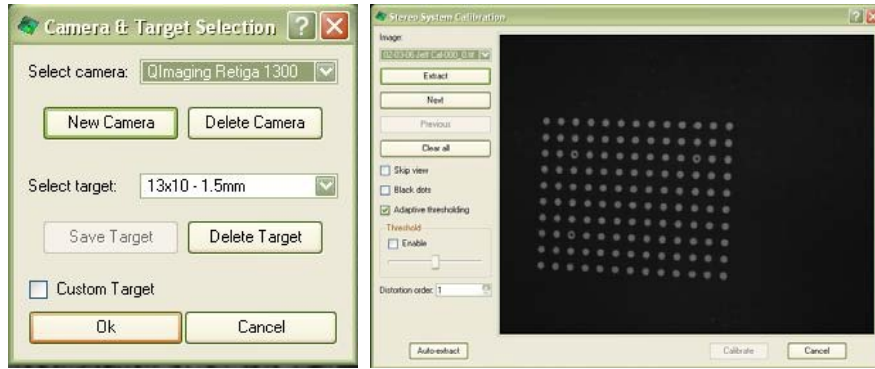
Click “*shortcut to VIC3D*” on the start menu



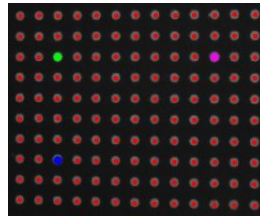
Click on the **icon** that looks like the calibration paper. In the pop-up window, locate the calibration image directory (“*cal/cal\_date/*”). **Select** all of the **photos** in the directory (to select all images at once, click on the first image, scroll to the last image, hold down shift and click on the last image) and press **open**.



Click on the **calibration icon**  (it resembles a set of calipers). **Select** “*QImaging Retiga 1300*” for the **type of camera**. Under the **type of target**, select the correct pixel (dot) dimension and spacing for the calibration paper in the images. Turn on **adaptive thresholding** by checking the box.



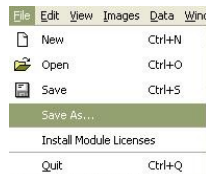
**Extract** the images, checking to see that all of the dots appear red except for 3 dots which are different colors. If you see any images with white dots during the extraction process, right click on the images at the left of the screen and click *remove*. Once erroneous pictures have been removed, click **Calibrate** and let the software calculate the standard deviations for each camera.



Once standard deviations (SD's) for each image are displayed on screen, “**remove**” any image that resulted in an **SD of 0.1 or higher** and repeat the “extraction”. Once all SD's are below 0.1 (preferably below ~0.07), click **Accept**.

Go back to **VicSnap** and **close** the program. **Re-open VicSnap** and enter the **pics image directory** name you provided earlier at the **Image Directory** prompt and choose a **prefix** name for you images (e.g., “*pics\_date\_name*”). Remember, your prefix will be followed by a numeric sequence (000, 001, 002, etc.) as images are stored to the computer.

**Save your work** into your Pics directory (or some other identifiable directory) as “analysis\_date\_name.v3d” or some other identifiable name.

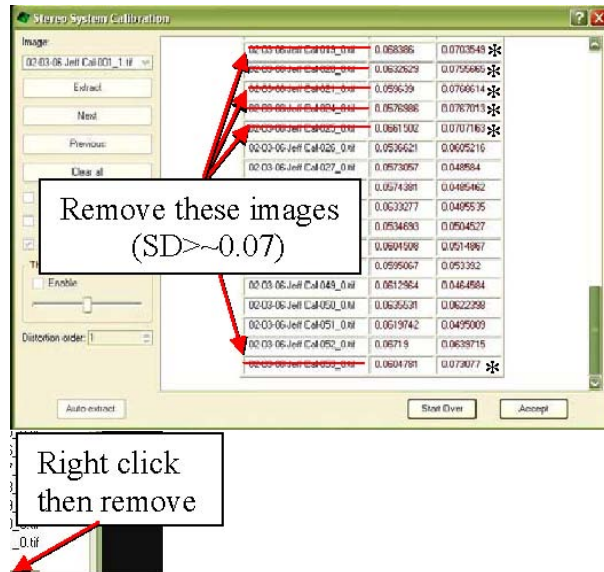


## VIC Testing

Turn the **light** back **on** and **place** the **specimen** back in position (**in view of both cameras**).

Make sure the on-screen lighting is still of good quality. Readjust the light position or exposure slider(s) if there is too much glare or if the image is not bright enough. **DO NOT adjust the camera positions or camera focus** unless if you plan to recalibrate.

Take a **reference photo** of the specimen **with no load** by **pressing the space bar**. Two images will be stored to your Pics image directory with the prefix you chose followed by a 000\_0.tif and 000\_1. These are the name of your reference images. Note that one of the images (“prefix\_000\_0.tif”) is from the left camera and the other (“prefix\_000\_1.tif”) is from the right camera.



Make sure to either **program the cameras to take photos** in intervals during your test **or** be prepared to **press the space bar** to take photos of your specimen **at key load or displacement intervals**. Begin loading the specimen and taking photos in appropriate intervals for your analysis.

Once you are done loading the specimen, **turn off** the **cameras, light, and transformer power switch** (on the surge protector).

Place the **lens covers** back **on** the **cameras**.

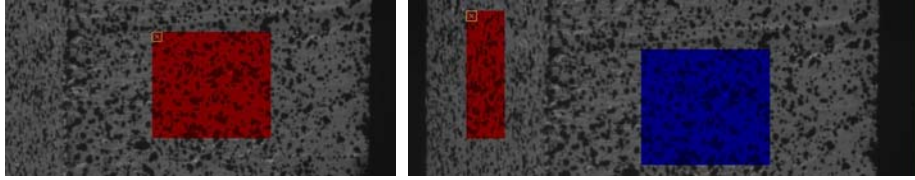
## Pre-VIC Analysis

Go back to **Vic3D**. Click the **reference image icon** . Select either the “**prefix\_000\_0.tif**” or “**prefix\_000\_1.tif**” image (either should work fine) and **click Open**.

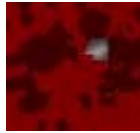
Click the **deformed image icon** . Select **all** of the **images aside from the reference images** and **click Open**.

Click an appropriate **target region selection icon**  ,  , etc.

**Highlight** areas of interest (**AOI's**) on the reference image. You can select multiple AOI's should your analysis require you to do so. Note that the red region is the active AOI.



**Cut out regions of disinterest** such as areas of high reflectivity by clicking the **cut region from aoi icon** . Use the **left mouse button** to **draw** a polygon around the region that you will cut from the selected region. Use the **middle mouse button** to **cancel**. Use the **right mouse button** to **confirm** your **cut**. Use the **cycle active AOI icon**  to toggle between AOI's if your analysis requires cutting operations to be performed on AOI's other than the active one (which is highlighted in red).



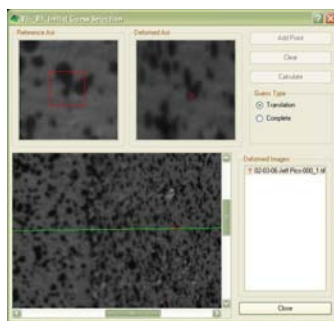
Highly reflective region cut from target AOI

Locate a seed point within an aoi which will be used to verify that both cameras are looking at the same point for your analysis. **Click the seed point icon** . **Click** an easily **identifiable feature** (e.g., a distinguishable speckle) on the active aoi.



Click the **select initial guess icon** . Two images will appear on a split screen. If the image on the right does not show the same point as on the left, move the slider bar around to **locate the point** on the right image. You can also **move the 'X' marker** on the bottom screen to **locate the seed point**. If the point cannot be found, move the seed point by clicking the seed point icon again and place it on another identifiable feature. Note that the points may appear distorted when being viewed from the other camera.

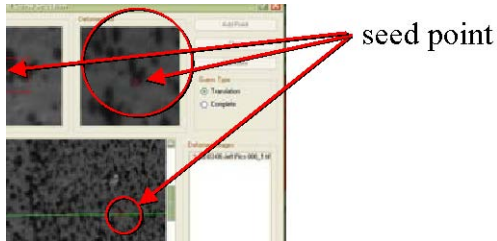
Once you **locate the point on the bottom and right images**, **click the point on both the left and right screens** that matches the seed point as seen in the left image.



Click **Add Point**, then click **Calculate**. The question mark over the deformed image name will change to a green check mark. Do this for all of the images. Click **Close** once a **green check mark** appears by **ALL images**.

Click the **start correlation analysis icon**  .

Under the **file tab**, make sure that all of the images you care to use in your analysis have a check next to their name.



Under the **option tab**, make sure to place a **check** by “**cubic B-spline interpolation**” and **uncheck** “**binomial low-pass filter**”. Also, change the “**contrast**” to **zero**.



Under the **thresholding tab**, **uncheck** “**use epipolar thresholding**”. Click **Run**.

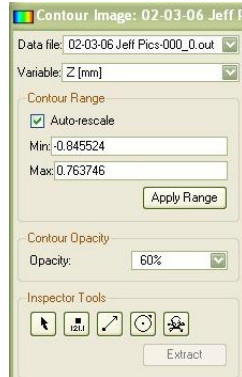


## VIC Analysis

Under the **Image Tab**, **right click** the **Deformed Image** you would like to analyze. **Click Contour Plot**.

Adjust the **Data File** and **Variable** fields according to your analysis needs. Use the **Inspector Tools** to **Extract** key information pertinent to your analysis.

Turn off cameras, light, and transformer power switch and place the lens covers back on the cameras if you have not done so already.



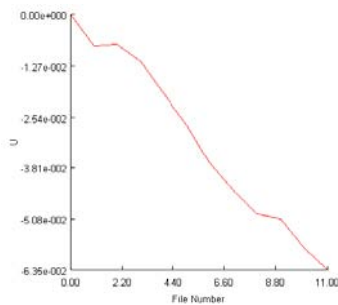
## Example Analysis

1) Objective: **Plot the U-deformation vs. load interval** for data collected from a target region on the specimen.

Use the circular (or similar) **inspection tool** to select a target region on the specimen aoi. **Click Extract**. Change the **Data File** field to the **next image** and **click Extract**. **Repeat** for all deformed image files (for each load interval).



Use data extracted from the target region to **plot U vs. File Number**.

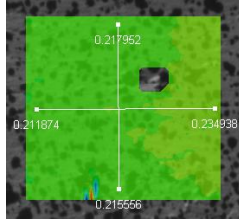


2) Objective: **Plot the U-deformation vs. Point Index** for data collected from a vertical line sketched on the fully loaded specimen and the **V-deformation vs. Point Index** for data collected from a horizontal line sketched on the loaded specimen.

**Select** the desired **image** from the **Data File** field.

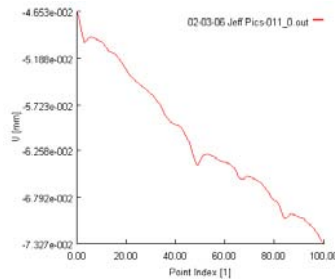
**Select U, V**, and any other variable of interest in the **Variable** field.

Use the **line inspection tool** to sketch a **vertical** and **horizontal line** on areas of interest on the image of the fully loaded specimen.



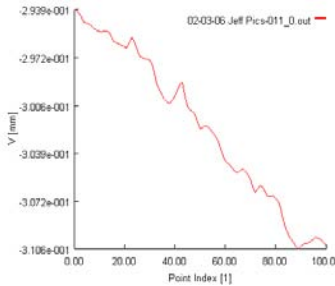
Click the **arrow icon** in the inspection toolkit. Click on the **vertical line** you sketched. Click **Extract** to extract data from the vertical line.

### Plot U vs. Point Index.



Click the **arrow icon** in the inspection toolkit. Click on the **horizontal line** you sketched. Click **Extract** to extract data from the horizontal line.

### Plot V vs. Point Index.



This data can be transformed, filtered, or used in its raw form for your analysis.

One final note is that you will want to check your analysis every step of the way. For example, your pre-analysis check should include a visualization of the VIC-generated contour plots that represent the surfaces of interest (AOI's). To do this, right click on each output file under the Data Tab and click "3D Plot". VIC3D will display a 3D plot of your AOI's. Look for plots that don't appear to be representative of the actual surfaces or that don't appear similar to other images in the group. You may want to consider removing these output files before continuing with your analysis.

Good luck with your analyses!

\*\*\*Special thanks to Dr. Peter Ifju for use of the VIC equipment and to Bret Stanford for providing the information necessary to compile this tutorial.

## LIST OF REFERENCES

- Akkus, O. Yeni, Y. Wasserman, N., 2004. Fracture mechanics of cortical bone tissue: A hierarchical perspective. *Critical Reviews in Biomedical Engineering* 32, 379-425.
- Alto, A. Pope, M., 1979. On the fracture toughness of equine metacarpi. *Journal of Biomechanics* 12, 415-422.
- An, Y., Friedman, R., 1999. *Animal models in orthopaedic research*. Boca Raton: CRC Press.
- An, Y., Draughn, R., 2000. *Mechanical testing of bone and the bone-implant interface*. Boca Raton: CRC Press.
- Arakere, N. Swanson, G., 2002. Effect of crystal orientation on fatigue failure of single crystal nickel base turbine blade superalloys. *Journal of Gas Turbines and Power* 124, 161-176.
- Arakere, N. Siddiqui, S. Magnan, S. Ebrahimi, F. Forero, F., 2005. Investigation of three-dimensional stress fields and slip systems for FCC single-crystal notched specimens, *Journal of Engineering for Gas Turbines and Power* 127, 629-637.
- Ashman, R., Cowin, S., Van Buskirk, W., and Rice, J., 1984. A continuous wave technique for the measurement of the elastic properties of cortical bone. *Journal of Biomechanics* 17, 349-361.
- Behiri, J. Bonfield, W., 1980. Crack velocity dependence of longitudinal fracture in bone. *Journal of Materials Science* 15, 1841-1849.
- Behiri, J. Bonfield, W., 1984. Fracture mechanics of bone – the effects of density, specimen thickness and crack velocity on longitudinal fracture. *Journal of Biomechanics* 17, 25-34.
- Behiri, H. Bonfield, W., 1989. Orientation dependence of the fracture mechanics of cortical bone. *Journal of Biomechanics* 22, 863-872.
- Bertholet, 1999. *Composite Materials – Mechanical Behavior and Structural Analysis*. Springer Verlag, New York.
- Bonfield, W. Behiri, J. Charalambides, B., 1985. Orientation and age-related dependence of fracture toughness of cortical bone. In: Perren, S. Schneider, E. (Eds.), *Biomechanics: Current Interdisciplinary Research*, pp. 185-189.
- Bonfield, W., 1987. Advances in the fracture mechanics of cortical bone. *Journal of Biomechanics* 20, 1071-1081.
- Boresi, A.P., Schmidt, R.J., Sidebottom, O.M., 2003, *Advanced Mechanics of Materials* (6<sup>th</sup> Ed.). John Wiley and Sons, Hoboken.
- Clifton, K., Golden, J., Reep, R., 2003. Material properties of subadult manatee bone. *Integrative and Comparative Biology* 43, 951.

- Clifton, K., 2005. Skeletal biomechanics of the Florida manatee. Ph.D. dissertation, Gainesville, University of Florida.
- Clifton, K., Reep, R. Mecholsky, J., 2007. Structural properties of manatee ribs tested in impact. *Journal of Materials Science* (submitted).
- Cooke, F. Zeidman, H. Scheifele, S., 1973. The fracture mechanics of bone – another look at composite modeling. *Journal of Biomedical Materials Research* 7, 383-399.
- Cowin, S., 2002. *Bone Mechanics Handbook* (2<sup>nd</sup> Ed.). CRC Press, Boca Raton.
- Currey, J.D., 1990. Physical characteristics affecting the tensile failure properties of compact bone. *Journal of Biomechanics* 23, 837-844.
- De Buffrenil, V., Schoevaert, D., 1989. Données quantitatives et observations histologiques sur la pachyostose du squelette du dugong, *Dugong dugon* (Muller) (Serenia, Dugongidae). *Canadian Journal of Zoology* 67, 2107-2119.
- De Santis, R. Anderson, P. Tanner, K. Ambrosio, L. Nicolais, L. Bonfield, W. Davis, G., 2000. Bone fracture analysis on the short rod chevron-notch specimens using the X-ray computer micro-tomography. *Journal of Materials Science: Materials in Medicine* 11, 629-636.
- Dong, X., Guo, X. 2004. The dependence of transversely isotropic elasticity of human femoral cortical bone on porosity. *Journal of Biomechanics* 37, 1281-1287.
- Evans, F.G., 1973. *Mechanical Properties of Bone*. Thomas, Springfield.
- FRANC3D Concepts and Users Guide, 2003. Available from the Cornell Fracture Group website ([www.cfg.cornell.edu](http://www.cfg.cornell.edu)). Ithaca.
- Freund, L., 1978. Stress-intensity factor calculations based on a conservation integral. *International Journal of Solids and Structures* 14, 241-250.
- Gibson, R.F., 1994. *Principles of Composite Material Mechanics*. McGraw Hill, New York.
- Gotzen, N., Cross, A., Ifju, P., Rapoff, A., 2003. Understanding stress concentrations about a nutrient foramen. *Journal of Biomechanics* 36, 1511-1521.
- Griffith, A., 1920. The phenomena of rupture and flow in solids. *Philosophical Transactions of the Royal Society of London* A221, 163.
- Grootenboer, H. Weersink, A., 1982. A composite model of cortical bone for the prediction of crack propagation. In: Huiskes, R. Van Campen, D. De Wijn J. (Eds.), *Biomechanics: Principles and Applications*. The Hague: Martinus Nijhoff.
- Gross, B., Srawley, J., 1964. Stress intensity factors for a single notch specimen by boundary collocation of a stress function. NASA TN D-2395.

- Hertzberg, R., 1989. Deformation and fracture mechanics of engineering materials. John Wiley and Sons, Hoboken.
- Hoffmeister, B. Smith, S. Handley, S. Rho, J., 2000. Anisotropy of Young's modulus of human tibial cortical bone. *Medical and Biological Engineering and Computing* 38, 333-338.
- Hoening, A., 1982. Near-tip behavior of a crack in a plane anisotropic elastic body. *Engineering Fracture Mechanics* 16, 393-403.
- Ifju, P., 1994. The shear gage: For reliable shear modulus measurements of composite materials. *Experimental Mechanics* 34, 369-378.
- Ifju, P., 1995. Shear testing of textile composite materials. *Journal of Composites Technology and Research* 17, 199-204.
- Iosipescu, N., 1967. New accurate procedure for single shear testing of metals, *Journal of Materials* 2, 537-566.
- Irwin, G., 1949. Fracture of metals. American Society for Metals. Cleveland, OH. pp.147-166.
- Irwin, G., 1957. Analysis of stresses and strains near the near the end of a crack traversing a plate. *Journal of Applied Mechanics* E24, 361.
- Kleerekoper, M., 2006. Personal contact. Quote available on Micro MRI, Inc. website: [www.micromri.com](http://www.micromri.com). Last accessed June 12, 2007.
- Knudsen, E., 2006. Anisotropic fracture analysis of the BX-265 foam insulation material under mixed-mode loading. Ph.D. thesis, University of Florida, Gainesville.
- Knudsen, E. Arakere, N., 2006. Numerical evaluation of Mode I stress intensity factor as a function of material orientation for BX-265 foam insulation material. In proceedings of the 51<sup>st</sup> ASME/IGTI Turbo Expo International Conference. Barcelona, Spain.
- Lekhnitskii, S.G., 1968. Anisotropic Plates. Gordon and Breach, New York.
- Lichtenberger, R., Schreier, H., 2002. Non-contacting measurement technology for component safety assessment, 6<sup>th</sup> International Symposium and Exhibition on Sophisticated Car Occupant Safety Systems. Rheinstetten, Germany.
- Liebowitz, H., 1968. Fracture, Academic Press, New York.
- Lucksanabool, P., Higgs, W., Higgs, R., Swain, M., 2001. Fracture toughness of bovine bone, influence of orientation and storage media. *Biomaterials* 22, 3127-3132.
- Malik, C.L., Stover, S.M., Martin, R.B. and Gibeling, J.C., 2003. Equine cortical bone exhibits rising R-curve fracture mechanics. *Journal of Biomechanics* 36, 191-198.
- Martin, R.B., Burr, D.B., Sharkey, N.A., 1998. Skeletal Tissue Mechanics. Springer, New York.

- Mehrabadi, M.M., Cowin, S.C., 1990. Eigentensors of linear anisotropic elastic materials, *Quarterly Journal of Mechanics and Applied Mathematics* 43, 15-41.
- Melvin, J. Evans, F., 1973. Crack propagation in bone. In: ASME biomaterials symposium. Detroit, MI.
- Moyle, D. Gavens, A., 1986. Fracture properties of bovine tibial bone. *Journal of Biomechanics* 17, 203-213.
- Murray, G., 1993. *Introduction to Engineering Materials*. CRC Press, Boca Raton.
- Nalla, R. Kinney, J. Ritchie, R., 2003. Mechanistic fracture criteria for the failure of human cortical bone. *Nature Materials* 2, 164-168.
- Nalla, R. Kruzic, J. Kinney, J. Ritchie R., 2005a. Mechanistic aspects of fracture and R-curve behavior in human cortical bone. *Biomaterials* 26, 217-231.
- Nalla, R. Stolken, J. Kinney, J. Ritchie, R., 2005b. Fracture in human cortical bone: local fracture criteria and toughening mechanisms. *Journal of Biomechanics* 38, 1517-1525.
- Neuman, W.F., Neuman, M.W., 1957. Emerging concepts of the structure and metabolic functions of bone. *American Journal of Medicine* 22, 123-131.
- Nicolella, D.P., Nicholls, A.E., Lankford, J., Davy, D.T., 2001. Machine vision photogrammetry: a technique for measurement of microstructural strain in cortical bone. *Journal of Biomechanics* 34, 135-139.
- Norman, T., 1995. Fracture toughness of human bone under tension, *Journal of Biomechanics* 28, 309-320.
- Norman, T. Vashishth, D. Burr, D. 1992. 2D finite element study of mode I fracture in human bone. In: Winter Annual Meeting of the American Society of Mechanical Engineers, Anaheim, CA.
- Norman, T. Vashishth, D. Burr, D., 1995. Fracture toughness of human bone under tension. *Journal of Biomechanics* 28, 309-320.
- Paruchuru, S. Wang, X. Agrawal, C., 2002. Finite element simulation of elastic compliance technique for formulating a test method to determine the fracture toughness of bone. *Journal of Mechanics in Medicine and Biology* 2, 473-486.
- Pope, M., Murphy, M., 1974. Fracture energy of bone in a shear mode. *Medical and Biological Engineering and Computing* 12, 763-787.
- Raju, I. Newman, J. Jr., 1979. Stress-intensity factors for a wide range of semi-elliptical surface cracks in finite-thickness plates. *Engineering Fracture Mechanics* 11, 817-829.

- Ranjan, S., 2005. Development of a procedure for mixed mode K-solutions of fatigue crack growth in FCC single crystal superalloys. Ph.D. dissertation, Gainesville, University of Florida.
- Ranjan, S. Arakere, N., 2007. A fracture mechanics based methodology for fatigue life prediction of single crystal nickel based superalloys. ASME Journal of Engineering for Gas Turbines and Power (In Press).
- Ray, S., Chinsamy, A., 2004. Diictodon Feliceps (Therapsida, Dicynodontia): Bone histology, growth, and biomechanics. Journal of Vertebrate Paleontology 24, 180-194.
- Rho, J., Kuhn-Spearing, L., Zioupos, P., 1998. Mechanical properties and the hierarchical structure of bone. Medical Engineering and Physics 20, 92-102.
- Rice, J., 1968. A path-independent integral and approximate analysis of strain concentrations by notches and cracks, Journal of Applied Mechanics 35, 379-386.
- Rice, J., 1968. Mathematical analysis in the mechanics of fracture, In: Liebowitz, H. (Ed.). Fracture (2<sup>nd</sup> Ed.). Academic Press, New York.
- Schachner, H. Reiterer, A. Stanzl-Tschegg, S., 2000. Orthotropic fracture toughness of wood. Journal of Materials Science Letters 19, 1783-1785.
- Schreier, H., Braasch, J., Sutton, M., 2000. Systematic errors in digital image correlation caused by gray-value interpolation. Optical Engineering 39, 2915-2921.
- Sih, G., 1973. Handbook of Stress Intensity Factors. Lehigh University. Bethlehem.
- Sih, G., Paris, P., Irwin, G., 1965. On cracks in rectilinearly anisotropic bodies, International Journal of Fracture Mechanics 1, 189-203.
- Stanzl-Tschegg, S. Tan, D. Tschegg, E., 1995. New splitting method for wood fracture characterization. Wood Science and Technology 29, 31-50.
- Stanzl-Tschegg, S., 2006. Microstructure and fracture mechanical response of wood. International Journal of Fracture 139, 495-508.
- Sutton, M., Cheng, M., Peters, W. et al., 1986. Application of an optimized digital correlation method to planar analysis. Image and Vision Computing 4, 143-151.
- Sutton, M., Turner, J., Bruck, H., Chae, T., 1991. Full field representation of the discretely sampled surface deformations for displacement and strain analysis. Experimental Analysis 31, 168-177.
- Swenson, D., Ingraffea, A., 1987. A finite element model of dynamic crack propagation with an application to intersecting Cracks. In: Proceedings of the 4<sup>th</sup> International Conference on Numerical Methods in Fracture Mechanics. San Antonio, TX.

- Swenson, D., Ingrassia, A., 1988a. Modeling mixed-mode dynamic crack propagation using finite elements: theory and applications. *Computational Mechanics* 3, 187–192.
- Swenson, D., Ingrassia, A., 1988b. Using combined experiments and analysis to generate dynamic critical stress intensity data. In: Cruse, T. (Ed.), *Fracture Mechanics: 19th Symposium*. ASTM STP 969. Philadelphia, pp. 405–426.
- Turner, C.H., Chandran, A., Pidaparti, R.M.V., 1995. The anisotropy of osteonal bone and its ultrastructural implications. *Bone* 17, 85-89.
- Van Rietbergen, B., Odgaard, A., Kabel, J., Huiskes, R., 1996. Direct mechanical assessment of elastic symmetries and properties of trabecular bone architecture. *Journal of Biomechanics* 29, 1653–1657.
- Van Rietbergen, B., Odgaard, A., Kabel, J., Huiskes, R., 1998. Relationships between bone morphology and bone elastic properties can be accurately quantified using high-resolution computer reconstructions. *Journal of Orthopaedic Research* 16, 23–28.
- Vashishth, D., Behiri, J., Bonfield, W., 1997. Crack growth resistance in cortical bone: concept of microcrack toughening. *Journal of Biomechanics* 30, 763-769.
- Vashishth, D., 2004. Rising crack-growth-resistance behavior in cortical bone: implications for toughness measurements. *Journal of Biomechanics* 37, 943-946.
- Wang, X., Agrawal, M., 1996. Fracture toughness of bone using a compact sandwich specimen: effects of sampling sites and crack orientations. *Journal of Biomedical Materials Research* 33, 13-21.
- Wang, X., Shen, X., Li, X., Agrawal, C., 2002. Age-related changes in the collagen network and toughness of bone. *Bone* 31, 1-7.
- Weiner, S., Wagner, H., 1998. The material bone: Structure-mechanical function relations, *Annual Review of Materials Science* 28, 271-298.
- Westergaard, H., 1939. Bearing pressures and cracks. *Journal of Applied Mechanics* 6, 49-53.
- Williams, M., 1957. On the stress distribution at the base of a stationary crack, *Journal of Applied Mechanics* 24, 109-114.
- Wirtz, D., Schiffers, N., Pandorf, T., Radermacher, K., Weichert, D., Forst, R., 2000. Critical evaluation of known bone material properties to realize FE-simulation of the proximal femur. *Journal of Biomechanics* 33, 1325-1330.
- Wright, T., Hayes, W., 1976. The fracture mechanics of fatigue crack propagation in compact bone. *Journal of Biomedical Materials Research* 10, 637-648.
- Wright, T., Hayes, C., 1977. Fracture mechanics parameters for compact bone – Effects of density and specimen thickness. *Journal of Biomechanics* 10, 419-425.

- Yan, J., 2002. Biomechanical properties of manatee rib bone and analytical study using finite element analysis. M.S. Thesis, University of Florida, Gainesville.
- Yan, J., 2005. Elastic-plastic fracture mechanics of compact bone. Ph.D. thesis, University of Florida, Gainesville.
- Yan, J., Clifton, K., Reep, R., Mecholsky, J. Jr., 2006a. Application of fracture mechanics to failure in manatee rib bone. *Journal of Biomechanical Engineering* 28, 281-289.
- Yan, J., Clifton, K., Mecholsky, J. Jr, Reep, R. 2006b. Fracture toughness of manatee rib and bovine femur using a chevron-notched beam test. *Journal of Biomechanics* 39, 1066-1074.
- Yan, J., Clifton, K., Mecholsky, J. Jr, Gower, L., 2007. Effect of temperature on the fracture toughness of compact bone. *Journal of Biomechanics* 40, 1641-1645.
- Yang, G., Kabel, J., Van Rietbergen, B., Odgaard, A., Huiskes, R., Cowin, S.C., 1999. The anisotropic Hooke's law for cancellous bone and wood. *Journal of Elasticity* 53, 125-146.
- Yau, J., Wang, S., Corten, H., 1980. A mixed-mode crack analysis of isotropic solids using conservation laws of elasticity. *Journal of Applied Mechanics* 47, 335-341.
- Yeni, Y., Norman, T., 2000. Calculation of porosity and osteonal cement line effects on the effective fracture toughness of cortical bone in longitudinal crack growth. *Journal of Biomedical Materials Research* 51, 504-509.
- Yoon, H., Katz, J., 1976. Ultrasonic wave propagation in human cortical bone I, theoretical considerations for hexagonal symmetry. *Journal of Biomechanics* 9, 407-412.
- Zhang, D., Arola, D., 2004. Application of digital image correlation to biological tissues, *Journal of Biomedical Optics* 9, 691-699.
- Zhang, D., Arola, D., Reprogel, R., Zheng, W., Tasch, U., Dyer, R. 2007. A method for characterizing the mechanical behaviour of hoof horn. *Journal of Materials Science* 42, 1108-1115.
- Zioupos, P. Currey, J., 1998. Changes in the stiffness, strength and toughness of human cortical bone with age. *Bone* 22, 57-66.

## BIOGRAPHICAL SKETCH

Jeff Leismer was born in southeast Michigan in 1978. He moved to Houghton, Michigan in 1996 to begin working towards his bachelor's degree in biomedical engineering from Michigan Technological University. Jeff took an interest in space physiology and supportive technology for astronauts under the tutelage of Dr. William Cooke during his junior year. He developed a particular interest in bone mechanics and went on to receive a master of engineering degree from the department of mechanical engineering at Michigan Tech, where he developed a vibration therapy device capable of stimulating muscle and bone in order to reduce disuse atrophy in astronauts. After completing his master's degree in 2002, Jeff was accepted to the PhD program in the department of mechanical and aerospace engineering at the University of Florida. His initial project involved the stress analysis of single crystal nickel base superalloys used in the space shuttle main engine, aircraft, and industrial gas turbines. The many similarities between modeling the orthotropic turbine blade material and bone (another orthotropic material) landed him on his current project of studying the anisotropic elastic material and linear elastic fracture properties of the Florida manatee rib bone.

Before moving to Gainesville in the fall of 2002, Jeff married his wife, Renee Morrow, of Alpena, Michigan. The couple now has two rambunctious boys born in the spring of 2006.